UNIVERSITÁ DEGLI STUDI DI SASSARI
DIPARTIMENTO DI SCIENZE CHIMICHE, FISICHE, MATEMATICHE E NATURALI

Corso di Dottorato in Scienze e Tecnologie Chimiche
Ciclo XXXVI

Functional nanostructured surfaces with biocidal and antiviral properties

Settore Scientifico Disciplinare di Afferenza
ING-IND/22

Coordinatore:
Prof.ssa Carla Cannas
Supervisore:
Prof. Luca Malfatti

Candidato:
Matteo Poddighe

Anno accademico 2022/2023

Abstract

Discovered in the early 2000s, that of carbon-dots is a family of carbon-based nanomaterials that has received a great interest from the scientific community because of their excellent properties. Initially studied for their optical properties (especially fluorescence), the fields of application have become many over the years, finding greater use in the biomedical field, such as in bioimaging, photodynamic therapy, and control on inhibition and proliferation of microorganisms, among many others.

The goal of this doctoral work was to use these nanoparticles, the carbon-dots, to functionalize surfaces to confer them antimicrobial properties. The synthesized carbon-dots, starting from an amino acid, glycine, and two co-precursors, 1,5-diaminonaphthalene and glycyrrhizic acid, showed interesting antimicrobial properties. Specifically, dots synthesized with glycine and 1,5-diaminonaphthalene showed excellent antiviral activity against two variants of SARS-CoV-2, the original strain and the delta strain. Whereas dots synthesized from glycine and glycyrrhizic acid showed interesting antibacterial susceptibility against gram-positive bacteria, S. aureus and E. faecium. Characterizations carried out, such as TEM, FTIR, XPS, and NMR, allowed to understand the main structural features of these dots, while with EPR, it was possible to understand the mechanism of antimicrobial action of these dots, identifying the promotion of ROS by these nanomaterials. Finally, the dots that showed antiviral activity were used to functionalize the silicon-based surfaces through a covalent chemical approach, keeping their antiviral property unaltered, even after functionalization. The dots that showed antibacterial activity, on the other hand, were used to functionalize a self-standing PVA-based surface by embedding the materials within a polymer matrix. This system showed interesting application in preserving the integrity of fresh foods, such as fruits, by increasing their shelf-life.

List of Abbreviations

CDs:	Carbon-dots
C-dots:	Carbon-dots
GQDs:	Graphene quantum dots
CQDs:	Carbon quantum dots
CNDs:	Carbon nanodots
CPDs:	Carbonized polymer dots
ROS:	Reactive oxygen species
Gly:	Glycine
1,5-DAN:	1,5-diaminonaphthalene
DAN:	1,5-diaminonaphthalene
GA:	Glycyrrhizic acid
TEOS:	Tetraethoxysilane
APTES:	(3-aminopropyl)triethoxysilane
PVA:	Polyvinylalcohol
CD-Boron:	Carbon-dots of glycine, 1,5-DAN and boric acid
CD-Chlorine:	Carbon-dots of glycine, 1,5-DAN and hydrochloric acid
CD-Lico:	Carbon-dots of glycine, glycyrrhizic acid and boric acid

Introduction

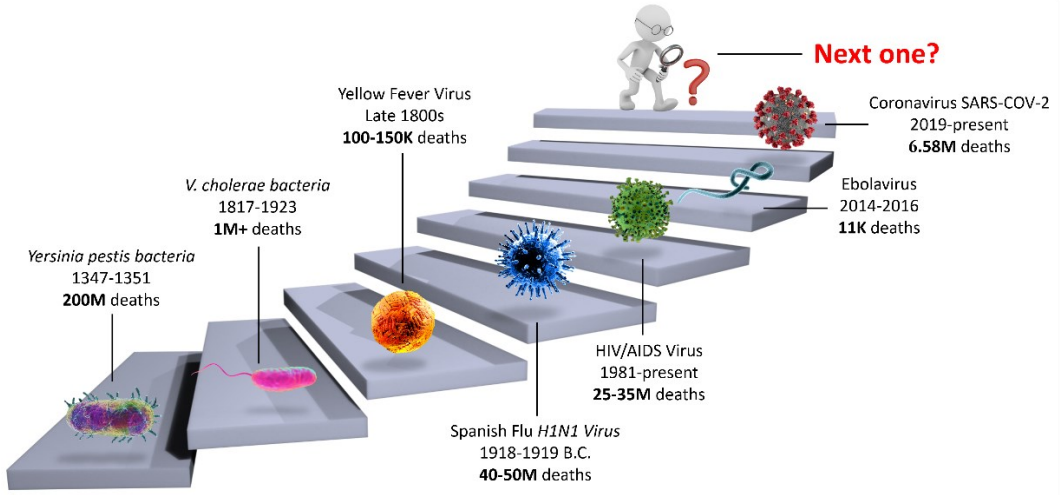

Figure A. This figure represents the most serious pandemics (viral and bacterial) faced by humanity throughout history.

Microbial infections have always been a challenge for researchers (**Figure A**) to find an effective way to safeguard human health [1]. Classical prevention methods such as vaccines, are not always the right solution, as they require a long time to be tested and marketed and have a well-defined and limited application, which could be ineffective in the long period [2]. Vaccines operate by improving the immune system's response against a viral or bacterial infection. This reaction forms a memory in the immune system, allowing the body to recall countermeasures to a specific virus or bacterium to protect itself against, so preventing sickness. The majority of vaccinations contain an antigen, which is a weakened or inactivated form or fragment of a virus or bacteria that is not capable of producing illness [3]. After receiving a vaccination, the immune system recognizes the antigen as alien. This activates immune system cells, which make antibodies to neutralize the disease-causing virus or bacteria.

The recent pandemic emergency has increased researchers' interest in this field, leading to the development of new technologies to fight the spread and proliferation of microorganisms [4]. Among the various proposals in the literature, the

engineering of nanostructured functional surfaces seem to be the most promising solution. At the moment, the most studied surfaces are those functionalized with silver nanoparticles, gold nanoparticles, cerium oxide nanoparticles and quaternary ammonium salts [5-7] (**Figure B**). The main problems with these systems arise from the poor mechanical strength properties of the synthesized films, because they are not resistant to scratching or fingerprint testing, and the intrinsic chemical instability of the nanoparticles used for the functionalization. In fact, many of them become deactivated and can no longer be used once antimicrobial activity has taken place [8]. These drawbacks make these systems very difficult to be applied in real-world applications.

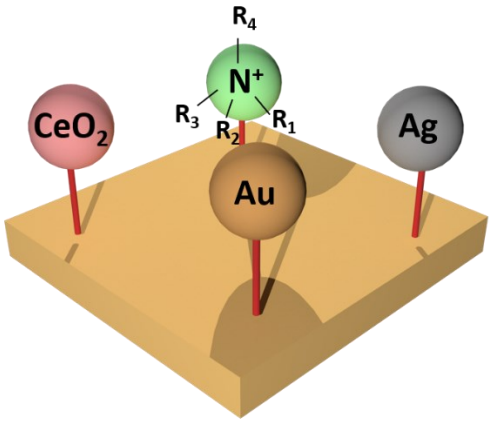

Figure B. This figure represents a schematization of the surfaces currently proposed in the literature for fighting the spread and proliferation of microbes.

A new category of nanoparticles that has received great interest in the scientific world is that of carbon-dots [9]. These are carbon-based nanoparticles, with a size of less than 10 nm, easy to synthesize, low cost and highly biocompatible [10] They possess excellent optical properties, making them versatile in various fields of application. The most studied fields of application are those involving biosensors, however they are also used as markers in bioimaging [11, 12]. Recently, with the advent of the pandemic emergency, it has been found in several scientific studies that these nanoparticles have efficient antimicrobial activity [13-15]. The use of

these systems makes it possible to minimize the spread and proliferation of viruses and bacteria.

Aim of the thesis

In this thesis work, synthesis of new carbon-dots, and the engineering of the related functionalized surfaces will be presented. The aim of the study is to design systems capable of inhibiting and fighting the proliferation and spread of microorganisms which can eventually be used for real-world applications.

The chemical design of these carbon-dots was selected based on the interactions between the functional groups of the precursors. An amino acid was chosen as the basis for the synthesis of the carbon-dots, to which several precursors were associated that have amine and carboxyl groups. The presence of these specific functional groups allows the interaction of these molecules through the formation of amide-type bonds. The choice of amino acid was based on the possibility of using a biocompatible compound, with the goal of synthesizing materials with low toxicity. The use of acid catalysts makes it possible to improve the degree of reaction between the various precursors, resulting in the best possible structure. This is because the acid catalyst allows the functional groups of the amino acid to be activated in a way that makes it more reactive.

Once the nanoparticles with the best antimicrobial activity are obtained, they are chemically bound to a silicon-based surface, or embedded into a PVA-based polymer matrix, in order to obtain a surface with biocidal properties that can be used in biomedical applications.

Structure of the thesis

The thesis is structured as follows:

- The first chapter focuses on the state of the art of carbon-dots, their properties and applications, with emphasis on their use to fight the spread and proliferation of pathogens.
- The second chapter discusses the experimental part, tdescribes the motivations in selecting the precursors and the rationale behind each system.

- The third chapter illustrates and comments all the results obtained.
- The fourth chapter is devoted to draw the conclusions of the experiments, and identify the pros and cons of each system. Moreover a possible real-world application and technology scale-up of the on a large scale is commented.

Chapter 1: State of the Art

Carbon-dots

Carbon-dots are carbon-based nanostructures that have received increasing attention from the scientific community in recent years. Discovered in 2004 [16], during an experiment on carbon nanotubes (CNTs), Carbon-dots can be divided in different families of nanoparticles: graphene quantum dots (GQDs), carbon quantum dots (CQDs), carbon polymer dots (CPDs) and carbon nanodots (CNDs). These classifications are derived from one of the main problems we run into when carbon-dots are studied, which is structural variation (**Figure 1.1**). It has been generally accepted to define carbon-dot as a material that has a particle size of less than 10 nm composed of a carbon matrix (crystalline or amorphous) and functional groups on the surface [17].

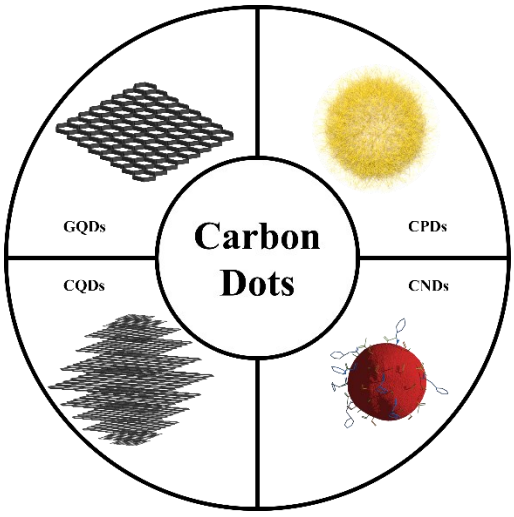

Figure 1.1 The figure shows the four main structures of carbon-dots: GQDs, CQDs, CPDs and CNDs.

The nomenclature and subsequent classification of these nanoparticles are not yet defined because of the extreme heterogeneity of the structure, as well as the wide range of potential starting materials and synthetic approaches. GQDs and CQDs

differ from CNDs due to the presence of extended π-conjugated carbon structures and quantum size effect (although this is not always proven). GQDs are formed by by a single graphene layer, while tf CQDs are composed by a series of stacked graphene layers leading to an almost spherical shape (**Figure 1.2 a, b**). CNDs (**Figure 1.2 c**), finally, show a mixture of graphitic and amorphous structures, due to the presence of atoms with sp^2 and sp^3 hybridization [18]. This classification, however, does not uniquely explain the identification of these nanoparticles. There are other factors to consider beside the core structure, such as defects on the surface (in the case of CQDs and CNDs) or on the edges (in the case of GQDs) due to the presence of functional groups, especially those based on oxygen compounds (carbonyl, carboxylic and hydroxyl groups) [19]. As a consequence of the surface functional groups, the large family of carbon-dots contains nanoparticles with different hydrophylicity: by properly adjusting the chemical synthesis, in fact, it is possible to design hydrophobic, hydrophilic s and also amphiphilic carbon-dots [20]. Finally, a fourth category, that of carbonized polymer-dots (CPDs), has attracted the attention of the scientific community in recent years (**Figure 1.2 d**). CPDs result from the partial carbonization of reagents of polymeric nature. The structure of these nanoparticles is composed of an amorphous core with a variable degree of carbonization, surrounded by a polymeric fraction, which may have different functional groups [21].

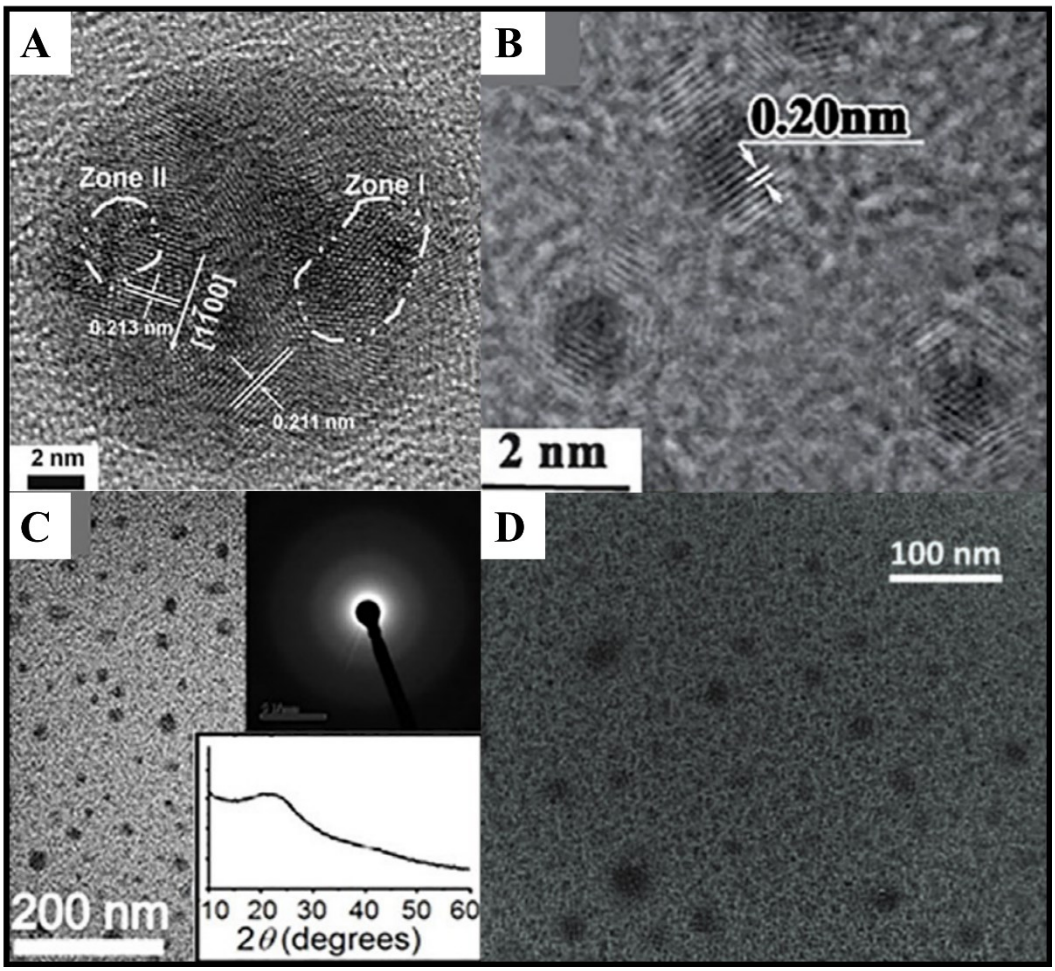

Figure 1.2 The figure shows TEM images related to the various structures of the four main carbon-dots: A) GQDs, B) CQDs, C) CNDs and D) CPDs. Image A) reproduced with permission of Ref 22; images B), C), and D) reproduced with permission of Ref 23.

The presence of functional groups or heteroatoms used as dopants in these structures makes it possible to improve or confer certain properties to carbon-dots. One of the distinguishing properties of these nanoparticles is their excellent fluorescence [24].

Fluorescence is a property of light emission when carbon-dots are excited by light radiation (**Figure 1.3**). This fluorescence can be tuned by varying the size, shape

and chemical composition of the carbon-dots [25]. The ability to emit light at different wavelengths has made carbon-dots very attractive for applications in biomedical imaging, sensor technology and optoelectronic devices [26].

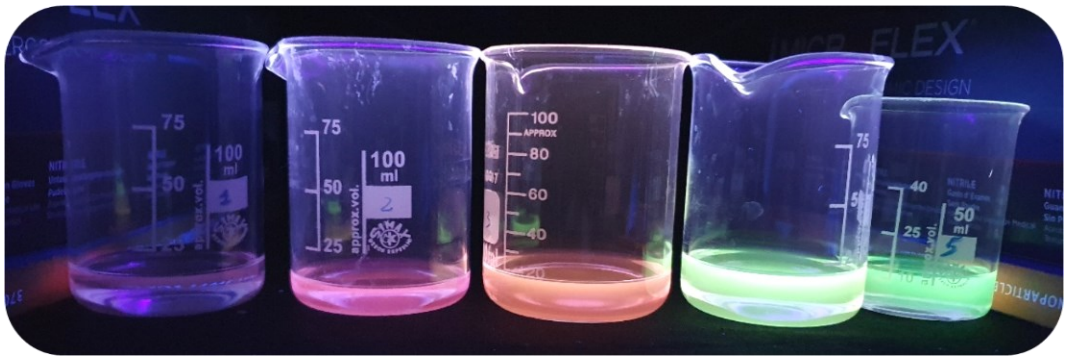

Figure 1.3 Representation of the various emissions of carbon-dots at different wavelengths.

The versatility of carbon-dots is also reflected in their easy functionalization. The surface of carbon-dots can be modified by introducing functional groups through various chemical reactions. This functionalization allows the properties of carbon-dots to be improved or new functionalities to be conferred. For example, chemical groups can be introduced to improve solubility in different solvents, to provide selective targeting in the biomedical field, or to promote specific chemical reactions [27-29].

Another interesting feature of carbon-dots is their biocompatibility. Because of the carbon-based structure and the possibility of functionalization, many carbon-dots can be used in biomedical applications without causing significant toxicity. Their biocompatibility makes them promising for cell imaging, controlled drug delivery, and photodynamic therapy [30-32].

They have been used as contrast agents for biomedical imaging, as sensors for detecting specific ions or molecules, and as catalysts for chemical reactions. The wide range of applications of carbon-dots is evidence of their potential in various fields of science and technology.

Methods for the synthesis of carbon-dots

The methods for preparing carbon-dots are various, but they can be divided into two large families: those relying on Top-Down approach and those using a Bottom-Up approach (**Figure 1.4**) [33, 34].

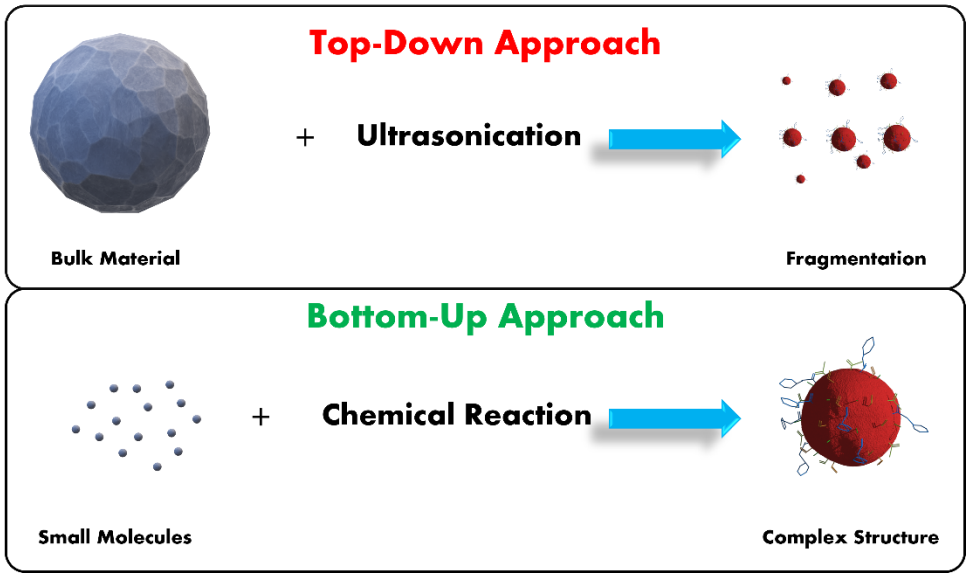

Figure 1.4 Schematic example of A) a reaction using the Top-Down method and B) a reaction using the Bottom-Up method.

Top-down methods involve reducing the size of a larger starting material, such as graphene or carbon nanotubes, to obtain nanometer-sized carbon-dots. The starting materials undergo mechanical or chemical erosion processes, such as laser ablation, acid treatment or ultrasound. Controlling the size of carbon-dots in top-down methods can be more difficult than in bottom-up methods [35]. The size and distribution of the particles depend on the nature and properties of the starting material and the synthesis parameters.

Methods for Top-Down include:

- Laser ablation: this method involves using a high-energy laser to fragment a larger carbonaceous material, such as graphene or carbon nanotubes. The laser focused on the carbonaceous material causes vaporization and local explosion, generating carbon-dots particles.

- Mechanical erosion: in this method, a larger carbonaceous material, such as graphite, is subjected to mechanical erosion using ultrasound or high-energy grinding. This mechanical fragmentation process reduces the size of the carbonaceous material until the desired carbon-dots are obtained.

- Laser combustion: a high-energy laser is used to induce the combustion of a larger carbonaceous material, such as graphene or carbon nanotubes. During laser combustion, evaporation, melting and condensation processes occur, leading to the formation of carbon-dots.

- Electromechanical shearing and disintegration: this method involves the use of electrical and mechanical forces to fragment a larger carbonaceous material. Carbon-dots are produced by the application of a high-intensity electric field, which induces the disintegration and fragmentation of the carbonaceous material.

Carbon-dots from top-down method, for instance, were synthesized from a dispersion of graphite in ethanol, with a graphite particle size of 400 nm. In this case, a laser pulse in the range of 150 femtoseconds was used, which hit the sample, placed under stirring, with a wavelength of 800 nm, for a total reaction period of 30 minutes [36]. The carbon-dots obtained had a minimum size of about 1 nm and a high amount of functional groups due to laser ablation. Other dots have been synthesized from a dispersion of a carbon matrix in water. Laser treatment at 248 nm resulted in the formation of non-fluorescent nanoparticles, which needed to be subjected to treatment in HNO_3 and PEG_{200} to activate the functional groups on the

surface of the carbon-dots and give them the fluorescence property [37]. The maximum of emission of these nanoparticles was in the range of the blue region spectra, at 450 nm. The influence of solvent has also been studied. It has been reported that treating a graphite sample dispersed in different solvents such as water, acetone, isopropyl alcohol and PEG_{200} with laser ablation leads to the formation of very small nanoparticles (less than 3 nm). The laser wavelengths used in this case were two, one at 1064 nm and one at 355 nm. Among all the solvents used, the only medium that did not lead to obtaining fluorescent nanoparticles was water [38]. Another way to obtain these nanoparticles via laser ablation was reported by treating with a laser having a wavelength of 532 nm, a dispersion of graphite in a liquid with a polymeric character, polyethyleneimine (PEI). Once the sample was treated, it was dialyzed against water for 5 days, and only after dialysis, nanoparticles that exhibit fluorescence properties and emission at about 440 nm, were obtained [39].

Synthesis techniques employing the use of high-intensity electric fields have been used for the synthesis of carbon-dots starting from graphite rods [40]. The application of the electric field led to the formation of single-wall carbon nanotubes (SWNTs), which, when treated by refluxing with a mixture of sulfuric acid and nitric acid, resulted in fluorescent nanoparticles in the green range of the spectra (about 502 nm). Using an arc discharge technique, carbon-dots doped with two heteroatoms, boron and nitrogen, were obtained [41]. An electrode made by mixing Boron powder with graphite was used for boron doping. For nitrogen doping, a graphite electrode was used in the presence of a gas mixture where ammonia was present. A high-intensity electric field was used for both systems, in the presence of flow of H_2 and He, in order to obtain doped graphene particles. The doped GQDs were finally obtained by ultrasonic treatment in the presence of a mixture of HNO_3 and H_2SO_4 (**Figure 1.5**). The GQDs thus synthesized showed a particle size of about 5-6 nm and fluorescence with an emission at about 420 nm.

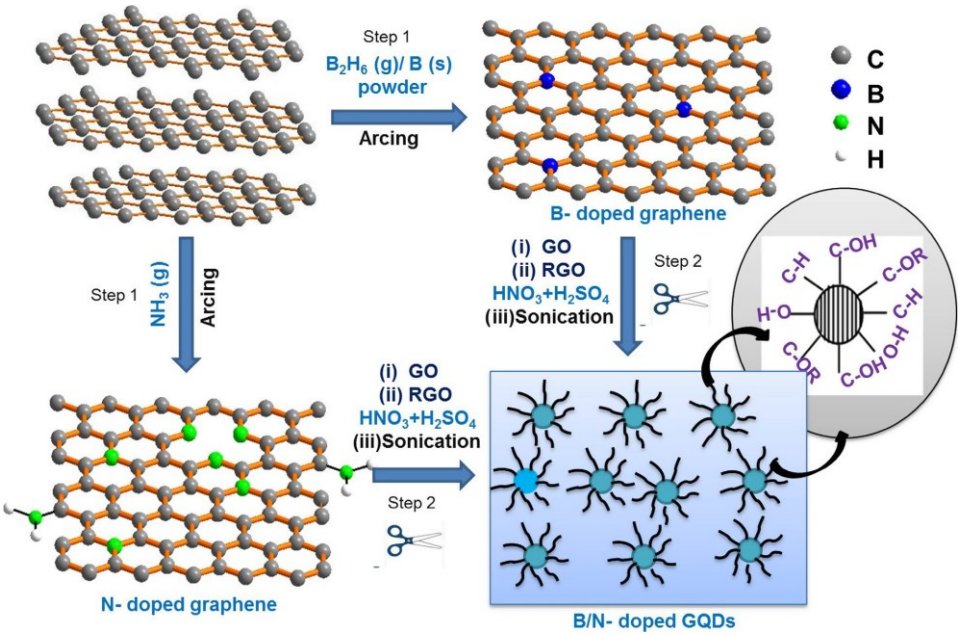

Figure 1.5 Schematic representation of top-down syntheses of GQDs doped with boron and nitrogen atoms. Image reproduced with permission of Ref 41.

As opposed to top-down methods, bottom-up synthesis involve the construction of carbon-dots from molecular or atomic precursors. Organic or inorganic molecules are reacted or converted into carbon nanoparticles. The precursors are subjected to controlled chemical reactions, such as hydrothermal synthesis, microwave synthesis or sol-gel synthesis, to obtain the desired carbon-dots. In bottom-up methods, the size control of carbon-dots is generally more precise than in top-down methods [42]. Synthesis parameters, such as temperature, reaction time, pH and reagent concentration, can be adjusted to obtain nanoparticles of specific sizes and properties. Bottom-up methods can be more easily scaled up than top-down methods because synthesis from molecular or atomic precursors allows greater control over the production of carbon-dots.
Methods for Bottom-Up include:

- Hydrothermal synthesis: the method involves the chemical reaction of organic or inorganic precursors in an aqueous solution at high temperatures (usually

around 200°C) and in a controlled environment. The precursors are dissolved in the solution, and under the effect of temperature and pressure, chemical reactions occur, leading to the formation of carbon-dots.

- Microwave synthesis: organic or inorganic precursors are mixed in a solution and subjected to microwave irradiation. The microwave energy heats the system, accelerating the chemical reactions that lead to the formation of carbon-dots. This method can be rapid and efficient in obtaining carbon-dots of controlled size.

- Electrochemical synthesis: This method. By applying an electric current to uses carbon electrodes immersed in a solution containing carbon precursors, electrochemical charges are generated. These trigger redox reactions leading to the formation of carbon-dots on the surface of the electrodes. Electrochemical synthesis offers precise control over the size and properties of the carbon-dots.

Through the use of microwave synthesis techniques, carbon-dots were obtained from sucrose, diethylene glycol and gadolinium oxide [43]. A classic kitchen microwave with a power of 750 W was used, obtaining nanoparticles with a particle size of about 5 nm and an emission in the green range, at about 510 nm. Using the same technique, dots exhibiting nitrogen and phosphorus doping were obtained from the precursors ethylenediamine and N-phosphonomethyl aminodiacetic acid [44]. Treatment of these reagents at 700 W for 7 min resulted in nanoparticles with emission at 418 nm and dots size of about 3 nm. Another way to obtain carbon-dots by microwave is to treat a solution containing citric acid, urea and thiourea, at 450 W for 5 minutes [45]. The dots thus synthesized can be separated after centrifugation and subsequent dialysis against distilled water, resulting in particles with a size of 10 nm and emission at 523 nm. It is possible to obtain carbon-dots also starting from citric acid only, [46]. A high-power microwave treatment for 8 minutes results in the synthesis of nanoparticles with fluorescence in the blue, at about 450 nm, and a size between 3 and 5 nm.

Direct combustion of citric acid at 200°C for 35 minutes on a hot plate led to the production of carbon-dots [47]. In this case, the synthesized nanoparticles were obtained after performing purification by dialysis, obtaining as a product, dots with a fluorescence around 460 nm and a relatively narrow particle size distribution around 6 nm. Burning glucose and L-aspartic acid, at 125°C for 30 minutes and then at 200°C for 20 minutes, yields carbon-dots with an emission ranging from 465 to 550 nm as the concentration of dots in solution increases [48]. Carbon-dots synthesized in this way have a particle size with a center around 2 nm. Thermal pyrolysis of citric acid and diethylenetriamine, used here as a surface passivation agent, is one of the methods reported for obtaining carbon-dots [49]. The nanoparticles, obtained after dialysis and subsequent freeze-drying, showed emission at about 458 nm with a red shift to 537 nm changing from an excitation of 380 nm to 480 nm, respectively. The carbon-dots thus synthesized had an average size of 7 nm.

One of the most widely used synthesis methods, following the bottom-up approach, is the one that uses stainless steel autoclaves to carry out hydrothermal/solvothermal reactions. Solubilizing citric acid and cysteine in distilled water, it is possible to obtain carbon-dots after the treatment of this solution by hydrothermal reaction at 200°C for 3 hours [50]. The nanoparticles thus obtained have an average size of 8 nm and an emission around 415 nm. Following the same process but in organic solvent, in this case acetone, it is possible to synthesize carbon-dots starting from $SiCl_4$ and hydroquinone, in order to obtain Si-doped carbon-dots [51]. The solvothermal synthesis at 200°C for 2 hours leads to nanoparticles with a size of 7 nm and a fluorescence in the range of UV, around 380 nm. Using hydroquinone and BBr_3, have been synthesized carbon-dots by solvothermal reaction at 200°C [52]. The doped Boron carbon-dot synthesized in this way (**Figure 1.6**), showed an emission at 360 nm and an average nanoparticle size of 16 nm.

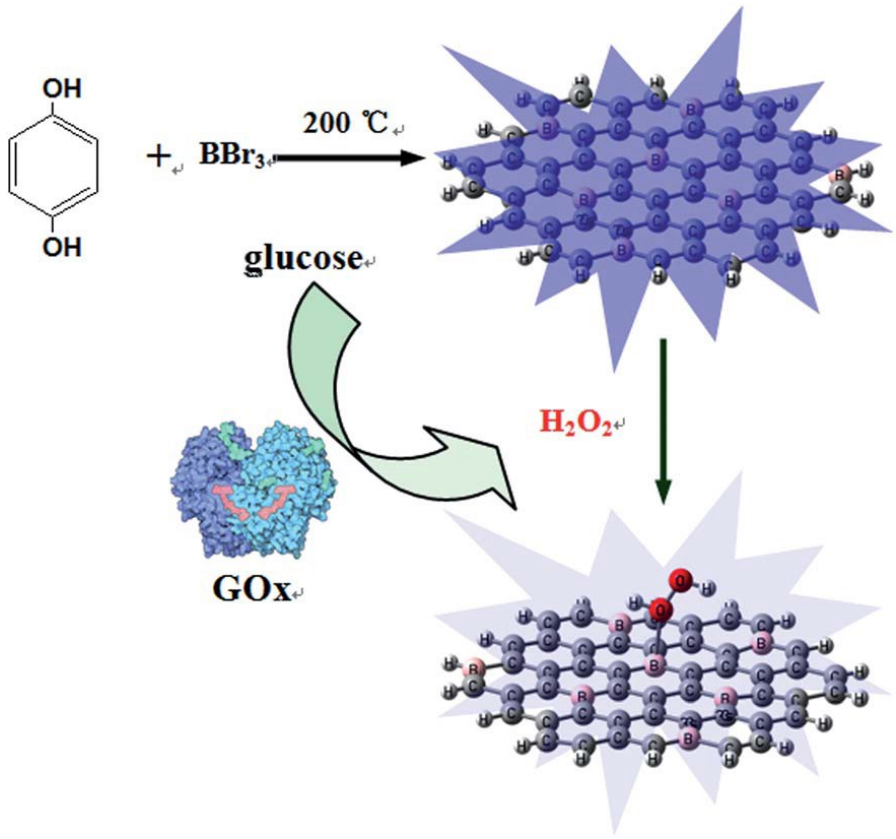

Figure 1.6 Schematic representation of Top-Down syntheses of GQDs doped with boron and nitrogen atoms. Image reproduced with permission of Ref 52.

Carbon-dots properties: the fluorescence

Despite structural differences among various types of carbon-dots, they possess similar characteristics, such as dispersibility in water or other organic solvents [53-57]; high biocompatibility and low toxicity [58-62]; and electromagnetic radiation absorption and emission properties [63-67]. These properties are mainly due to the presence of specific functional groups.

The photoluminescence of carbon dots represents one of their most intriguing and useful features.

The fluorescence of carbon-dots is tunable [68-70] (**Figure 1.7**), it is influenced by pH [71] and solvent [72, 73] and generally shows a high quantum yield [74-76].

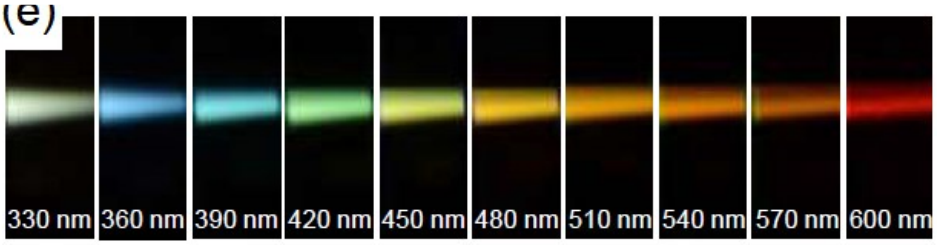

Figure 1.7 Illustration of the various carbon-dots emissions. Image reproduced with permission of Ref 77.

The characteristic absorption of light in these nanoparticles is broad in the electromagnetic radiation spectrum, but mainly occurs in the ultraviolet range. This is because the main light-absorbing portions in carbon-dots are those where conjugated carbons are present (as in C=C bonds or aromatic rings) leading to $\pi \rightarrow \pi^*$ type electronic transitions and $n \rightarrow \pi^*$ type absorptions (**Figure 1.8**). The presence of specific functional groups containing oxygen and other heteroatoms contributes to modulate and shift the absorption range inducing relevant differences in the photophysical properties of the dots [78].

Transition	λ radiation
$\sigma \rightarrow \sigma^*$	110 – 135 nm
$\pi \rightarrow \pi^*$	160 – 255 nm
$n \rightarrow \sigma^*$	160 – 255 nm
$n \rightarrow \pi^*$	> 285 nm

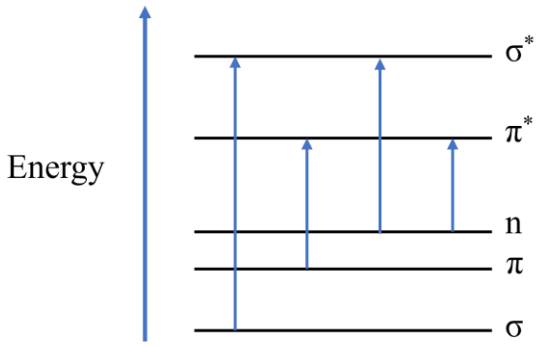

Figure 1.8 Schematic representation of the main electronic transitions that occur under irradiation.

The main factor influencing the absorption, however, is the structural composition of carbon-dots [79]. The presence of crystalline structures, such as in GQDs and

CQDs, leads to π-conjugate systems, which are primarily responsible for light absorption and emission. The size of the nanoparticles in this case affects the mechanism of photoluminescence: smaller particles show a shift in emission toward lower wavelengths (higher energy), while larger particles tend to shift toward higher wavelengths (lower energy) [80, 81]. In CNDs and CPDs, on the other hand, photoluminescence is of the molecular type, and absorption and emission depend mainly on the presence of certain functional groups on the surface of the nanoparticles, or on the partial graphitization of the dot [82, 83]. Specifically, the presence of defects due to oxidation leading to the formation of oxygen-containing groups promote a shift of the emission to higher wavelengths. The presence, on the other hand, of functional groups such as carbonyl or amide groups promotes a shift of emission to lower wavelengths.

The main challenge is therefore to appropriately modify the structure of the dots in order to achieve the desired absorption and emission [84]. This problem can be tackled by selecting the most suitable precursors and synthesis techniques, depending on the designated target [85].

The mechanisms of carbon-dots fluorescence are the subject of ongoing scientific research and include several processes. The most commonly hypothesized mechanisms are listed below.

- Emission mechanism by absorption and recombination: carbon-dots can absorb energy from an excitation source, such as ultraviolet light or laser light, through their surface functional groups. The absorbed energy is then converted into excited electron energy within the carbon-dot structure. Subsequently, the excited electrons can recombine with the holes left in the valence band, releasing energy in the form of fluorescent light [86].

- Forbidden-band emission mechanism: the mechanism is based on the presence of forbidden energy bands within the carbon-dot structure. When electrons are excited, they can jump from a valence band to a conduction band through a nonradiative transition process. Subsequently, the electrons

can decay back to the valence band, releasing energy in the form of fluorescent light [87].

- Mechanism of surface state emission: carbon-dots have a surface rich in functional groups and structural defects. These defects can create energetic surface states that can be populated by excited electrons. When electrons transit from these surface states to the valence band, fluorescent light emission occurs [88].

Applications

Because of their amazing photoluminescence properties, carbon-dots find applications in a wide variety of fields (**Figure 1.9**).

Carbon-dots have demonstrated to be promising materials in both biological [89] and energy fields [90].

In the context of biological applications, the low toxicity and ease of degradation of these carbon-based nanomaterials make them of particular interest in the biomedical field [91, 92].

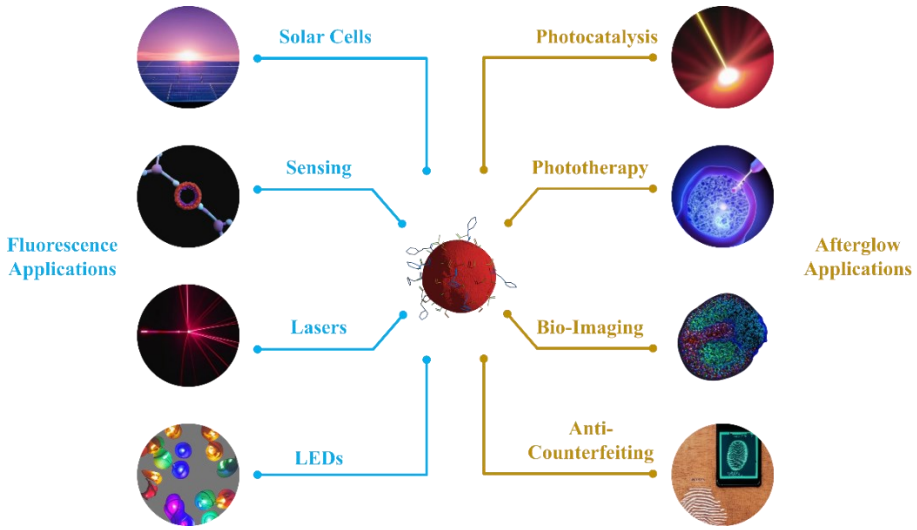

Figure 1.9 Schematization of the main applications due to the fluorescence and afterglow effect.

Several examples of carbon-dots applied to biological applications have been reported so far. Carbon-dots obtained from citric acid and polyene polyamine, for instance, were conjugated to a platinum complex for the diagnosis of liver tumor cells in a mouse, used as a model for in vivo measurements [93]. The synthesized dots exhibited a blue-range fluorescence observed in the in vivo image, and a change in emission was achievable by varying the excitation wavelength in in vitro analyses. The hydrothermal synthesis of 2,3-diaminophenazine and folic acid led to the formation of carbon dots used for the treatment of tumor cells in vivo [94]. These dots exhibited selectivity in attacking tumor cells in a mouse, resulting in the apoptosis and death of those cells (**Figure 1.10**). Other carbon dots, employed in drug delivery, were conjugated with $mSiO_2$-PEG for the transport of anticancer drugs into HeLa cells [95]. Although these carbon dots are conjugated with anticancer drugs, it has been demonstrated that the dots do not affect the drug's efficacy in any way. After drug release, carbon-dots are eliminated from the body without any side effects [96].

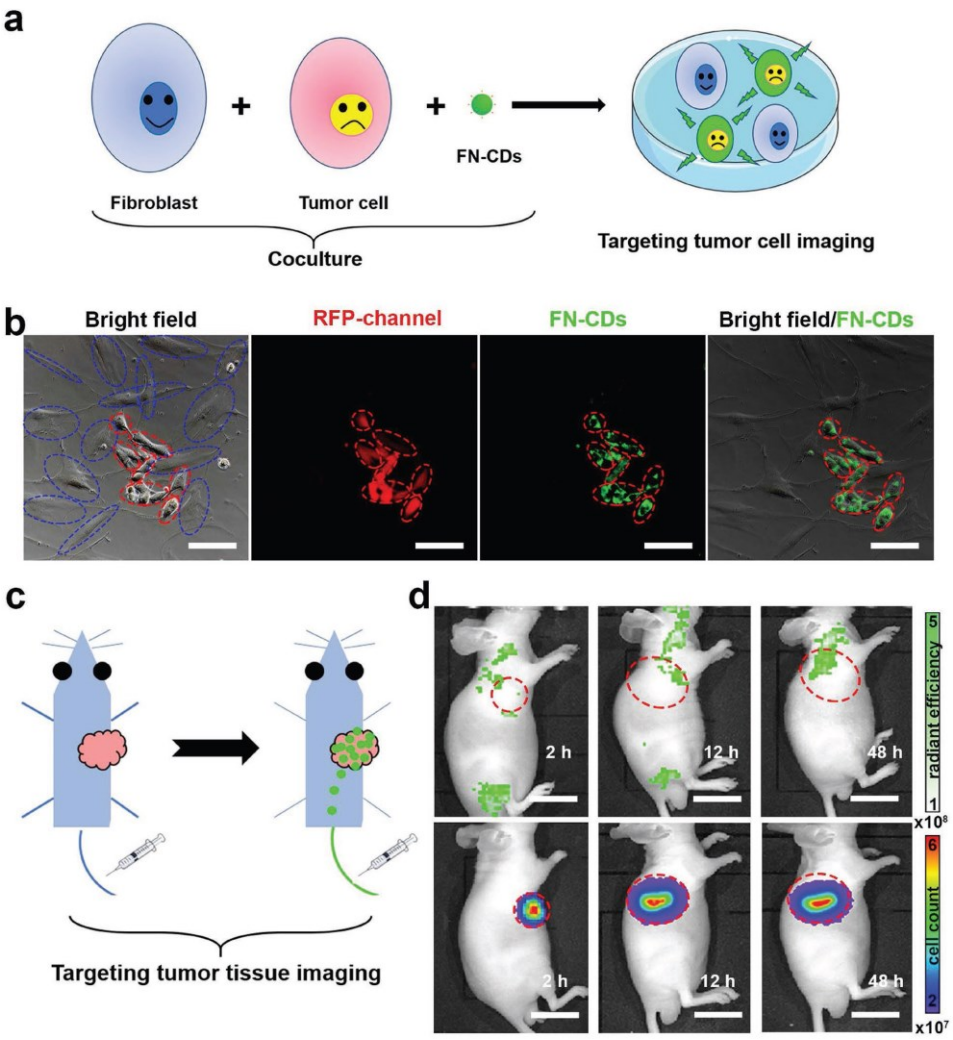

Figure 1.10 Tumor-specific fluorescence imaging in vitro and in vivo. a) Diagram of tumor-cellular specific bioimaging in vitro; b) fibroblast cultures with carbon-dot incubation; c) diagram of tumor-targeted fluorescence bioimaging in vivo; d) Real-time in vivo images of tumor-bearing mice at various time points after i.v. injections of FN-CDs. The tumor sites are marked by red circles. Image reproduced with permission of Ref 94.

The catalytic properties of these nanomaterials make carbon dots particularly attractive for research in the fields of hydrogen production, O_2 reduction, CO_2 reduction, and water splitting [97-100]. Other areas of interest include energy storage [101-102] and the development of light-emitting diodes (LEDs) [103-107].

The doping of carbon-dots with heteroatoms like nitrogen has allowed the production of GQDs capable of performing water splitting reactions [108]. In this case, the GQDs were divided into two portions, each serving as electrodes. The carbon-dot portion containing oxygen acted as the anode, where H_2 production occurred, while the part containing nitrogen served as the cathode, where O_2 was produced. In the case of using CDs as photosensitizers, it was possible to increase the energy efficiency of a photovoltaic cell [109]. The actual advantage of using these GQDs, which showed a slight increase in efficiency compared to the photoactive polymer alone, lies in the ease of manipulating the nanoparticle for integration into the organic photoactive matrix. Another way to employ GQDs, is for the protection of a VO_2 electrode, in a lithium-ion battery [110]. The coverage over the entire electrode by these carbon-dots, not only allowed the electrode to be preserved throughout the life of the battery, but also increased the amount of ions stored. A battery so composed showed high ions storage capacity for more than 1,500 cycles.

Antimicrobial activity of Carbon-Dots

Among all the possible applications, also accomplice to the recent pandemic emergency, the antimicrobial activity of these carbon-based nanoparticles has received great interest from the scientific community [111-113].

Carbon-dots have shown promising potential as antimicrobial agents against viruses, bacteria, and fungi [114-116]. Their antimicrobial activity is attributed to a combination of several mechanisms, including inhibition of microbial growth, interference with metabolic processes, and direct inactivation of microorganisms.

Antiviral activity of Carbon-Dots:

Carbon-dots have shown to possess antiviral activity against several types of viruses, including RNA and DNA viruses. Inhibitory properties of carbon-dots have been observed against viruses such as influenza, HIV, hepatitis C virus, and Zika virus. The antiviral effect of carbon-dots may result from their ability to bind to viral proteins, inhibiting virus adhesion to host cells. In addition, carbon-dots can

interfere with the replicative cycle of viruses, inhibiting viral replication and assembly [117-120].

The mechanism of antiviral action of carbon-dots can be complex and may vary depending on the type of virus being targeted. However, some of the most common ways through which carbon-dots can exercise their antiviral activity are listed below.

- Inhibition of viral adhesion: carbon-dots can interact with viral proteins and prevent virus adhesion to host cells. This can occur through direct interaction between the surface functional groups of carbon-dots and viral proteins on the surface of the virus. The ability of carbon-dots to block viral adhesion can prevent infection of host cells and reduce the spread of the virus.

- Inhibition of viral penetration: carbon-dots can interfere with the process of virus penetration into host cells. For example, they can interact with cellular receptors that the virus uses to enter cells, thus blocking virus entry. In addition, carbon-dots can bind to the virus itself, preventing its fusion with the cell membrane and the subsequent release of its genetic material inside the host cell.

- Inhibition of viral replication: carbon-dots can interfere with the replicative cycle of viruses once they have entered host cells. They can act in a variety of ways, such as by inhibiting the activity of key viral enzymes required for replication of viral genetic material or by interfering with transcription and translation of viral genes. In this way, carbon-dots reduce the ability of the virus to replicate within host cells, thereby slowing the spread of infection.

- Induction of antiviral immune response: carbon-dots can stimulate the antiviral immune response of the host organism's immune system. They can act as adjuvants, enhancing the immune response against the virus. This can

occur through presentation of viral antigens to lymphocytes and activation of immune cells involved in the antiviral response, such as T and B lymphocytes. Stimulation of the immune response may contribute to eliminate the virus from the host body and prevent of future infections.

It is important to understand that the mechanisms of antiviral action of carbon-dots may be specific to a particular virus or group of viruses and may also depend on the characteristic properties of the carbon-dots used, such as their size, functionalized surface area, and surface charge. Ongoing research continues to investigate the mechanisms of action of carbon-dots as antiviral agents in order to develop effective strategies for countering viral infections.

Antibacterial activity of Carbon-Dots:

Carbon-dots have proved interesting antibacterial activity against a wide range of pathogenic bacteria. Their antibacterial activity can be attributed to several mechanisms of action. Firstly, carbon-dots can act as direct antimicrobial agents, inhibiting bacterial growth and inducing bacterial cell death [121-124]. Their high specific surface area allows greater contact with bacterial membranes, facilitating adhesion and penetration inside cells. Once inside, carbon-dots can damage cell membranes and alter ion homeostasis, leading to loss of integrity and bacterial cell death [125].

In addition, carbon-dots can generate reactive oxygen species (ROS) such as singlet oxygen ($^1O_2$) and free radicals [126], which can cause oxidative stress in bacterial cells. ROS generated by carbon-dots can damage biomolecules essential for bacterial survival, such as lipids, proteins, and nucleic acid, causing disruption of cellular functions and bacterial cell death (**Figure 1.11**).

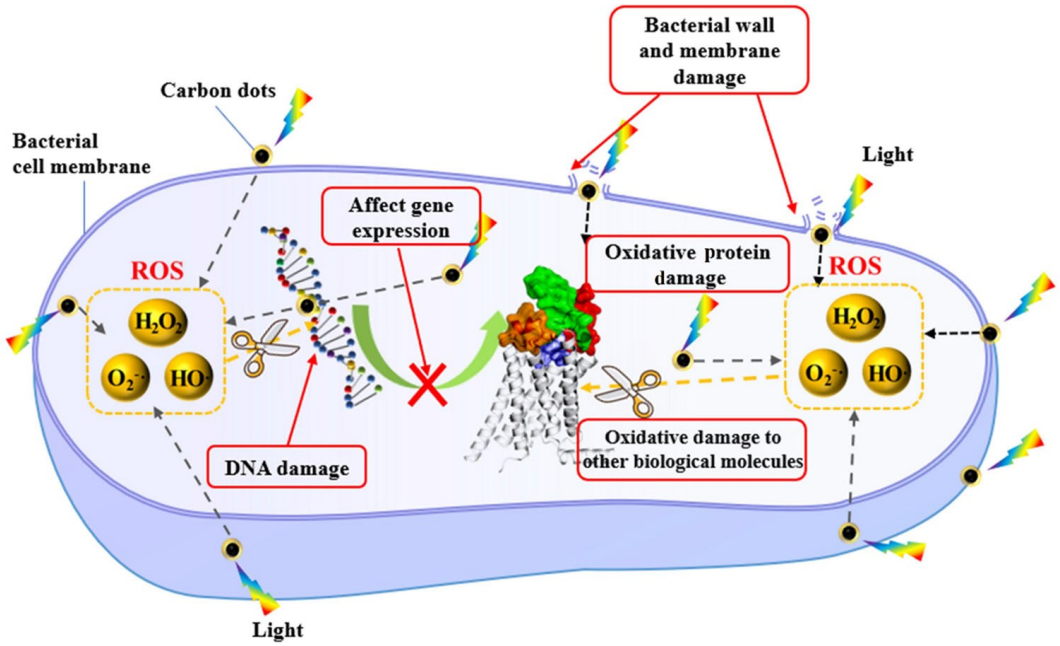

Figure 1.11 Cartoon illustration of the mechanism of action for CDs photoactivated antibacterial activities. Adhesion of CDs to the bacterial surface and visible-light-induced generation of ROS. CD, carbon dot; ROS, reactive oxygen species. Image reproduced with permission of Ref 126.

Moreover, functionalization of carbon-dots can contribute to antibacterial activity through the introduction of specific functional groups that interact with bacterial components [127-130]. For example, amine or carboxyl groups can promote interaction and selective adhesion to bacteria, increasing the antibacterial efficacy of carbon-dots.

The antibacterial activity of carbon-dots has been demonstrated both in vitro and in vivo, with promising results against Gram-positive and Gram-negative bacteria, including antibiotic-resistant pathogens [131].

Antifungal activity of Carbon-Dots:

Carbon-dots have also been shown to possess antifungal activity against pathogenic molds and fungi. Inhibitory effects on the growth and germination of fungal spores have been observed. The antifungal activity of carbon-dots may result from their

ability to interfere with mold life processes, such as cell wall synthesis and cell division [132-135]. In addition, carbon-dots can induce ROS production in fungal cells, causing oxidative damage and fungal cell death.

Mechanisms of action of Carbon-Dots as antimicrobial agents:

The mechanisms of action of carbon-dots as antimicrobial agents vary depending on the type of microorganism being targeted (**Figure 1.12**). However, some common mechanisms include generation of ROS, inhibition of bacterial or viral adhesion to host cells, damage to the bacterial or fungal cell membrane, and inhibition of key enzymes involved in microbial metabolic processes [136, 137].

Carbon-dots conjugated to other nanoparticles, which often already possess antimicrobial properties, allows them to increase their efficiency, selectivity, and biocompatibility. Indeed, the use of these carbon-based nanomaterials represents a new frontier in fighting viruses, bacteria and fungi, finding wide use with various noninvasive therapies that use light as a primary resource [138]. Their potential in counteracting microbial infections opens new perspectives for the development of innovative and sustainable antimicrobial treatments.

Reactive Oxygen Species

The formation of reactive oxygen species (ROS) by carbon-dots is one of the mechanisms by which these nanomaterials can exert their antimicrobial activity [139-141]. ROS generation by carbon-dots may involve several processes, including oxidation of the surface functional groups of carbon-dots and ROS production by photoinduced reactions (**Figure 1.12**).

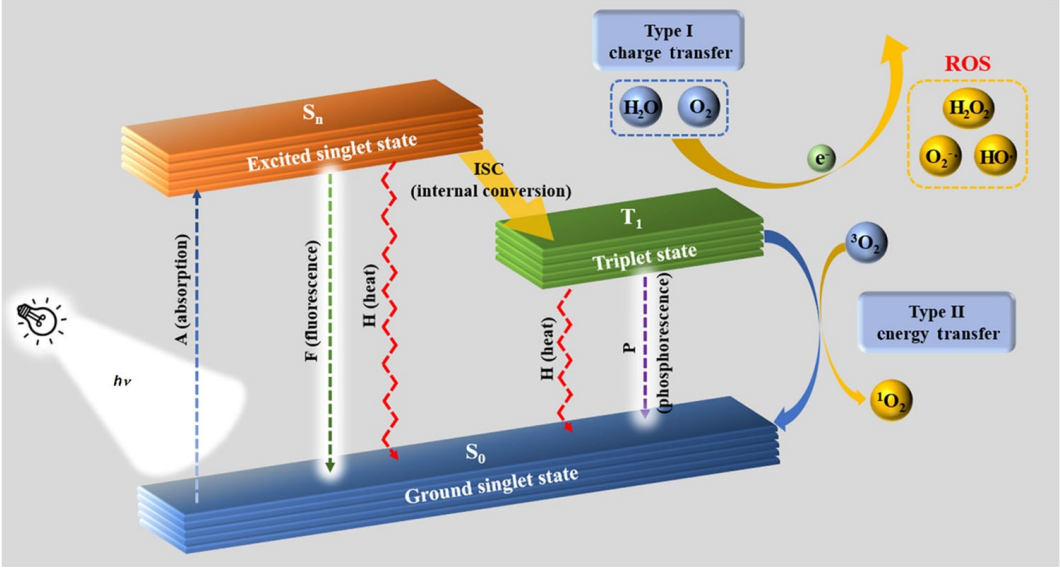

Figure 1.12 Adapted Jablonski diagram showing the photochemical and photophysical mechanisms of antimicrobial photodynamic therapy. Image reproduced with permission of Ref 126.

Carbon-dots have surface functional groups, such as hydroxyl groups (-OH), carbonyl groups (-C=O) and carboxyl groups (-COOH). These functional groups can undergo oxidation reactions in the presence of oxidizing species, such as molecular oxygen (O_2) or hydrogen peroxide (H_2O_2) [142, 143]. During these oxidation reactions, electron transfers occur, producing ROS such as superoxide anion (O_2^-), hydrogen peroxide (H_2O_2) and hydroxyl anion (OH^-). These ROS species can damage target microorganisms through oxidative reactions.

The carbon nanoparticles can also generate ROS through photoinduced reactions when excited by an energy source, such as ultraviolet or visible light. During excitation, electrons in carbon-dots are excited to higher energy levels [144, 145]. Then, the excited electrons can interact with molecular oxygen (O_2) or other molecules in the surrounding environment, generating ROS such as superoxide anion (O_2^-) and hydroxyl anion (OH^-). The production of photoinduced ROS by carbon-dots can contribute to antimicrobial efficacy, as the ROS generated can damage target microorganisms.

The formation of ROS by carbon-dots depends on various factors, such as the chemical composition of carbon-dots, their size and the presence of other reactive substances in the surrounding environment [146, 147]. In addition, the optical and photochemical properties of carbon-dots influence the amount and type of ROS generated. Among all the ROS that can be produced, singlet oxygen is the most interesting, from an antimicrobial point of view, because of its efficient antioxidant activity [148].

Singlet Oxygen generation

Carbon-dots can generate singlet oxygen ($^1O_2$) as one of the reactive oxygen species through a process known as oxygen photosensitization (**Figure 1.13**). The formation of $^1O_2$ by carbon-dots can involve several mechanisms, including energy and electron transfer processes [149, 150].

As a consequence of the UV and/or visible light absorption the electrons in the carbon-dots, can be excited to higher energy levels. During the relaxation process, the excited electrons can release energy in the form of phosphorescence or transferr it to nearby molecules, such as molecular oxygen (O_2). As a consequence of the energy transfer, molecular oxygen can be converted into its excited state, also known as singlet oxygen $^1O_2$, where all the electrons are spin paired [151].

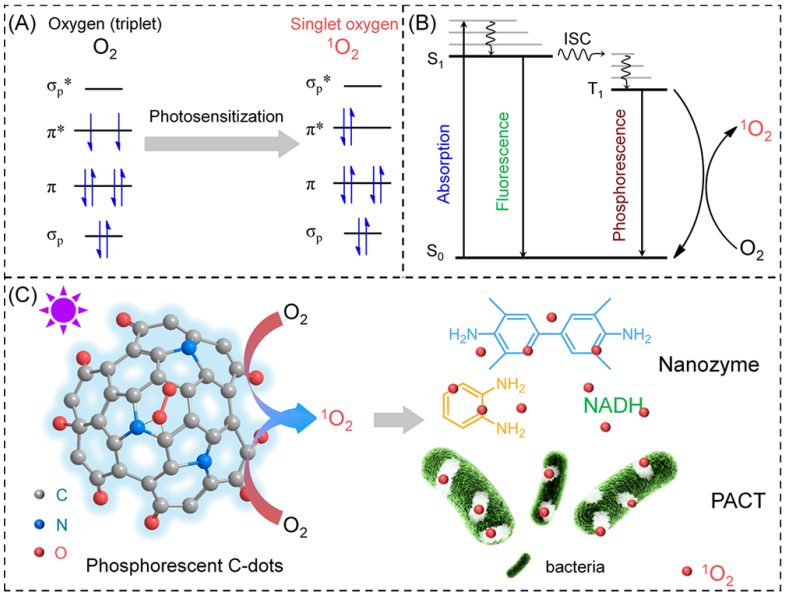

Figure 1.13 Schematic Illustration of Photosensitized Oxygen Activation with Water-Soluble C-Dots: (A) Electron Configuration Change during Photosensitized Oxygen Activation; (B) Jablonski Energy Diagram of Phosphorescence and Singlet Oxygen; and (C) Photosensitized Oxygen Activation with Water-Soluble CDots for Nanozyme and Antimicrobial Photodynamic Inactivation. Image reproduced with permission of Ref 151.

Carbon-dots can also generate $^1O_2$ by electron transfer. [152]. In this case, the excited electrons can react directly with molecular oxygen (O_2), transferring an electron to oxygen and forming a superoxide anion (O_2^-). The superoxide anion can undergo further reactions and transform into $^1O_2$.

The formation of $^1O_2$ by carbon-dots can be influenced by various factors, such as the chemical composition of carbon-dots, their size, and the presence of other reactive species in the surrounding environment [153]. Phosphorescence is one of those properties of carbon-dots that most affect the promotion of singlet oxygen. This is due to the fact that the energy absorbed by the dot, is released more slowly over time than the fluorescence property alone, thus increasing the likelihood of exciting atmospheric oxygen, which is in a stable triplet state, to a reactive singlet state [151]. In addition, the optical and photochemical properties of carbon-dots,

such as the energy band gap and the characteristic optical absorbtion, affect the generation efficiency of $^1O_2$ production [154].

Singlet oxygen ($^1O_2$) is a very reactive species that can damage target microorganisms, with a much longer lifetime than other ROS [155]. The formation of $^1O_2$ by carbon-dots can contribute to the antimicrobial activity of these nanomaterials, as $^1O_2$ can react with biomolecules within microorganisms, causing oxidative damage and microbial cell death [156].

Functionalized surfaces

Surfaces functionalized with nanoparticles represent a promising frontier in the fight against the spread and proliferation of viruses and bacteria [157]. This innovative technology uses charged or chemically treated nanoparticles to impart antimicrobial and antiviral properties to the surfaces to which they are applied [158-160]. The use of silver, copper, and zinc nanoparticles, among others, has been extensively studied for their ability to destroy viruses and bacteria through several mechanisms, including inhibition of cell reproduction and disruption of the cell membrane [161-164]. Although these nanostructured systems are being studied intensively, their real-world application is really difficult, as there are several critical aspects which still need to be optimized:, 1) the chemical instability of the nanoparticles, which often lose their antimicrobial activity once they have accomplished it; 2) the poor mechanical properties of the functionalized surfaces, which exhibit a low resistance to scratching, and the adhesion on substrates, which is often lead to delamination of the functional coatings [165, 166]. Carbon-dots represent a promising alternative to metal-based nanoparticles with antimicrobial activity [167] and, considering the high biocompatibility, one of themain prospected applications involving the use of carbon-dots is the design of active surfaces for food packaging [168-172].

Carbon-dots with antimicrobial properties, applied to surface functionalization, have been already used to counteract the proliferation of bacteria [173]. To achieve this goal, carbon-dots were embedded within a hydrogel made by a polymer matrix. Similar result was obtained using carbon-dots conjugated to zinc oxide

nanoparticles, to fight gram-positive and gram-negative bacteria [174]. Carbon-dots were also used for functionalization of nanocellulose-based films (**Figure 1.14**) [175] enhancing the antimicrobial properties of nanocellulose against gram-positive L. monocytogenes and gram-negative E. coli bacteria. Interestingly, it was observed that, the surfaces functionalized with Carbon-dots/nanocellulose showed a better antibacterial activity then the surfaces functionalized with carbon dots only.

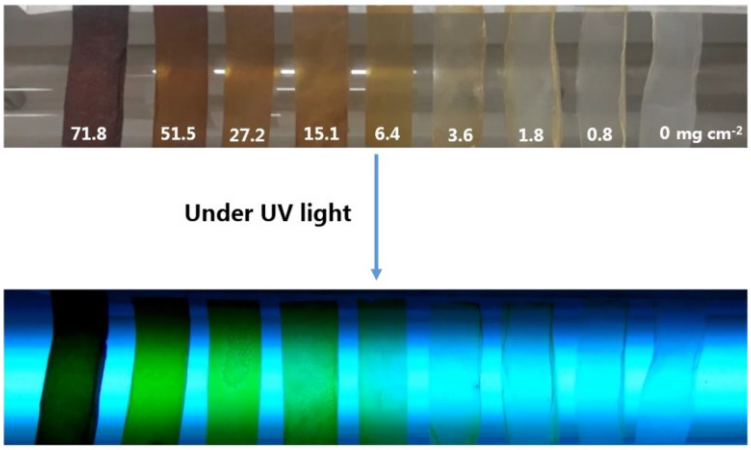

Figure 1.14 The photographs of the polymer membrane with different CDs loading capacities solutions under white light and UV lamp. Image reproduced with permission of Ref 175.

Chapter 2: Experimental

A rational approach to the carbon dots precursors

The present thesis is based on the use of a very simple aminoacid, called glycine, to form carbon-dots featured by virucidal and antiviral properties. Discovered in 1820 by French chemist Henri Braconnot, glycine, like all amino acids, has an amine group ($-NH_2$) and a carboxyl group (-COOH), as shown in **Figure 2.1**. Because of the two hydrogen atoms in the α carbon, glycine is a non-chiral molecule, has no steric hindrance and is apolar.

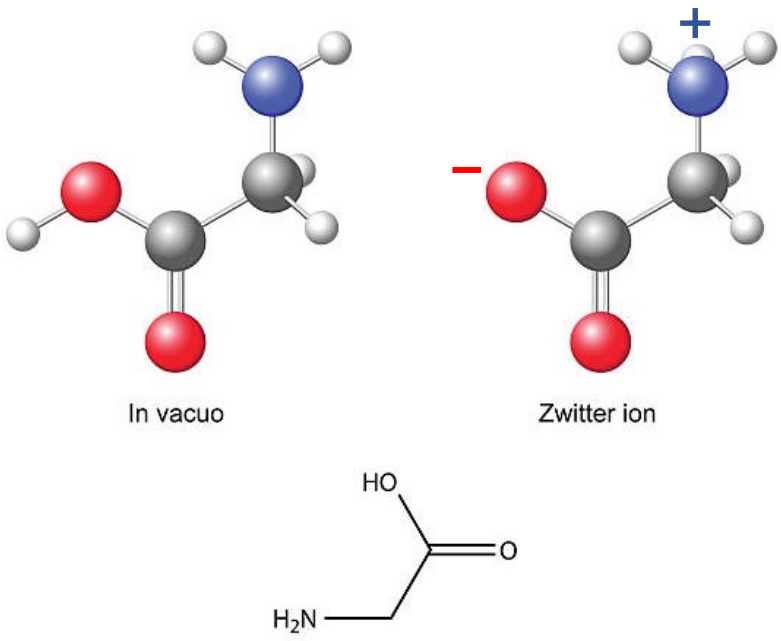

Figure 2.1 Illustration of the structure of the glycine molecule, in neutral and in zwitterionic form.

The goal of this thesis work is to exploit this amino acid as the building block of the complex structure that, after synthesis, will form the carbon-dots. To do this, the carboxyl and amine groups of glycine have been both involved to obtain amide-type covalent bonds. The functional properties of the carbon-dots have been

obtained by a careful selection of the co-precursors, to be reacted together with glycine. The co-precursors used have been: 1,5-diaminonaphthalene and glycyrrhizic acid.

1,5-diaminonaphthalene (**Figure 2.2**) is an organic, aromatic compound that has two condensed benzene rings and two amine groups in position 1 and position 5. It has structural isomers, such as 1,8- 1,2- or 2,3-diaminonaphthalene. It is obtained starting from 1-aminonaphthalene through a nitration reaction, and in the polymer industry it is used as a precursor to polyurethanes.

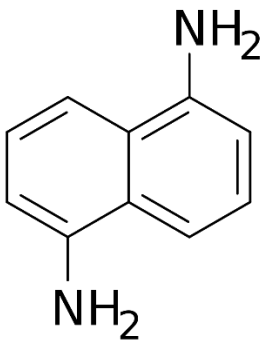

Figure 2.2 Illustration of the structure of the 1,5-diaminonaphthalene molecule.

The prospected function of 1,5-diaminonaphthalene in the carbon-dot design is to build an aromatic-type structure and ensure absorption in the ultraviolet range with subsequent emission in the visible. The formation of 1,5-diaminonaphthalene-based carbon-dot was based on an amide reaction between the carboxylic group of glycine and the amine group of 1,5-diaminonaphthalene, knowing that secondary polymerization reactions could occur leading to products such as poly-diaminonaphthalene and poly-glycine (**Figure 2.3**) [176, 177]

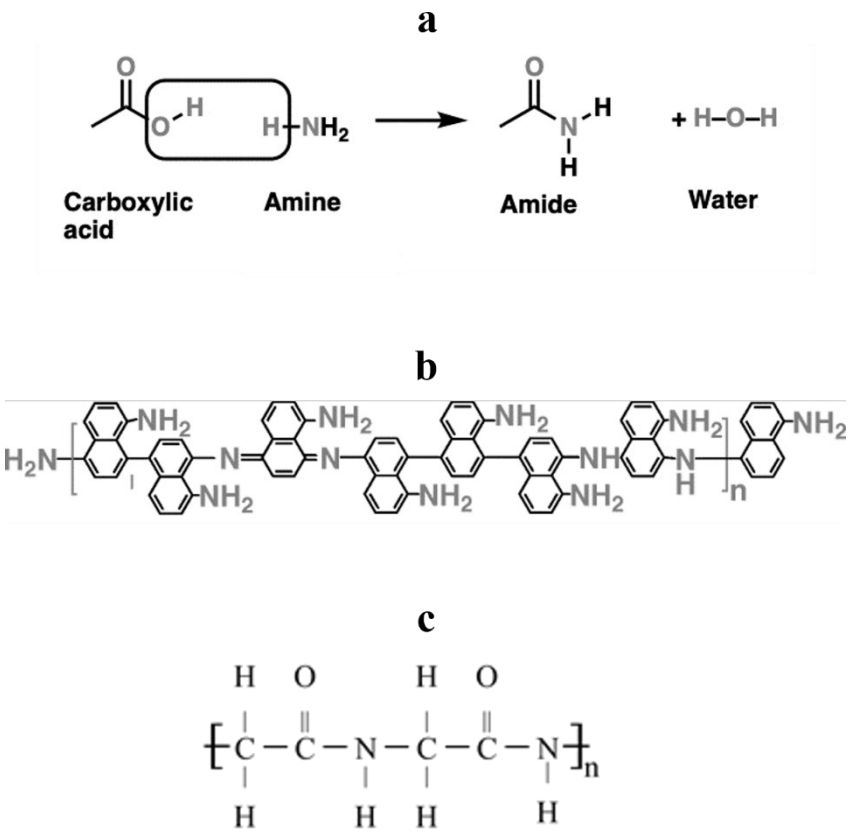

Figure 2.3 Illustration of the a) amidic reaction and the structure of the b) poly-1,5-diaminonaphthalene and c) poly-glycine.

Glycyrrhizic acid (**Figure 2.4**) is a compound obtained by the conjugation of two smaller molecules, glucuronic acid and glycyrrhetinic acid, leading to the formation of a triterpene saponin with three carboxyl groups [178]. It is obtained from the extract of the root of the licorice plant, Glycyrrhiza Glabra, a plant belonging to the Febaceae family [179]. It is reported in the literature that this acid exhibits anti-cancer, anti-inflammatory, antiviral and antibacterial properties. It is used both in pharmaceuticals for its medical properties and in food, as it is fifty times more sweetener than sucrose [180].

It has eight reactive sites: three carboxyl sites that can give amide reactions; five hydroxyl sites that can give Maillard reactions.

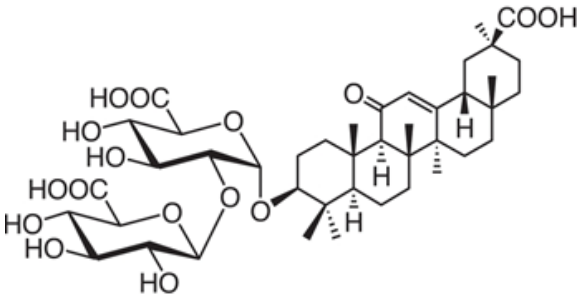

Figure 2.4 Illustration of the structure of the glycyrrhizic acid.

The function of this compound is to react with the amine group of glycine so that its antiviral and antibacterial properties can be transferred to the synthesized nanoparticles. The amidation between glycine and glycyrrhizic acid is not obvious as, in theory, polymerization of glycine into poly-glycine and glycyrrhizic acid into poly-glycyrrhizic acid could also occurs.

Once the desired nanoparticles have been obtained and their biocidal properties verified, they have been further used for surface functionalization.

Chemicals

Glycine (purity 98.5%), boric acid (purity 99.5%) and glycerol (purity 99.5%) were purchased from Carlo Erba Reagents. 1,5-diaminonaphthalene (purity 97%), glycyrrhizic acid ammonium salt from glycyrrhiza root (licorice) (purity >95%), TEOS (Tetraethoxysilane) (purity 98%), APTES ((3-aminopropyl)triethoxysilane) (purity 99%), hydrochloric acid (37%) and PVA (polyvinylalcohol) partially hydrolyzed (Mw approx. 30000) were purchased from Sigma Aldrich. All the chemicals were used without any further purification. Milli-Q water was used for synthesis and analysis.

Microwaves approach

A microwave synthesis technique was chosen for the synthesis of the first system, composed by glycine and 1,5-diaminonaphthalene. This choice was made

empirically, as we observed that, with other synthesis techniques, poly-glycine and poly-1,5-diaminonaphthalene byproducts were present in larger quantities.
For this synthesis, glycine and 1,5-diaminonaphthalene were solubilized in milli-Q water in the molar ratio 1:1, according to the following quantities: 0.15g of glycine and 0.31g of 1,5-diaminonaphthalene, in 20mL of milli-Q water.
The reaction was catalyzed using two different acids, hydrochloric acid and boric acid, according to the molar ratios shown in **Table 1**.

	1,5-diaminonaphthalene	**Glycine**	**Catalyst**
CD-Boron	1	1	1 (boric acid)
CD-Chlorine	1	1	0.2 (hydrochloric acid)

Tabel 1 The table shows the two compositions of the precursors used to obtain the two carbon-dots, the one catalyzed with boric acid (CD-Boron) and the one catalyzed with hydrochloric acid (CD-Chlorine).

After solubilization, which was performed with the assistance of an ultrasonic bath, the sample was placed in a 250 mL beauta and treated at 1000W for 3 minutes in a classic kitchen microwave oven. (**Figure 2.5**).

Figure 2.5 Representation of a kitchen microwave oven used for the synthesis.

The product obtained from the reaction was a dark purple powder when the reaction was catalyzed by hydrochloric acid (37%), and a dark brown powder when catalyzed by boric acid.

In both cases, the product obtained were solubilized in 20 mL of milli-Q water, filtered through a cellulose syringe filter with a pore size of 0.22 μm, and finally placed inside a dialysis membrane with a cut-off of 2000 Daltons and dialyzed against milli-Q water for 24 hours, changing the water every 2 hours.

The dialyzed solution was then placed in a silicone mold and placed in an oven at 60°C for 14 hours to obtain a black powder for the reaction catalyzed by hydrochloric acid and a brown powder for the reaction catalyzed by boric acid.

The resulting products were finally characterized.

A schematic flowchart of the synthesis is reported in **Figure 2.6**.

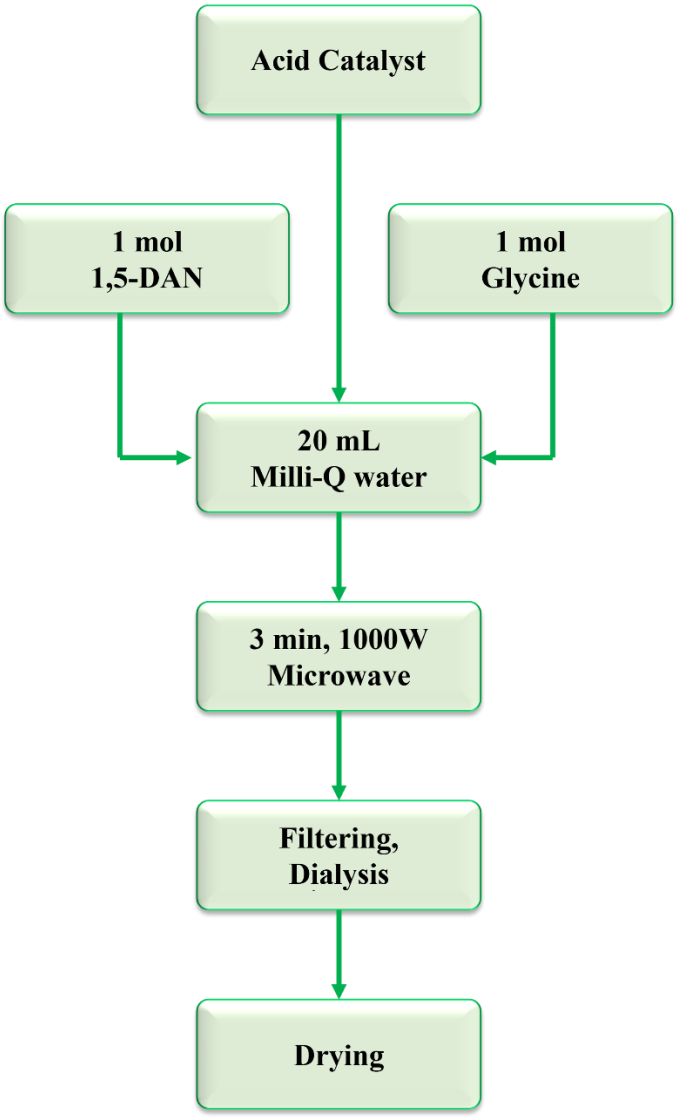

Figure 2.6 Flowchart of synthesis by microwave method.

Hydrothermal approach

The second system, composed of glycine and glycyrrhizic acid, was treated by a classical hydrothermal reaction.

In this case, the molar ratios were chosen on the basis of the results obtained from the microwave system. .

In a typical synthesis 1.67 g of glycyrrhizic acid were mixed with 0.15 g of glycine (1:1 molar ratio) and solubilized in 10 mL milli-Q water. The reaction was catalyzed

by boric acid in a 1:1 molar ratio with glycine and glycyrrhizic acid, based on the results obtained from microwave synthesis. The resulting solution was placed in a Teflon jar and finally in a stainless-steel autoclave (**Figure 2.7**). Then it was treated at 180°C for 8 hours in an oven, after a ramp of 10°C per minute up to 180°C.
The reaction conditions were chosen on an empirical basis, as 180°C and 8 hours were the minimum conditions to obtain particles with fluorescence properties.

Figure 2.7 Representation of an autoclave used for synthesis.

The product obtained was filtered through a cellulose syringe filter with a pore size of 0.22 μm and finally placed inside a dialysis membrane with a cut-off of 2000 Daltons and dialyzed against milli-Q water for 24 hours, changing the water every 2 hours.
The dialyzed solution was then placed in a silicone mold and in an oven at 60°C for 14 hours to obtain a black powder that was used for characterizations. A schematic flowchart if the overall synthesis is reported in **Figure 2.8**.

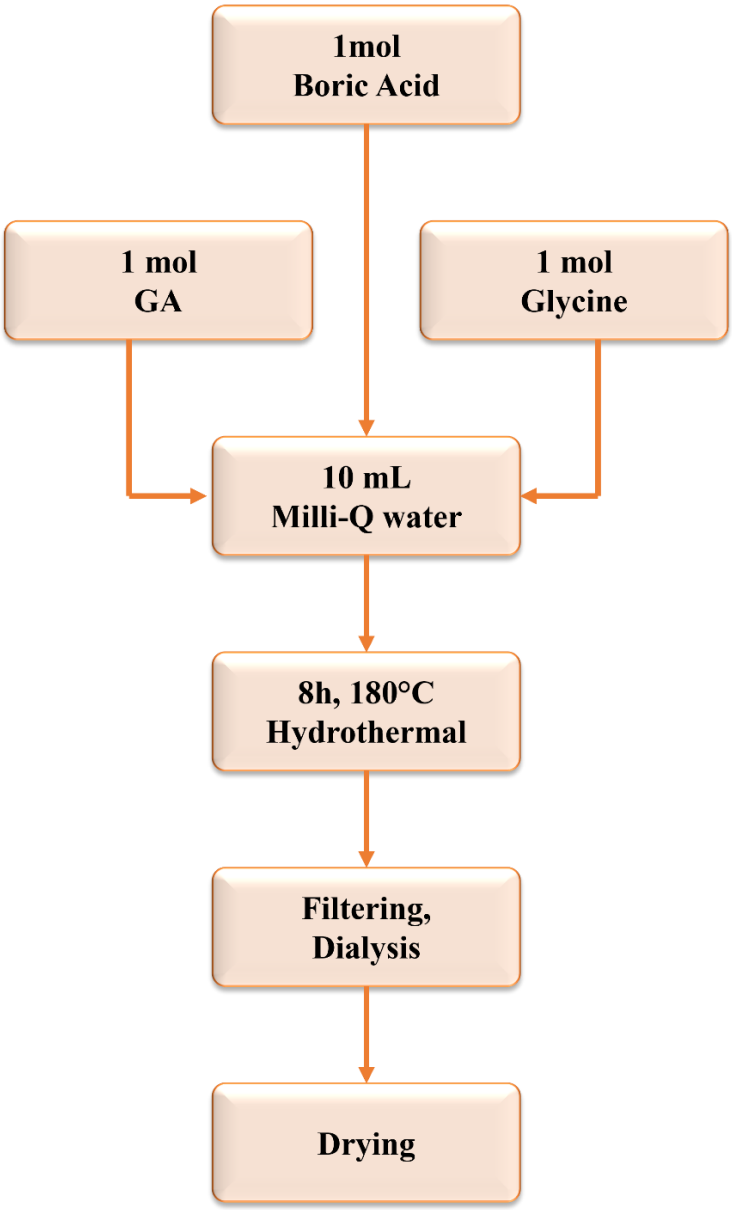

Figure 2.8 Flowchart of synthesis by hydrothermal method.

Surface engineering

To obtain active surfaces, carbon-dots were directly grafted on a pre-treated substrates or embedded into matrices to form coatings. The surface engineering was therefore designed along two paths: the first involves the use of covalent bonding

between a pre-treated silicon wafer, used as “ideal” surface, and the nanoparticle, while the second involves embedding the nanoparticles in a polymer matrix.
For the first pathway, a piece of single-crystal silicon wafer, size 1.5 cm x 3 cm, was left in 1M hydrochloric acid for 12 hours. It was then washed with ethanol and dried in an oven at 60°C for 1 hour.
Substrate deposition was done through a two-step process: in the first step a TEOS film was deposited; in the second step a second layer was deposited using APTES. This double step allows to have a larger amount of amine groups (derived from APTES) on the surface of the film.
The deposition was made according to the following sol-gel method:

- 10mL of TEOS were added to 15 mL of ethanol (EtOH) and 2.5mL of 1M HCl;
- The solution was placed under stirring for 1 hour and 30 minutes at room temperature;
- The formed sol was used to coat the silicon substrate through dip-coating technique, with a withdrawal rate of 100 mm/min;
- The deposited film was finally treated at 350°C for 2 hours.

Afterwards the silica layer was modified with amino groups thanks to a chemical functionalization with a sol containing aminopropyl triethoxisilane (APTES)

- 5 mL of APTES were added to 20 mL of EtOH and 1.5mL of 1M HCl;
- The solution was placed under stirring for 1 hour at room temperature;
- The formed sol was used to coat the silicon substrate through dip-coating technique, with a withdrawal rate of 100mm/min;
- The deposited film is finally treated at 120°C for 1 hour.

In this way, a TEOS/APTES film was obtained in order to have -NH_2 groups that could be exploited as the anchoring sites for the nanoparticles.

Once the surface of the silicon substrate was prepared, an EDC/NHS coupling reaction was performed to take advantage of the carboxyl groups of the carbon-dots and the amine groups of the TEOS/APTES film. The EDC is the coupling reagent that allowas to activate the carboxyl group of the carbon-dots. After the activation, the EDC is substituted by the NHS, which is a better exiting group than the EDC. When the so functionalized carbon-dot reacts with the amine group of the APTES, the NHS is removed and the amidation reaction occurs.
In an example reaction:

- 200 mg of powder containing the carbon-dots, were added to 200 mg of EDC and 120 mg of NHS and then solubilized in 10 mL of DMF (N,N-dimethylformamide);
- Then, the substrate with the TEOS/APTES film was added to the reaction solution;
- The reaction was placed at reflux and heated to 70°C for 24 hours under stirring;
- At the end of the reaction, the substrate was recovered and dried in an oven at 60°C for 1 hour (**Figure 2.9**) before being characterized.

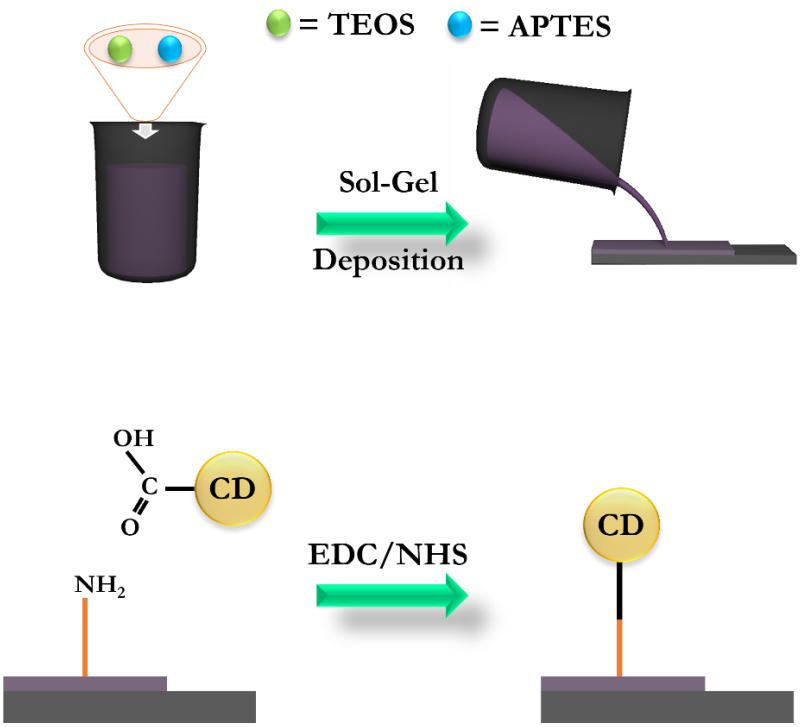

Figure 2.9 The figure shows the steps of the sol-gel reaction for obtaining the film and the reaction for anchoring the dots on the surface.

For the second approach which involves carbon-dots embedding into a polymeric matrix, polyvinyl alcohol (PVA) was chosen as the polymer.

The aim was to produce a thick film (about 0.5-1 mm) featuring tough mechanical properties to coat the surface as a standard polystyrene film.

With respect to the sol-gel film, this coating woud have the advantage to be easily adapted to a wide variety of surfaces, including those of vegetables and fruits in food packaging.

The films were produced according to the following process:

- 10 g of PVA were added to 2g of glycerol and placed in a 250 mL flask;
- 100 mL of Milli-Q water was then poured into the flask, and the resulting solution was placed under stirring for 2 hours;
- After that, the flask was placed in the oven at 60°C overnight.

To obtain the thick films (**Figure 2.10**), 20 mg of carbon-dots powder was solubilized in 20 mL of previously prepared PVA solution and finally placed in a Petri dish with a diameter of 9 cm. The solutions thus deposited were placed in an oven at 60°C overnight, resulting in films of about 1 mm thickness.

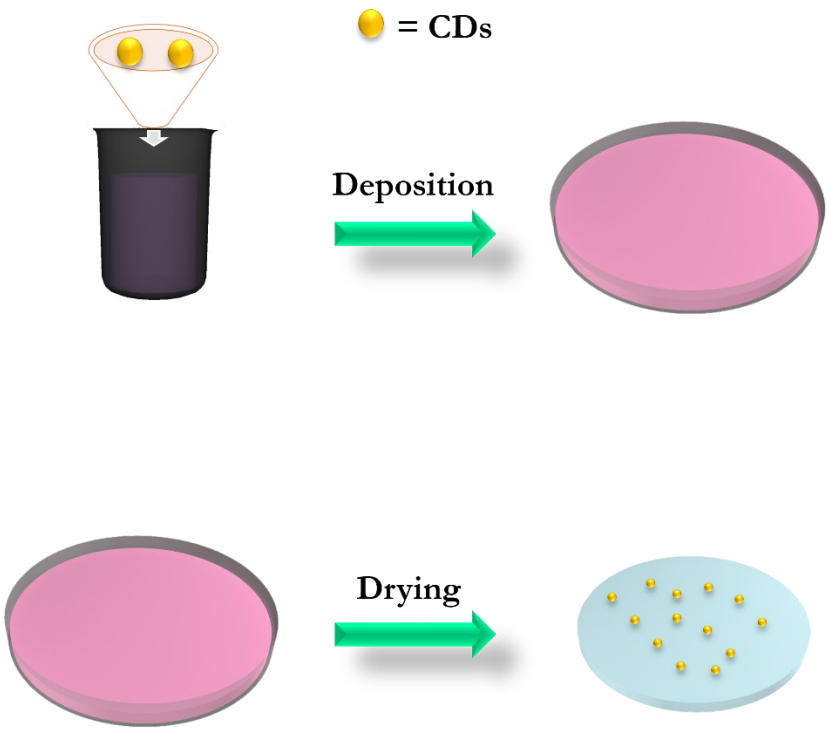

Figure 2.10 Diagram representing the procedure for obtaining the self-standing surface.

Antiviral, Antibacterial and Antifungal assay

Biological tests were carried out at three different locations according to specific procedures.

Antiviral, antibacterial, and antifungal properties were carried out both on the dot as is and on the functionalized surfaces.

Prior to antiviral analysis, a cytotoxicity measurement was performed, taking the result obtained as a reference for all biological measurements.

Cytotoxicity and antiviral activity of the material CD-Boron were studied in collaboration with the company Virostatics srl. Cytotoxicity of the material CD-GA was studied by the laboratory of obstetrics and clinical gynecology of the University of Sassari; antibacterial susceptibility was evaluated in the laboratory of ICCRAM at Burgos University; antifungal activity was evaluated in the laboratory at University of Sassari.

Cytotoxicity:

Cytotoxicity of the material CD-Boron was evaluated using Vero E6 cells (Cercopithecus aethiops, kidney, ATCC CRL-1586) as a reference.

The cell line was routinely maintained in DMEM supplemented with 1% glutamine, 1% penicillin/streptomycin and 10% fetal bovine serum. After the cells were grown, they were placed inside a 96-well plate and allowed to grow for another 24 hours in order to achieve optimal cell density. After this period, the cells were subjected to different concentrations of the nanomaterial and were left to incubate for 72 hours. The measurement was performed in triplicate. Cytotoxic effect was evaluated through microscopy observation (determination of cell monolayer integrity). A cytotoxic concentration 50% (CC50, concentration resulting in 50% loss of cell viability compared to untreated control) was calculated.

Cytotoxicity of the material CD-Boron was evaluated using Vero E6 cells (Cercopithecus aethiops, kidney, ATCC CRL-1586) as a reference.

Antiviral activity:

The virucidal activity of the tested nanomaterials was evaluated by modifying the guidelines given in EN 14476:2013+A2:2019/UNI EN 14476:2019 [181] for testing chemicals as disinfectants.

A volume of viral suspension (as indicated for each experiment below in results section) of SARS-CoV-2 (Original strain or Delta strain) was put on a 96-well plate lid (12x8 cm). A volume of nanomaterial was added to the viral suspension (at the indicated volume and final concentrations below in results section).

Suspensions were then left in the dark or exposed to visible (450 nm) or ultraviolet light (365 nm) for the time indicated in each experiment (range 2-5 minutes).
Culture medium was used as control, added to the viral suspension and exposed to the dark or to visible/ultraviolet light as with nanomaterials.
A general scheme of the experiment setup is shown in **Figure 2.11**.

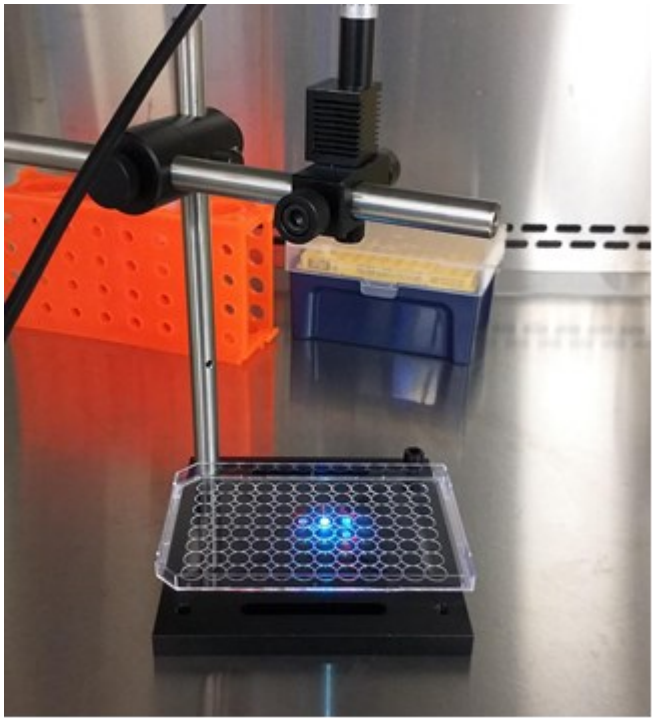

Figure 2.11 Real illustration of the operational setup for antiviral measurement.

After an additional 5-minute incubation, viral suspensions were collected, and viral titer was determined according to the methodology described below.
An in vitro system was employed to determine viral titer of SARS-CoV-2 suspensions and it was determined according to the following scheme:

- Vero E6 cells (kidney epithelial cells from African green monkey, ATCC CRL-1586) were used for the test;
- On day 1 of the experiment, cells were transferred in 96-well plate (20.000 cells per well);

- On day 2 cells were infected with the serial viral dilutions (10-2, 10-3, 10-4...) in 6-well replicates for each condition;
- After three additional days infection in each test well was determined by observation of the cytopathic effect.

Infection data were employed to build the following example table:

A	B	C	D	E	F
Viral dilution	Number of affected wells	Number of unaffected wells	Cumulative number of affected wells	Cumulative number of unaffected wells	Affected ratio (%)
10^{-2}	...	...	...	...	...
10^{-3}	...	...	...	...	...
10^{-4}	...	...	...	...	...
10^{-5}	...	...	...	...	...
...	...	...	...	...	...

Put in the first row the virus dilution with 6/6 affected wells and in the last row that one with 0/6 affected.

Write in column B the number of affected wells and in column C the number of unaffected wells.

Column D represents the cumulative number of affected wells calculated by adding numbers starting at the bottom of column B and adding up.

Column E represents the cumulative number of unaffected wells calculated by adding numbers starting at the top of column C and adding down.

Column F represents the cumulative ratio of affected wells (%): number from column D divided by the total of column D + E and express as %.

Calculate the proportionate distance between the two dilutions nearest to 50% using value from column F:

$$\frac{(\%\ \text{affected next above 50\%}) - 50\%}{(\%\ \text{affected next above 50\%}) - (\%\ \text{affected next below 50\%})}$$

Add the negative exponent of the viral dilution next above 50%.
Use the calculated value as exponent with base 10 to obtain the virus titer within the infection volume (i.e., TCID50/100 µL).

Antibacterial assay:
For the measurement of antibacterial susceptibility, the Broth microdilution test was performed.
The test was conducted against four different bacteria, two Gram positive (*Staphylococcus Aureus* and *Enterococcus Faecium*) and two Gram negative (*Pseudomonas Aeruginosa* and *Acinetobacter Baumannii*), according to the following procedure:

1. the culture of the bacteria in MHB medium was prepared;
2. the dilution of the carbon-dotss was carried out;
3. inoculation on 96-well plates;
4. incubation at 37°C for 18h;
5. evaluation of antibacterial activity.

The carbon-dots concentrations were chosen based on solubility tests carried out over 24 hours. 1.35 mg/mL and 337.5 µg/mL were chosen as the maximum concentrations for samples CD_GA and CD-Boron and, respectively. The presence of a deposit at the bottom of the well was observed was considered as the proof of the bacterial susceptibility, (**Figure 2.12**).

Figure 2.12 The presence of bacteria is identified by a deposit at the bottom of the well (in this case the well on the right).

Antifungal assay:

The measurement of antifungal activity was evaluated by simulating a real application of the functionalized surface.

In this case, *botrytis cinerea* mold was grown naturally on fresh fruit, strawberries to be specific.

To evaluate the effect of carbon-dots on inhibition of mold growth, a PVA-only film and a PVA film containing the carbon-dots were produced, both of which were used as "membrane caps" of the strawberry container.

The samples were left out of the refrigerator, at room temperature and about 55% humidity, until mold grew in each individual sample.

In addition to the functionalized films, mold growth was also evaluated in the presence of water-solubilized carbon-dots sprayed on fresh fruit with an atomizer.

Characterization techniques

UV-Visible Spectroscopy:

Ultraviolet-visible (UV-Vis) spectra of the samples solubilized in water were measured in absorbance mode from 200 to 600 nm by using a Nicolet Evolution 300 UV−Vis spectrophotometer (Thermo Fisher). A concentration of 0.1 mg mL^{-1} was used for the analysis.

FTIR Spectroscopy:

Absorption Fourier-transform infrared (FTIR) spectra were recorded by a Vertex 70 interferometer (Bruker) in the range of 4000−400 cm^{-1} with a 4 cm^{-1} resolution

and 32 scan. The spectra were recorded using KBr pellets with 1 mg of sample and 500 mg KBr.

Fluorescence Spectroscopy:

Fluorescence analysis of the samples solubilized in water was done using a Horiba Jobin Yvon NanoLog spectrofluorometer with an excitation and emission wavelength from 300 to 700 nm. A concentration of 0.1 mg mL^{-1} was used for the analysis.

Raman Spectroscopy:

The Raman measurement was performed by employing a "Senterra" Raman microscope (Bruker) under a laser excitation of 532 nm (25.0 mW power). The spectra was collected with a resolution of ~3–5 cm^{1}, and an integration time of 15 s. The sample (powder) was deposited onto silicon wafer.

X-ray Photoelectron Spectroscopy (XPS):

X-ray photoelectron spectroscopy (XPS) was carried out in a custom designed UHV system equipped with an EA 125 Omicron electron analyzer with five channeltrons, working at a base pressure of 10-10 mbar. Core level photoemission spectra (C 1s and N 1s) were collected in normal emission at room temperature with a non-monochromatized Al Kα X-ray source (1486.7 eV) and using 0.1 eV steps, 0.5 s collection time and 20 eV pass energy.

Nuclear Magnetic Resonance (NMR):

NMR spectra have been acquired on a Bruker Avance 600 MHz spectrometer ((Bruker Biospin, Karlsruhe, Germany) equipped with a 5 mm BBI probe. All the measures were collected in DMSO solvent. 800 µL were transferred into 5 mm NMR tubes for analysis.

Transmission Electron Microscopy (TEM):

Transmission electron microscopy (TEM) images were acquired with a Jeol JEM 1400 Plus microscope. Once dispersed in a tiny amount of n-octane the samples were dropcasted on a holey carbon-coated copper grid and let evaporate at RT.

Atomic Force Microscopy (AFM):

Atomic Force Microscopy (AFM) were performed with a microscope NT-MDT Ntegra at 0.8 Hz scan speed in semicontact mode, using a silicon tip with nominal resonance frequency of 150 kHz, 5 N m^{-1} force constant, and 10 nm typical curvature radius.

Electron Paramagnetic Resonance (EPR):

EPR spectra were acquired using a Bruker EMX spectrometer operating at X-band (9.5 GHz), equipped with a cylindrical cavity operating at 100 kHz field modulation. All the spectra were recorded at room temperature (RT) with a 10 mW of incident microwave. Experiments were carried out also in static vacuum obtained connecting Suprasil quartz glass tubes to a high vacuum pumping system (residual pressure $P < 10^{-3}$ mbar).

Chapter 3: Results and Discussion

Microwave CDs

Comparison between CD-Boron and CD-Chlorine:

Carbon-dots based on glycine and 1,5-diaminonaphtalene were obtained after microwave treatment with the support of two different catalysts, namely boric acid ($B(OH)_3$) and hydrogen chloride (HCl). Corresponding nanoparticles were therefore named CD-Boron and CD-Chlorine, respectively.

The use of these two precursors, 1,5-DAN and Gly, was designed to take advantage of the possibility of obtaining different structures through amidation reactions. The starting idea was to exploit the $-NH_2$ groups of 1,5-DAN and the -COOH groups of Gly in order to obtain pyridine cyclic structures, with fluorescent properties. Fluorescence is crucial to promote reactive oxygen species (ROS), mainly due to the presence of -COOH groups within the carbon structure of the synthesized nanoparticles.

Several differences can be observed when comparing CD-Boron and CD-Chlorine spectra (**Figure 3.1 a**).

The spectrum of CD-Chlorine is almost superimposable to those of 1,5-DAN, except for a very weak signal with a maximum at about 460 nm, which can be observed in CD-Boron (**Figure 3.1 b**). This signal is compatible with the presence of graphitic or polyaromatic structures in the sample [182].

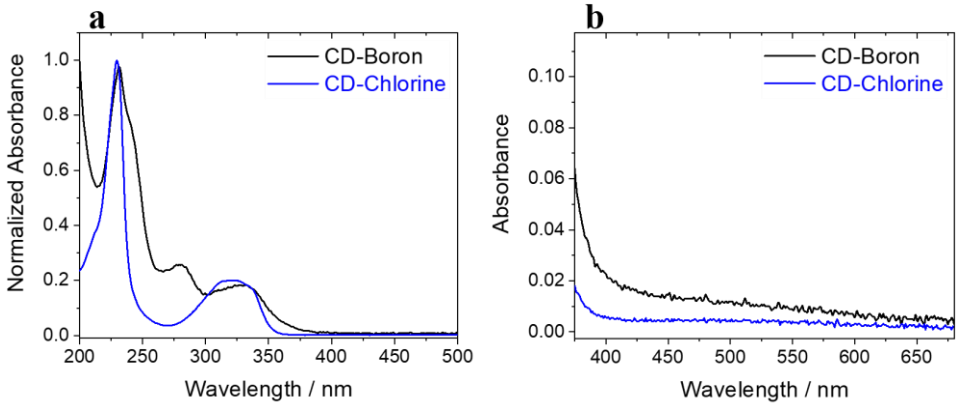

Figure 3.1 The picture shows a) UV-Vis spectra of CD-Boron and CD-Chlorine in the range 200-500 nm; b) UV-Vis spectra of both carbon-dots in the range 375-675 nm.

The fluorescence spectra or responses of the two samples (**Figure 3.2**) are particularly different. As it can be seen, the shape of the excitation signal of CD-Boron is broader than that of CD-Chlorine, which is narrower, while the excitation and emission signals are shifted to higher wavelengths in CD-Chlorine.

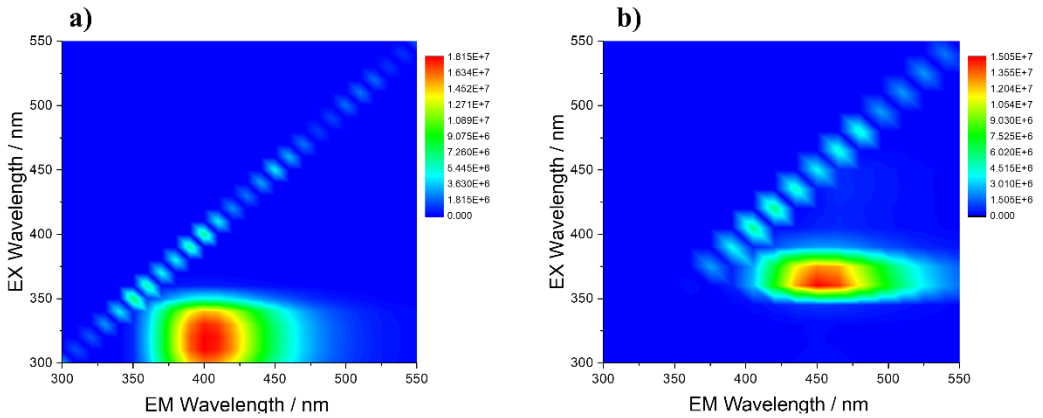

Figure 3.2 The images show the fluorescence 3D maps of a) CD-Boron (excitation = 330 nm; emission 405 nm) and b) CD-Chlorine (excitation = 360 nm; emission 450 nm), in the range of 300-550 nm of excitation and emission.

Figure 3.3 shows the images of the two types of samples as observed by Transmission Electron Microscopy (TEM). The morphologies of the carbon-dots vary in shape and size depending on the catalyst. In the CD-Boron sample, round-shape nanoparticles with a diameter of approximately 18 nm are observed. Conversely, the CD-Chlorine structure is less simple, displaying characteristic morphologies. Larger, elongated structures with low electronic contrast seem to enclose small, high-contrast spherical cores showing an average size below 6 nm.

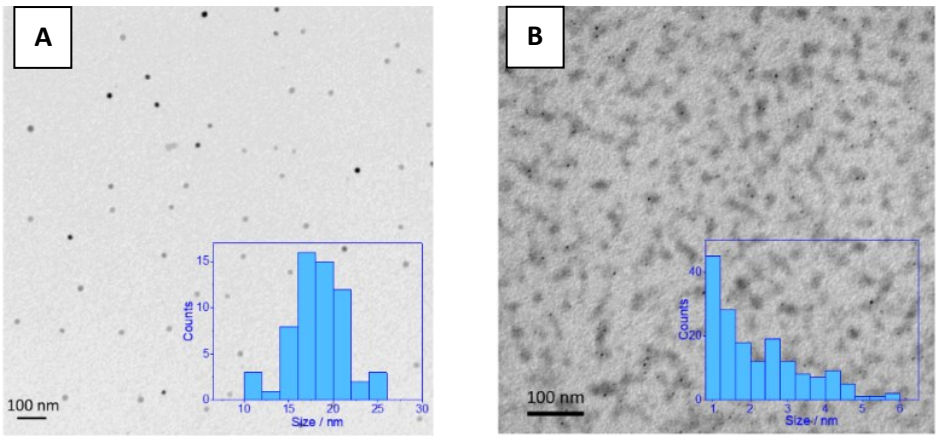

Figure 3.3: a) TEM images of CD-Boron and b) CD-Chlorine. CD-dots with the corresponding size distribution shown in the inset (bar scale 100 nm).

Figure 3.4 b shows the FTIR spectra in the range between 1800 and 1000 cm^{-1}. Carbon-dots spectra are characterized by the superimposition of the main vibrational modes of Gly and DAN. The corresponding -NH_2 scissoring and wagging modes are located at 1626 cm^{-1} and 766 cm^{-1}. Aromatic C=C stretching vibrations typically occur in the range of 1450-1600 cm^{-1} [183]. In CD-Boron, distinctive features emerge from the overlapping of COO and NH_2 bending and stretching modes, located between 1600 and 1575 cm^{-1} [184], with a prominent peak around 1500 stemming from the asymmetrical bending and rocking of the NH_3^+ group. The range between 1500 and 1250 cm^{-1} primarily corresponds to CH_2 stretching and bending, while two additional modes at 1125 and 1042 cm-^{1} persist and can be attributed to C-O and C-N stretching, respectively [185, 186]. In CD-

Chlorine, distinctive absorptions corresponding to the vibrational modes of the DAN monomer are observed. This is particularly noticeable in the spectral range between 1600 and 1500 cm^{-1}, and at lower frequencies between 1200 and 1000 cm^{-1}, where the CO and CN groups of Gly are less prominent compared to CD-Boron. In general, the vibrational spectra indicate the robust polymeric nature of both CDs, leading to a broadening and reduction in the detail of the characteristic monomer modes.

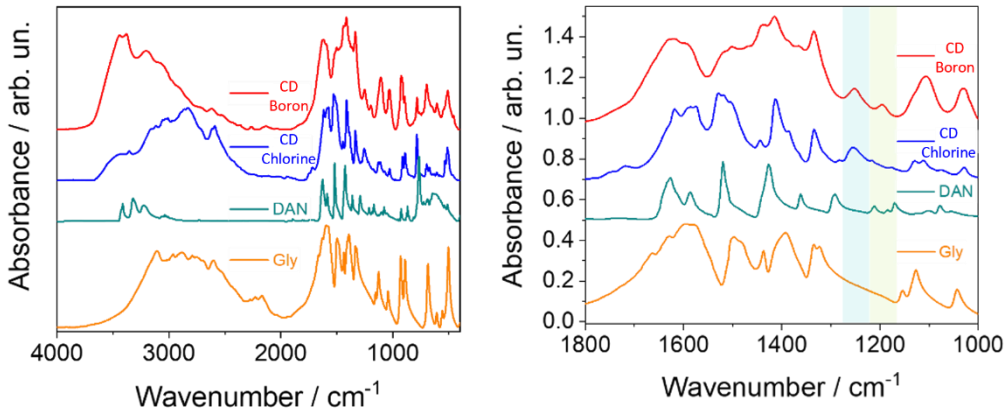

Figure 3.4: a) FTIR in the range 4000 – 400 cm^{-1}; b) FTIR spectra recorded in the region between 1800 and 1000 cm-1.

Additionally, it can be inferred that CD-Boron exhibits a higher proportion of Gly in both its monomeric and linear polymeric forms. Moreover, in CD-Chlorine, DAN seems to maintain its monomeric form. Lastly, two modes at 1252 and 1195 cm^{-1} are noteworthy, as they do not appear in the precursor materials. The former is detectable in both CDs, whereas the latter is exclusively found in CD-Boron and is tentatively attributed to Aryl-O-R ether bonds [187], probably formed with a condensation process between DAN and Gly without amide bond formation. The second is attributable to Aryl-OH-type stretching, which can take place as an effect of a strong oxidative process of DAN.

The ^{1}H NMR spectra of CD-Chlorine shows signals ascribed to glycine methylene protons at 3.62 ppm (**Figure 3.5**). By comparing the spectrum of free glycine in

DMSO we believe that this downfield shifted signal can be explained by linear polymeric chains of glycine molecules variably intercalated by DAN.

Very weak signals at 3.94 and 4.39 ppm might be assigned to α-CH_2 of terminal glycine molecules. The absence of the -NH_2 signal of DAN at 5.4 ppm [188] indicates the presence of Gly-DAN complexes, which further supports the formation of amide groups between the carboxylic and ammine groups of Gly and DAN, respectively. At 168.8 ppm, both the ^{13}C-NMR spectrum and the ^{1}H- ^{13}C heteronuclear single quantum coherence (HSQC) maps of CD-Chlorine exhibit unambiguous signals from amide carbonyl carbons (**Figure 3.6**). In contrast, no signal from free Gly could be detected.

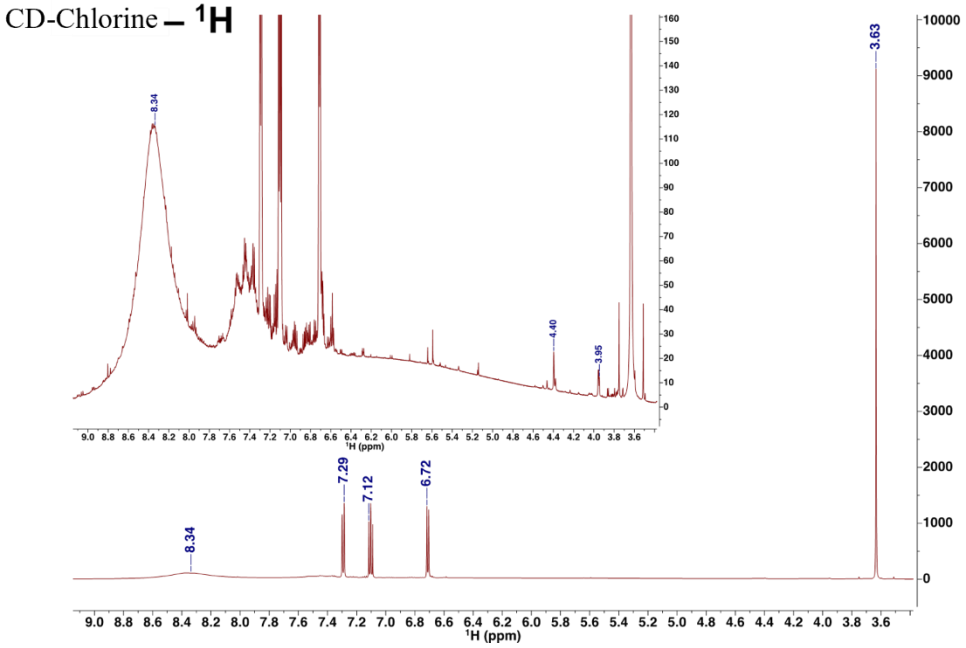

Figure 3.5: the figure shows the ^{1}H NMR of CD-Chlorine; the inset represents the magnification in the range 3.5-9.5 ppm.

The appearance of two very broad bands (4 - 10 ppm and 7-9 ppm), in the 1D proton spectra of CD-Chlorine supports the hypothesis that the sample is composed of long chains of macromolecular aggregates of hydrocarbons, which cannot be resolved by liquid-state NMR, due to slow reorienting motions with respect to the magnetic

field. DAN proton and carbon signals are conserved in CD-Chlorine, but downfield shifted in comparison to the free form, especially those closer to the amide groups (^{1}H/ ^{13}C signals at 6.7/109 ppm and 7.28/111 ppm).

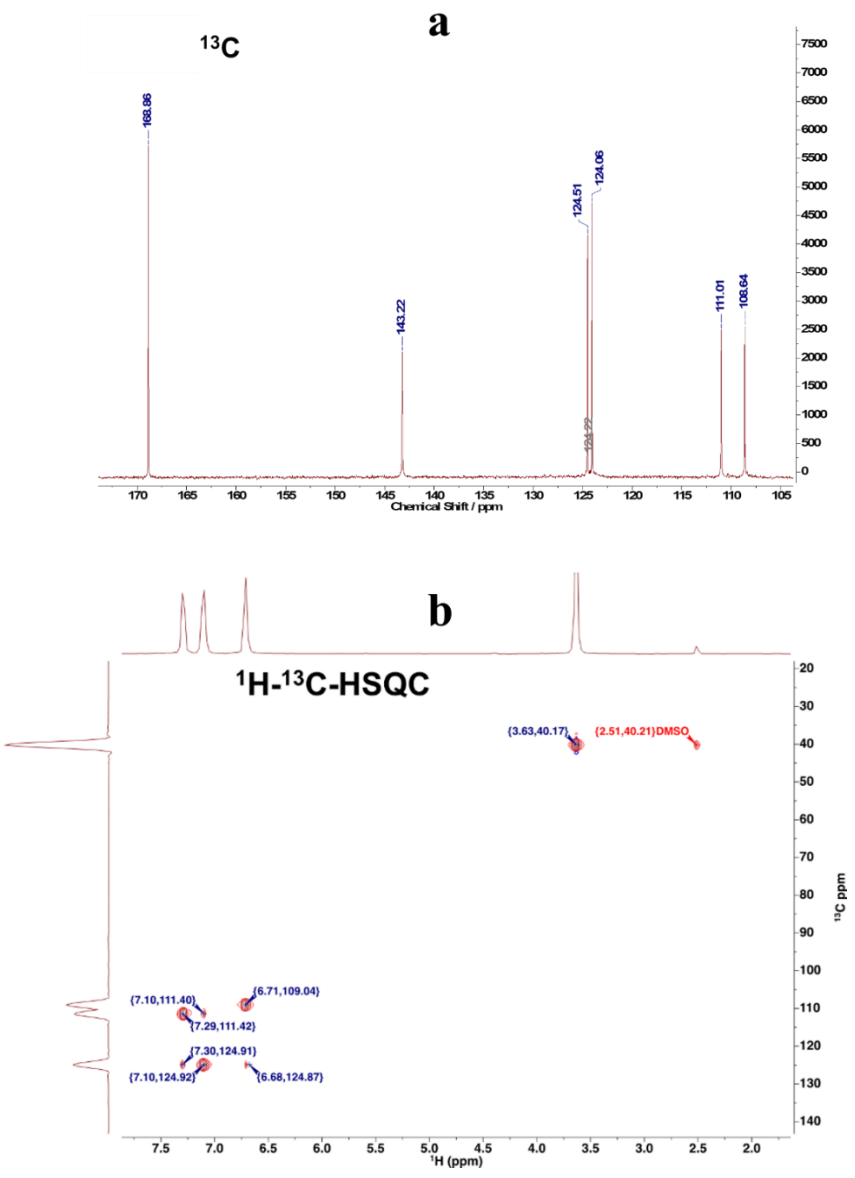

Figure 3.6 The figure shows a) ^{13}C analysis of CD-Chlorine and b) HSQC correlation between ^{1}H and ^{13}C-NMR.

NMR analysis of CD-Boron leads to different considerations. Signals from free Gly can be detected both in the 1D proton spectrum (3.01 ppm) (**Figure 3.7 a**) and the correlation of this signal with ^{13}C resonances (HSQC at 41.9 ppm; HMBC at 168 ppm (**Figure 3.7 b and c**, respectively)).

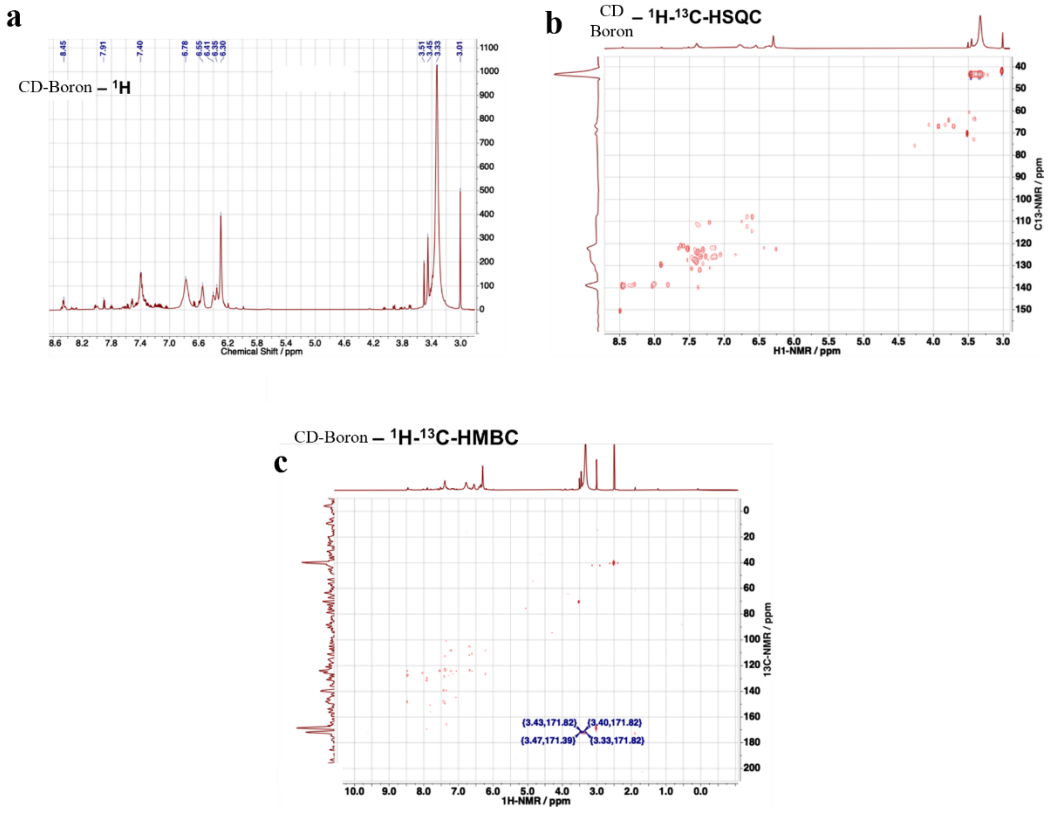

Figure 3.7: The image shows analysis of CD-Boron: a) ^{1}H NMR; b) HSQC; c) HMBC.

A broad proton signal at 3.33 ppm is assigned to the -NH_2 group of free Gly [189], however this signal is superimposed with signals of the methylene protons of at least three forms of polyglycines, which can be detected as HSQC cross peaks at 43.53 ppm. The heteronuclear multiple bond correlation (HMBC) at 3.33 - 171 ppm is ascribed to long-range scalar coupling between amine protons and carbonyl carbons of Gly (**Figure 3.7 c**). According to a preliminary calculation of the integrals of these HSQC cross peaks, roughly 20% of the Gly in CD-Boron is not

polymerized. Although free glycine is reasonably buried inside the polymeric strands and maintained by non-covalent contacts, it retains some reorientational freedom. In CD-Boron, DAN does not appear to retain its structure, but instead reacts with Gly and itself to generate a complex plethora of molecular compounds, which are likely smaller in size than in CD-Chlorine. This is also confirmed by the absence of very broad resonances as those observed in CD-Chlorine.

XPS analysis of the comparison of the two dots is shown in **Figure 3.8**. C1s spectra of CD-Boron and CD-Chlorine (**Figure 3.8**) have been deconvoluted into four components corresponding to different carbon states and chemical bonds, namely C-C/C=C (284.9 eV), C-OH /C-N (286.3 eV), -C=O (287.8 eV), and -COOH (289.1 eV). Significant modulation is observed in CD-Chlorine compared to CD-Boron. In particular, a lower contribution of COOH, C=O functional groups is observed next to C-OH functional groups. This could be attributable to a more efficient consumption of Gly towards a lower degree of polymerization and a higher degree of carbonization. In **Figure 3.8 a**, there is a greater contribution of the band at 284.4 eV, which we have attributed to sp^2 C=C bonds, probably responsible for a more graphitic structure compatible with the higher-contrast core observed at TEM.

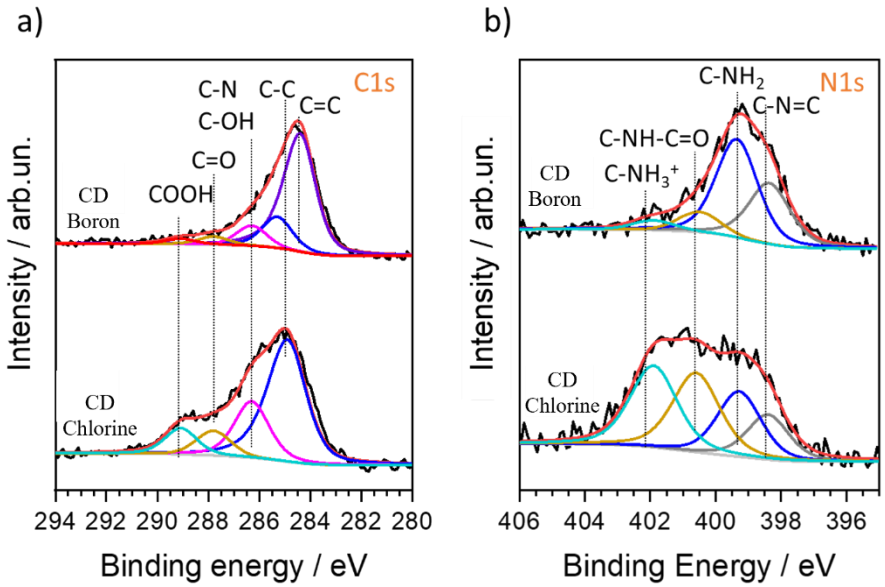

Figure 3.8 This figure shows the XPS measurement: a) C1s and b) N1s analysis.

However, a lower contribution of C-NH_3^+ and amide bonding is evident, confirming the formation of a compact and relatively less polymeric carbon structure than CD-Chlorine.

The evidence provided by XPS are in accordance with Raman measurements reported in **Figure 3.9**. The spectra are mainly characterized by the D and G bands at 1367 and 1590 cm^{-1} of a graphitic structure [190]. Due to the fluorescence over the scattering spectrum, it was not possible to acquire the Raman spectrum of the CD-Boron counterpart.

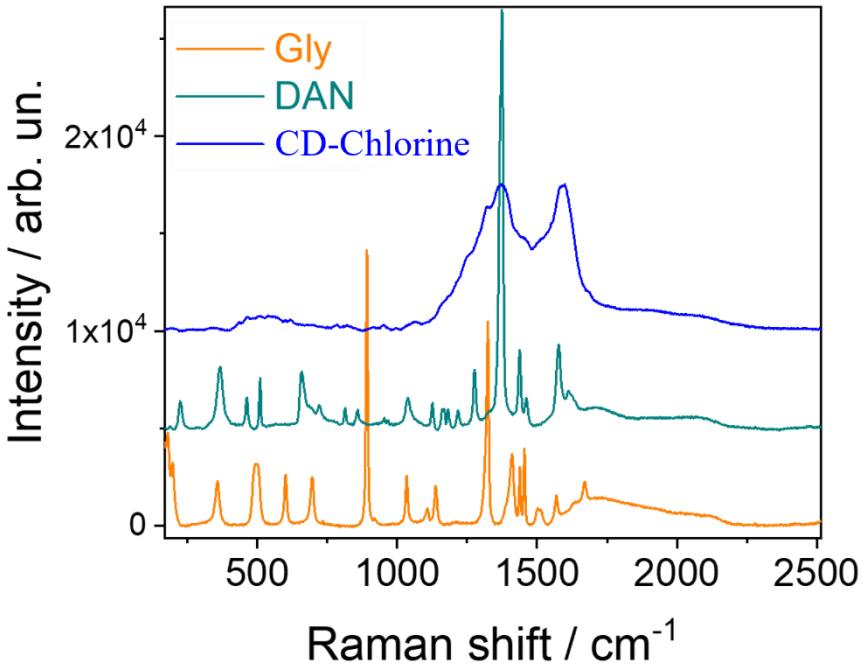

Figure 3.9 This is the Raman spectrum of CD-Chlorine compared to the one of Gly and 1,5-DAN.

Evaluation of the influence of 1,5-DAN concentration in CD-Boron:

To explore the potential provided by the synthesis of CD-Boron, three different compositions were evaluated (**Table 1**).

Table 1 Compositions of the CD-Boron with different concentrations of 1,5-DAN.

Sample	Glycine	1,5-diaminonaphthalene	Boric Acid
CD-Boron-01	1	0.1	1
CD-Boron-05	1	0.5	1
CD-Boron	1	1	1

Figure 3.10 shows the UV-Vis analysis of the samples at different concentrations. As it can be seen, an increase of the 1,5-DAN concentration leads to an increase in the intensity of the absorption at 330 nm. Anyway, the shape of the band, attributed to the $\pi \rightarrow \pi^*$ transition of the aromatic structure, is similar to the one of the 1,5-diaminonaphthalene [191]. At the highest concentration of 1,5-DAN we start observing an absorption at about 260 nm, probably due to a higher presence of carbonyl groups derived from the glycine [184].

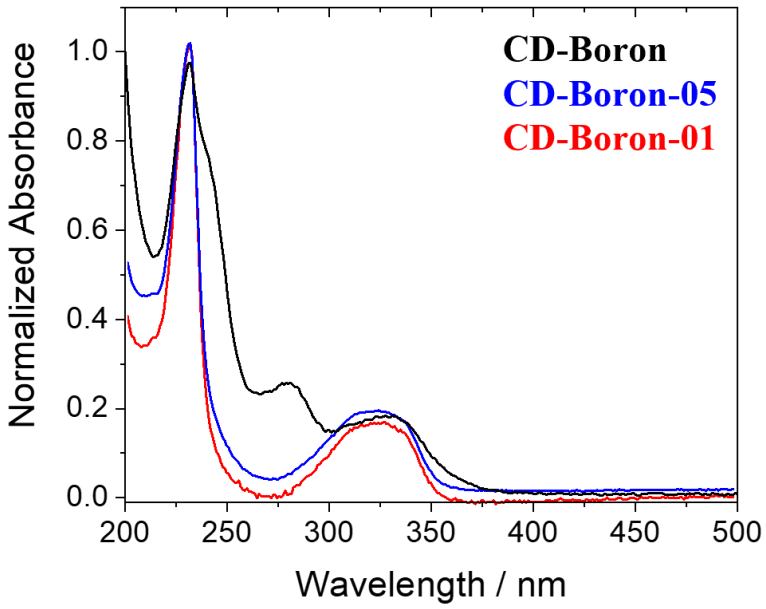

Figure 3.10 UV-Vis spectra of CD-Boron at different concentrations of 1,5-DAN.

The fluorescence analysis (**Figure 3.11**) of the same samples shows a strong emission at ~405 nm in each case, with a shift in the excitation wavelength from 350 to 320 nm as the concentration of 1,5-DAN increases.

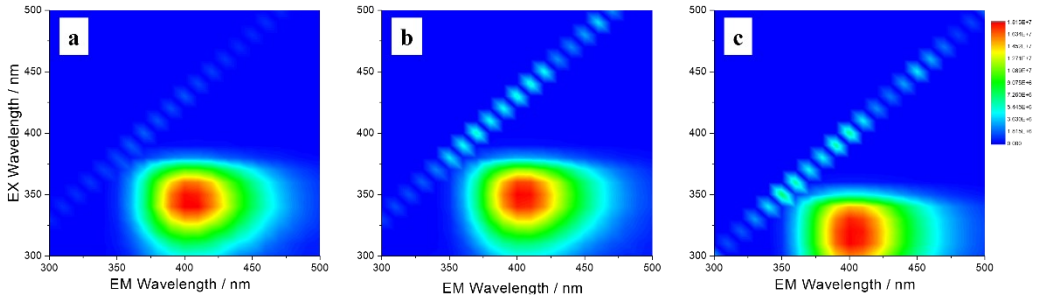

Figure 3.11 Fluorescence 3D maps of CD-Boron at different concentrations of 1,5-DAN in the range of excitation and emission of 300-500 nm.

FTIR-ATR spectra provide significant differences in the chemical structures of the three carbon-dots samples. In **Figure 3.12 a** is reported the ATR analysis at increasing molar ratios of 1,5-diaminonaphthalene with respect to the other two precursors. At a glance we observe a linear decrease of the amide I (about 1600 – 1700 cm^{-1}) band in accordance with the decrease of DAN concentration. A similar trend in intensity is also observed for the absorption bands attributed to the amide II and amide III (about 1400 and 1250 cm^{-1}, respectively) [184]. In addition, the patterns are very similar to that of glycine, except for the strong band at 1196 cm^{-1} that is given by the presence of unreacted aromatic amines [192].

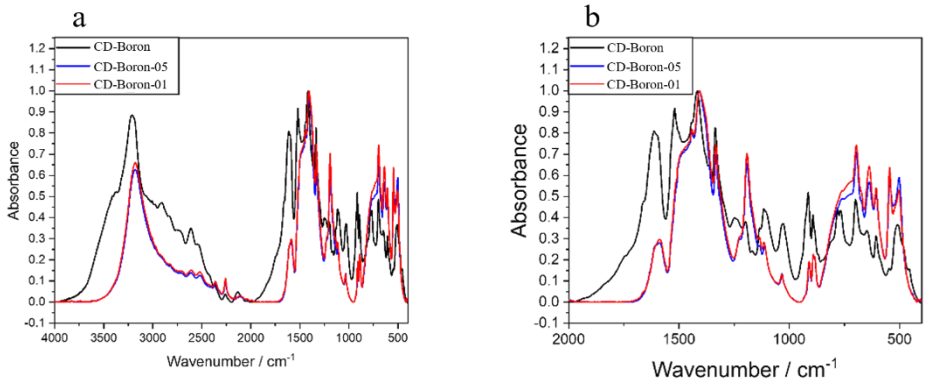

Figure 3.12 FTIR spectra of CD-Boron at different concentrations of 1,5-DAN in the range a) 4000-400 cm^{-1}; b) 2000-400 cm^{-1}.

Figure 3.13 shows the XPS spectra in the energy regions of carbon and nitrogen taken from the CD-Boron sample at different concentrations of 1.5-DAN. The signals related to carbon and nitrogen are the same as those observed previously. The C1s spectra of samples at different DAN concentrations do not appear to be particularly sensitive to different molar ratios, indicating that the spectra are more influenced by the presence of glycine and its intrinsic polymerization. The N1s spectra (**Figure 3.13 b**) provide further information about the glycine-DAN interaction. In this case, the spectra appear more sensitive to the molar ratio of the two precursors. CD-Boron is deconvoluted into four contributions, C-NH_3^+ (401.9 eV), C-NH-C=O (400.6 eV), C-NH_2 (399.3 eV) and C-N=C (398.4 eV) respectively. CD-Boron retains a significant contribution of glycine in its zwitterionic form in the solid state, and the formation of an amide bond is observed, which may be due either to the formation of polyglycine or to a chemical bond between glycine and DAN. The C-NH_2 contribution is made by the amines of DAN. Finally, we observe the formation of the C-N=C bond due to the presence of pyridinic N. By reducing the amount of DAN, its polymerization appears to be inhibited by the dispersion of DAN within the polyglycine matrix.

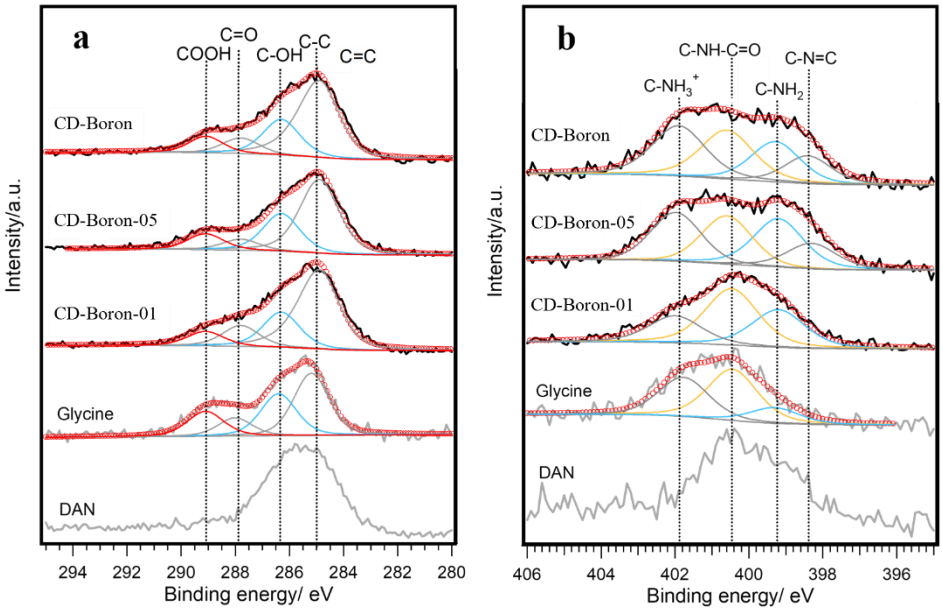

Figure 3.13 XPS comparison of a) C1s and b) N1s of CD-Boron at different concentrations of 1,5-DAN.

Finally, the structural differences between these two dots, were also observed in paramagnetic resonance measurements, to observe the eventual presence of radical species and the formation of singlet oxygen under visible light exposure.

Electron Paramagnetic Resonance for the detection of ROS:

Two types of Electron Paramagnetic Resonance (EPR) analysis were performed on the solid sample. In the first type, the sample was placed in a high vacuum ($P < 10^{-3}$ mbar) and kept in the dark or exposed to blue LED light (centered at 470 nm, irradiance of 344 W/m^2). Working in a vacuum is crucial to prevent the influence of molecular oxygen, which is a paramagnetic molecule itself, from altering the EPR signals of the material. The second type of analysis was conducted in the presence of oxygen to investigate its potential role in the observed photoinduced phenomena. **Figure 3.14** shows the EPR measurements of the CD-Boron **a)** in vacuum **b)** under oxygen pressure. The weak intensity spectrum is characterized by an isotropic signal at g = 2.004, attributed to carbon radical species (C•) [193]. The

figure also indicates minor signals with their respective g-values (g = 2.054, 2.030, and 1.978).

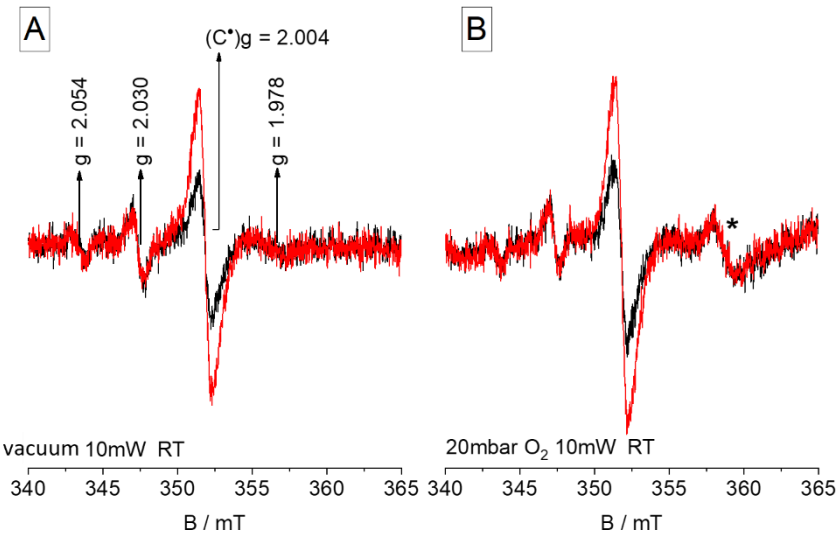

Figure 3.14 EPR measurement of carbon centers a) in vacuum and b) under oxygen pressure, of CD-Boron.

The carbon radical species display photosensitivity, as evident from the spectra recorded under irradiation with blue light, in vacuum conditions as well as in the presence of oxygen. After interrupting the irradiation, the original intensity is restored after approximately 60 minutes **Figure 3.15**. CD-Boron contains approximately 4.0×10^{14} spins/g of C• radicals.

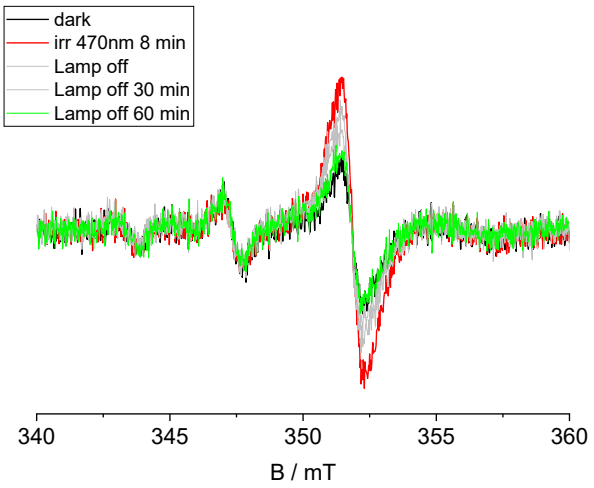

Figure 3.15 EPR measurement of carbon centers of CD-Boron under irradiation with a wavelength of 470 nm at different time of exposure.

In the case of CD-Chlorine (**Figure 3.16**), a single very intense and well-defined signal can be observed, always associated with the presence of carbon radical centers, with concentration 5.4 x 10^{17} spins/g, three orders of magnitude higher than in the CD-Boron sample. Also in this case, measurements were made in vacuum and in the presence of oxygen.

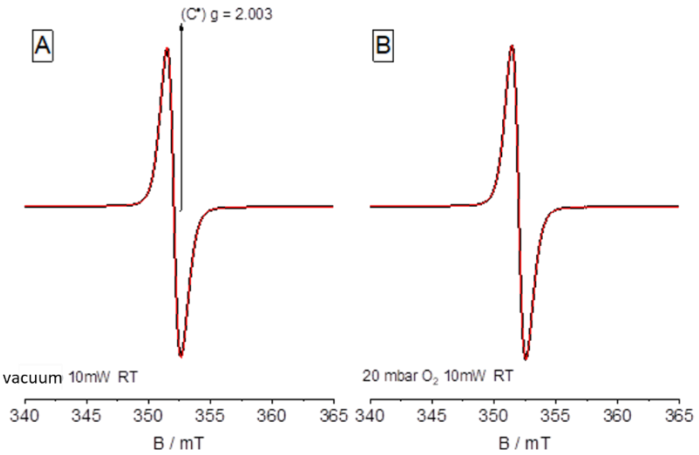

Figure 3.16 EPR measurement of carbon centers a) in vacuum and b) under oxygen pressure, of CD-Chlorine.

From these measurements, it is easy to assume that the structure of CD-Boron, in contrast to that of CD-Chlorine, has photosensitive sites that affect radical formation when under irradiation with visible light. The same behavior of CD-Chlorine was observed in the EPR spectrum of the 1,5-DAN precursor (**Figure 3.17**) with a concentration of carbon radical centers of 1.5 x 10^{15} spins/g.

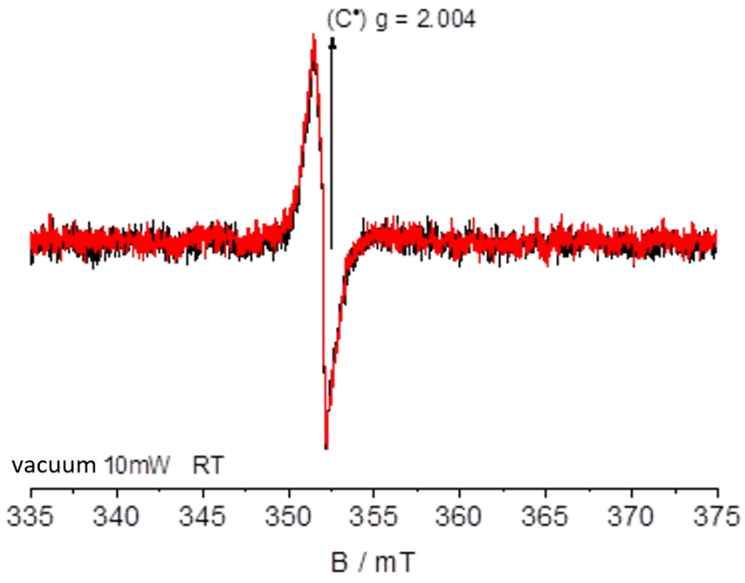

Figure 3.17 EPR measurement of carbon centers a) in vacuum and b) under oxygen pressure, of 1,5-DAN.

After the presence of carbon radical centers, the presence of other radical species, the reactive oxygen species, was also evaluated [194]. More specifically, the promotion of singlet oxygen, an excited (not radical) state of molecular oxygen, was evaluated.

In this case we utilized a pH 7.5 buffered solution (phosphate buffer) containing the CD-Boron sample (3 mg/ml) and 4-oxo-TEMP (0.044 M). Upon exposure to singlet oxygen, 4-oxo-TEMP reacts and forms the paramagnetic 4-oxo-TEMPO adduct

(**Figure 3.18**) [195]. During the test, the sample were exposed to blue light (470 nm), and EPR spectra recorded at 5, 30, and 60 minutes.

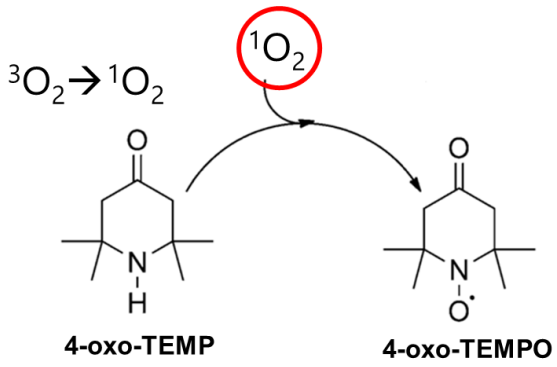

Figure 3.18 Scheme of the trapping of the singlet oxygen by the employing of the trapper TEMP.

To identify potential singlet oxygen species, the CDs suspension was irradiated under the conditions of 3 mg/ml, for the concentration, and a blue light at 470 nm, with a power of 344 W/m^2. Comparison of the two samples CD-Boron and CD-Chlorine, and the precursor 1,5-DAN (**Figure 3.19**), allowed for some very interesting observations. As can be seen, in contrast to the behavior shown previously with the formation of carbon radical centers, in this case only CD-Boron showed evidence of singlet oxygen formation.

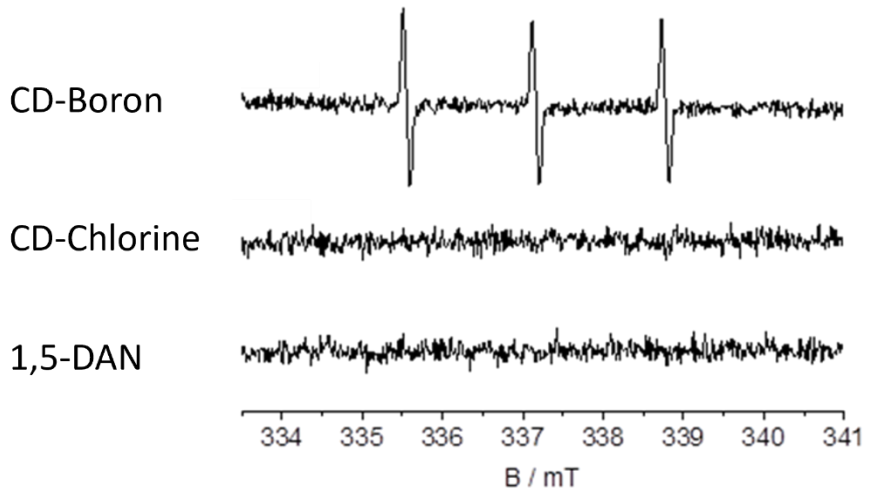

Figure 3.19 EPR measurement of singlet oxygen production of a) CD-Boron, b) CD-Chlorine, c) 1,5-DAN.

A more detailed view of this result shows that there is an increase in the intensity of the signal associated with singlet oxygen formation as the time of exposure of the sample to visible light (470 nm) increases (**Figure 3.20**).

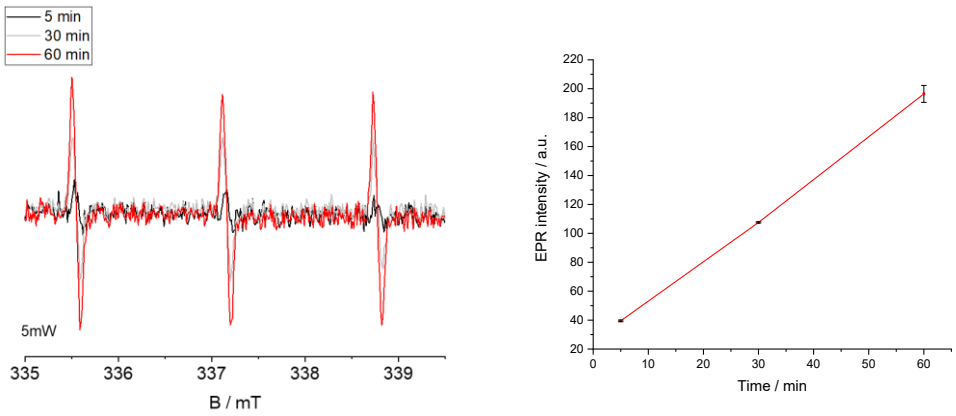

Figure 3.20 EPR measurement of singlet oxygen production of CD-Boron respect to the time of exposure at the visible light (470 nm).

The influence of the increasing amount of 1,5-DAN in the CD-Boron samples was also evaluated by EPR analysis. By halving the amount of 1,5-DAN in the synthesis step, a structure was obtained that exhibits almost the same signals as the carbon radical centers observed in CD-Boron (**Figure 3.20**), with a concentration of 1.4 x 10^{15} spins/g.

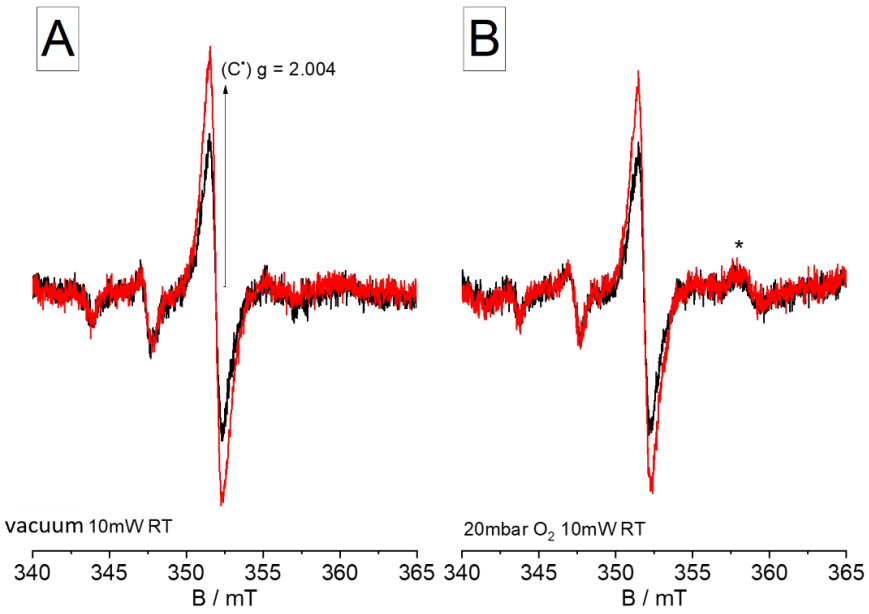

Figure 3.21 EPR measurement of carbon centers a) in vacuum and b) under oxygen pressure, of CD-Boron-05.

Again, photosensitivity can be observed in the presence of irradiation with visible light.

Concerning the measurements of the singlet oxygen production under visible light irradiation, a sensitive difference among CD-Boron and CD-Boron-05 (**Figure 3.22**) is observed.

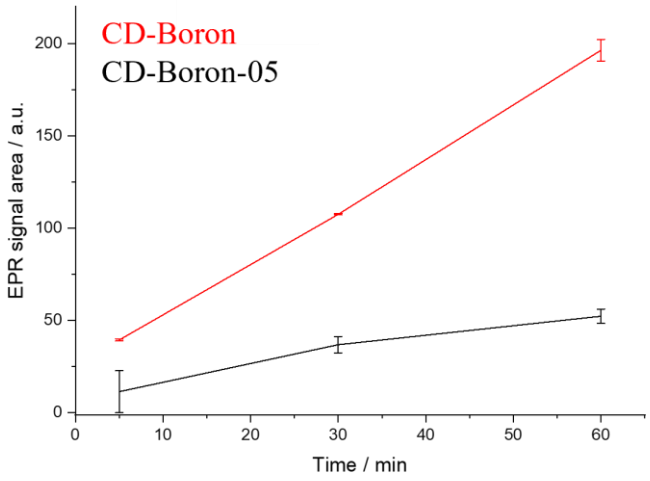

Figure 3.22 EPR measurement of singlet oxygen production of CD-Boron (red line) and CD-Boron-05 (black line).

In this case, by halving the amount of 1,5-DAN in the synthesis step, the structure that is obtained is less performing than that of CD-Boron, due to the lower amount of poly-1,5-DAN graphitic structure.

Hydrothermal CDs

The hydrothermal CDs were not analyzed as in detail as those synthesized by microwaves due to a lack of time and availability of the equipment. Nevertheless, in this paragraph, we the preliminary characterizations of this system, obtained from glycine, glycyrrhizic acid and boric acid, called CD-Lico.

Figure 3.23 shows the UV-Vis spectra of the CD-Lico. The spectrum shows four absorption signals: the first two, the one at approximately 210 nm and the one at about 250 nm, are associated with the absorption bands of glycine and glycyrrhizic acid, respectively, while the one at approximately 260 nm and about 330 nm are associated with the formation of aromatic structures [196]. Although not very clear, there is also an absorption component peaked at around 360 nm and attributed to the presence of aromatic structures.

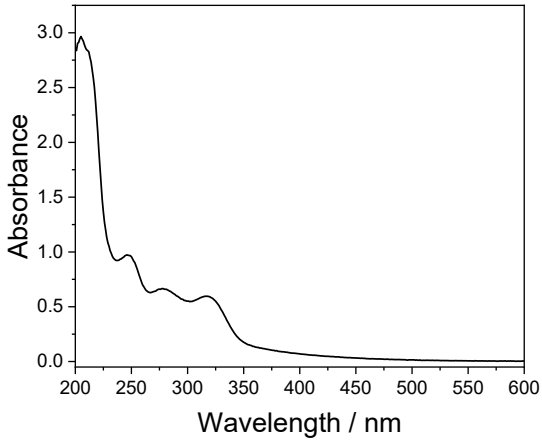

Figure 3.23 UV-Visible spectra of CD-Lico in the range of 200-600 nm.

Figure 3.24 shows the emission signal of the CD-Lico sample. The maximum of emission is centered at around 445 nm when the sample is irradiated with a wavelength of about 360 nm. This result is consistent with that one observed in the UV-Visible analysis.

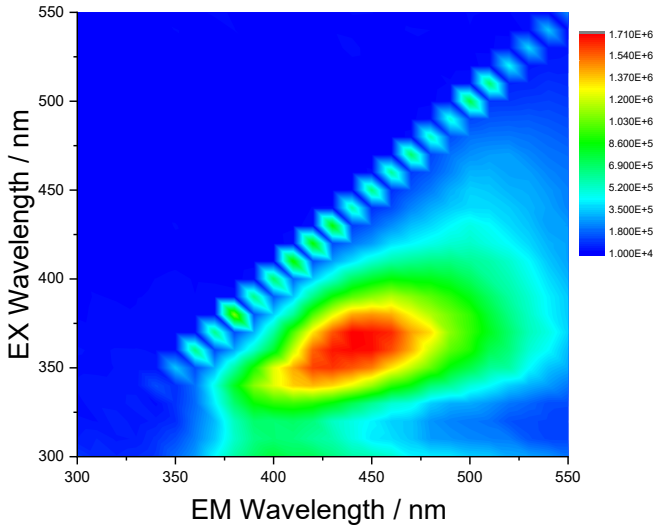

Figure 3.24 3D map of the fluorescence of CD-Lico in the range of excitation and emission 300-500 nm.

The FTIR analysis (**Figure 3.25**) shows some interesting signals. The presence of different vibrational modes assigned to NH_2 (1576 cm^{-1}, bending; 1500 cm^{-1}, symmetric bending + rocking; 1429 cm^{-1}, NH_2 bending; 1329 cm^{-1}, C-H_2 bending + NH bending) and CH_2 (1443 cm^{-1}, deformation) are typical of glycine [184]. The presence of a band at approximately 1700 cm^{-1} is associated with the COOH groups, which are abundantly present in glycyrrhizic acid [197]. The bands in the range between 1300-1400 cm^{-1} are of particular interest as they contain the contribution related to the amide bonds of tertiary amides; the CD-Lico shows an increase in intensity of these vibrational modes with respect to its precursors. The increase is consistent with the amidation reactions that likely occur between the amino group of glycine and the carboxylic groups of glycyrrhizic acid.

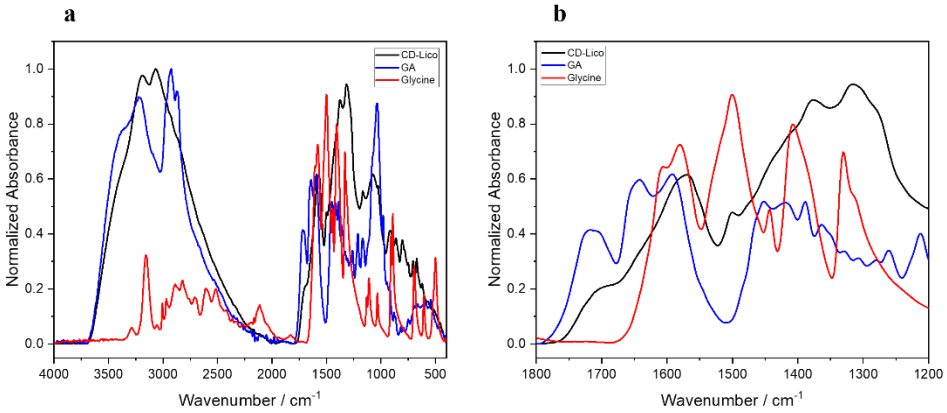

Figure 3.25 The figure shows the FTIR spectra of CD-Lico (black line), glycyrrhizic acid (blue line) and glycine (red line) in the range a) 4000-400 cm^{-1} and b) 1800-1200 cm^{-1}.

TEM characterization reveals (**Figure 3.26**) that the CD-Lico are made by large particles with a dense, almost spherical core surrounded by a less dens corona. As previously observed in the CD-Chlorine sample, this type of morphology suggests the presence of a compact inner part, which can be also composed of unreacted monomers, along with the presence of long polymer chains. Considering the

uniform shape of the particles, however, it is possible also hypothesize the presence of graphitic cores, as seen in the case of CD-Boron, which is highly probable due to the presence of glycyrrhizic acid (composed of aromatic rings). The shadow around the dense core can be associated with the formation of glycine polymers, which are formed during hydrothermal reactions catalyzed by boric acid, and glycyrrhizic acid polymers.

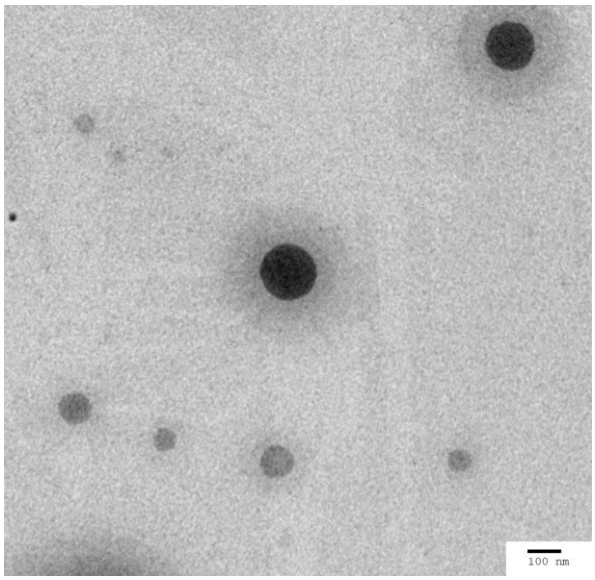

Figure 3.26 The figure shows the TEM image of CD-Lico, with a bar scale of 100 nm.

The surfaces

To achieve the surface engineering two approaches were used: the former uses an organosilane-based film for anchoring the nanoparticles through covalent chemical bonds, while the latter makes use of a polymer matrix to incorporate the dots to form flexible and self-standing surface.

For CD-Boron was used for the functionalization of organosilane films because of the good dispersibility in organic solvents while CD-Lico was embedded the polymer matrix, because of its better dispersion in water.

The nanoparticles (CD-Boron) were anchored to the film composed of a double layer of TEOS and APTES through an EDC/NHS coupling reaction. The coupling reagent EDC first activated the carboxylic group of the carbon dots, and it was subsequently replaced by NHS. NHS allows the formation of an ester adduct, which serves as an excellent leaving group [198], facilitating the reaction between the carboxylic group of the dot and the amino group provided by the APTES in the film. A typical image of the carbon dots-functionalized surface is shown in **Figure 3.27**. The optical appearance of the films does not change after carbon-dots functionalization suggesting the formation of a very thin layer of nanoparticles, with a small amount of aggregates.

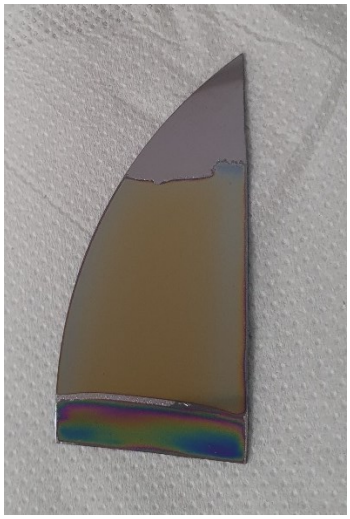

Figure 3.27 Picture of the functionalized silicon substrate with CD-Boron.

Atomic force microscopy was used to characterize the substrate morphology after carbon-dot functionalization. **Figure 3.28 a** is the image of the silicon wafer surface with the organosilica layer but without the carbon-dots. At this stage, the surface was treated only with the EDC/NHS reagents to observe possible differences after functionalization. As can be seen, the surface appears homogeneous, with a repeated structure throughout, represented by protrusions that look like a mountain

chain. The image in Figure 3.28 b is the confirmation of successful functionalization. As can be observed, the morphology completely changes and shows individual peaks, likely due to dots aggregates and associated to the anchoring of the carbon dots to the surface. It is important to note that the dots remain on the surface after several washing step and even a sonication treatment, indicating that the chemical functionalization is strong enough to provide a reasonable mechanical stability.

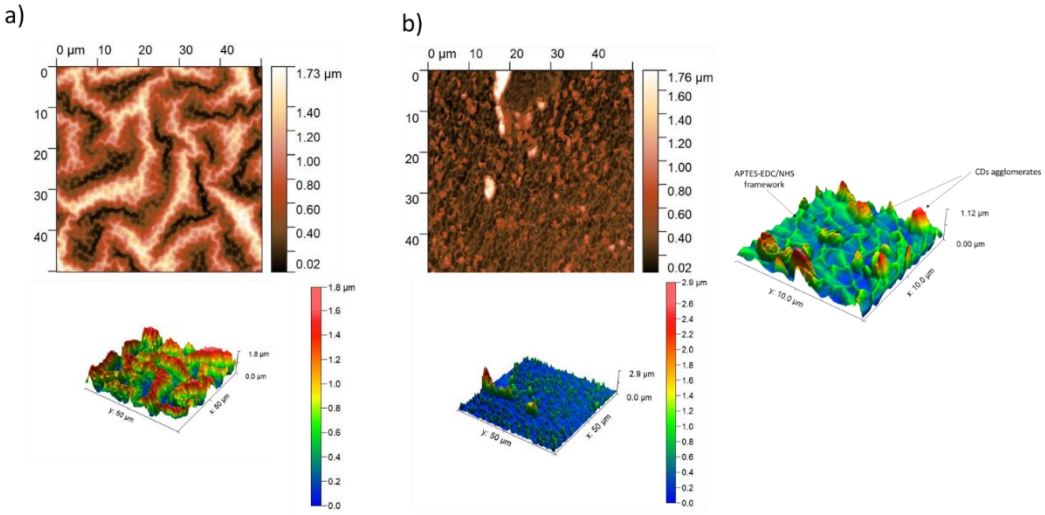

Figure 3.28: a) AFM images of pristine APTES-EDC/NHS functionalized and b) CD-Boron coated surfaces.

The second type of antiviral surface was obtained by forming a nancomposite layer of polyvinylalcohol (PVA) bearing carbon dots nanoparticles. The carbon dots (CD-Lico) were at first dispersed in an aqueous solution containing PVA and glycerol, then, once a homogeneous dispersion was obtained, it was deposited in a Petri dish. A subsequent heating treatment in an oven at 60°C overnight led to the formation of a self-standing surface (**Figure 3.29**). The addition of glycerol allowed the production of a more flexible film.

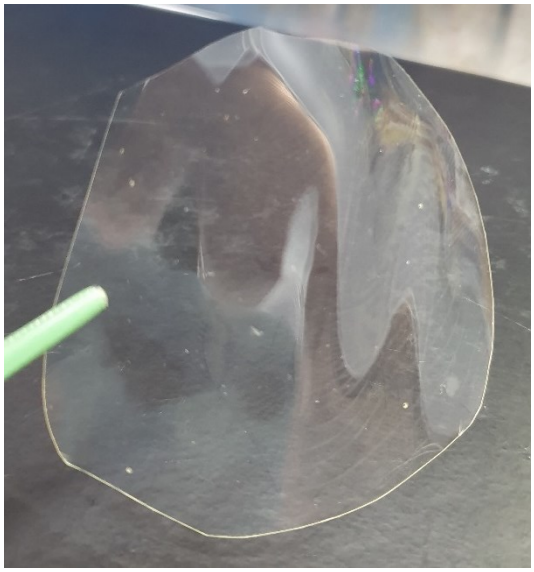

Figure 3.29 Picture of the self-standing surface functionalized with CD-Lico.

The successful functionalization was confirmed by measuring the fluorescence of the obtained film, which was found to be the same as that of the CD-Lico initially used (**Figure 3.30**).

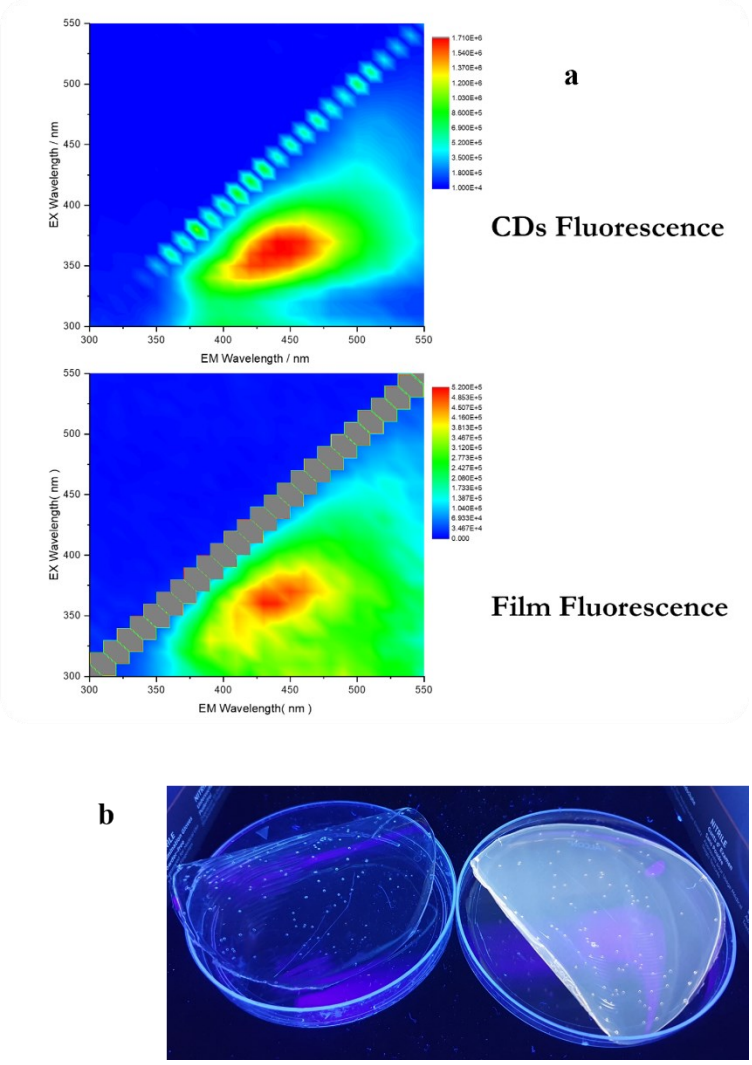

Figure 3.30 The figure shows a) the fluorescence of CD-Lico (upper picture) and fluorescence of the functionalized surface (lower picture); b) picture of both surfaces under a UV lamp: left non-functionalized and right functionalized with CD-Lico.

Antimicrobial evaluation

Antiviral evaluation:

Before testing the antiviral surfaces, the virucidal activity of the different carbon-dots, were evaluated against SARS-CoV-2, alone or in combination with visible or

ultraviolet light exposure, according to guidelines reported in EN14476 for testing of chemical disinfectants.

The analysis was conducted on original Wuhan strain and Delta strain of SARS-CoV-2 (Human 2019-nCoV strain INMI1, from Istituto "L. Spallanzani", Rome, Italy).

CD-Boron and CD-Chlorine cytotoxicity and virucidal activity were assessed in Vero E6 cells (African Green Monkey (Cercopithecus aethiops), ATCC-CRL-1586). Treatment concentration for each nanomaterial was selected in order to get a non-cytotoxic concentration at the first serial dilution added to cells during viral titer determination experiments. After 24 hours in a 96-well plate, Vero E6 cells were exposed to various concentrations of CDs for 72 hours. The biocompatibility was evaluated by observing the integrity of the cell monolayer under microscope. Correspondingly, we have estimated the cytotoxic concentration 50% (CC50) for each sample.

Results are reported in **Table 1**. Cytotoxicity was investigated at the increasing concentrations of 0.05, 0.50 and 5.00 mg ml^{-1}. CC50 of 2.5 mg ml^{-1} was determined for both CD-Boron and CD-Chlorine.

Table 1. Analysis of CD-Boron and CD-Chlorine cytotoxicity. Effect of nanomaterials on cell monolayer integrity.

	Cell monolayer integrity (viability)		
Tested Material	**5.0 mg ml^{-1}**	**0.5 mg ml^{-1}**	**0.05 mg ml^{-1}**
CD-Boron	0	100	100
CD-Chlorine	0	100	100

Under non-cytotoxic conditions, CD-Boron and CD-Chlorine virucidal effect against original strain (Wuhan) of SARS-CoV-2 were tested in dark and under light

exposure conditions, namely at 365 nm (UV) and 450 nm (Vis), as in the photograph in **Table 2 e**.

Table 2. a) Virucidal effect of CD-Boron and CD-Chlorine under ultraviolet light (UV ; λ = 365 nm) exposure. b) Virucidal effect of CD-Boron and CD-Chlorine under visible light (Vis ; λ = 450 nm) exposure.

a)

Tested Material	**Viral titer ($TCID_{50}$/ml)**
Control	2.85×10^5
Control – UV on	3.16×10^5
CD-Boron	7.50×10^4
CD-Boron – UV on	$0.00 (< 3.16 \times 10^2)$
CD-Chlorine	2.31×10^5
CD-Chlorine – UV on	$0.00 (< 3.16 \times 10^2)$

b)

Tested Material	**Viral titer ($TCID_{50}$/ml)**
Control	3.16×10^5
Control – Vis on	1.78×10^5
CD-Boron	1.78×10^6
CD-Boron – Vis on	1.00×10^4
CD-Chlorine	3.16×10^5
CD-Chlorine – Vis on	1.43×10^5

In a typical experiment, 10 µl of CDs (at the concentration of 3.3 mg ml^{-1}) have been added to 5 µl of viral suspension. The wells have been irradiated for 5 minutes followed by other 5 minutes of incubation. Firstly, we observe that under exposure of light (both UV and Vis) for 5 min, the viral titer appears substantially unaffected, with TCID50 / ml > 3.9×10^5. Furthermore, the addition of CDs does not affect the viral titer under dark conditions. Under exposure to UV light, both CD-Boron and CD-Chlorine determine an effective virucidal effect promoting the reduction of the viral titer to negligible values. On the contrary, the exposure to blue light produces different effects according to the specific CD.

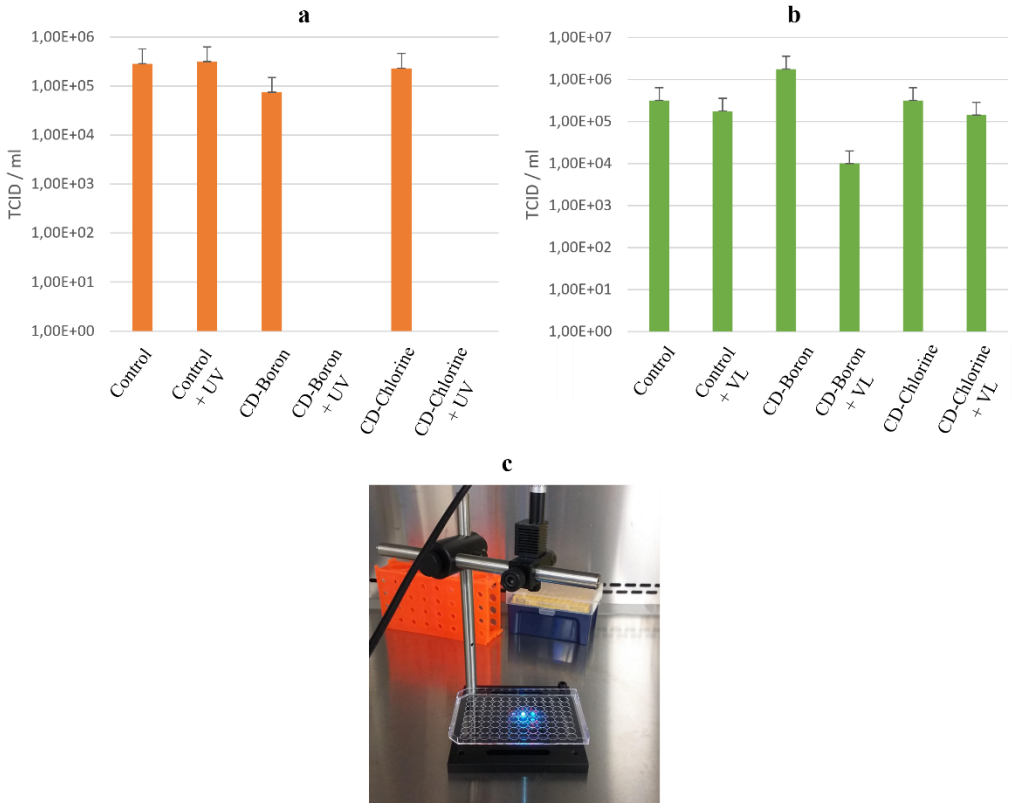

Figure 3.31 Bar chart of viral titer under (a) UV and (b) visible exposure conditions. c) Photograph of the experimental setup.

CD-Chlorine does not cause a significant decrease of viral titer with a small modulation comparable with the control. CD-Boron instead provokes a reduction of the titer of more two orders of magnitude. Based on in vitro experiments, it appears that CDs are able to produce a virucidal effect if triggered by UV light producing a more effective antimicrobial effect with respect to mere light. One species of carbon-dots, namely CD-Boron, also supports the antiviral effect under visible light. On the contrary, CD-Chlorine results ineffective at the same conditions. This result is consistent with what was observed in the EPR analysis. Among the two types of dots, only CD-Boron exhibits photosensitivity under visible light irradiation and is therefore the only one that promotes the formation of reactive oxygen species under these conditions.

The same tests were conducted on the functionalized surface (**Figure 3.32**).

In this case, tests were carried out on both variants of SARS-CoV-2, the original strain, and the Delta variant, obtaining interesting results.

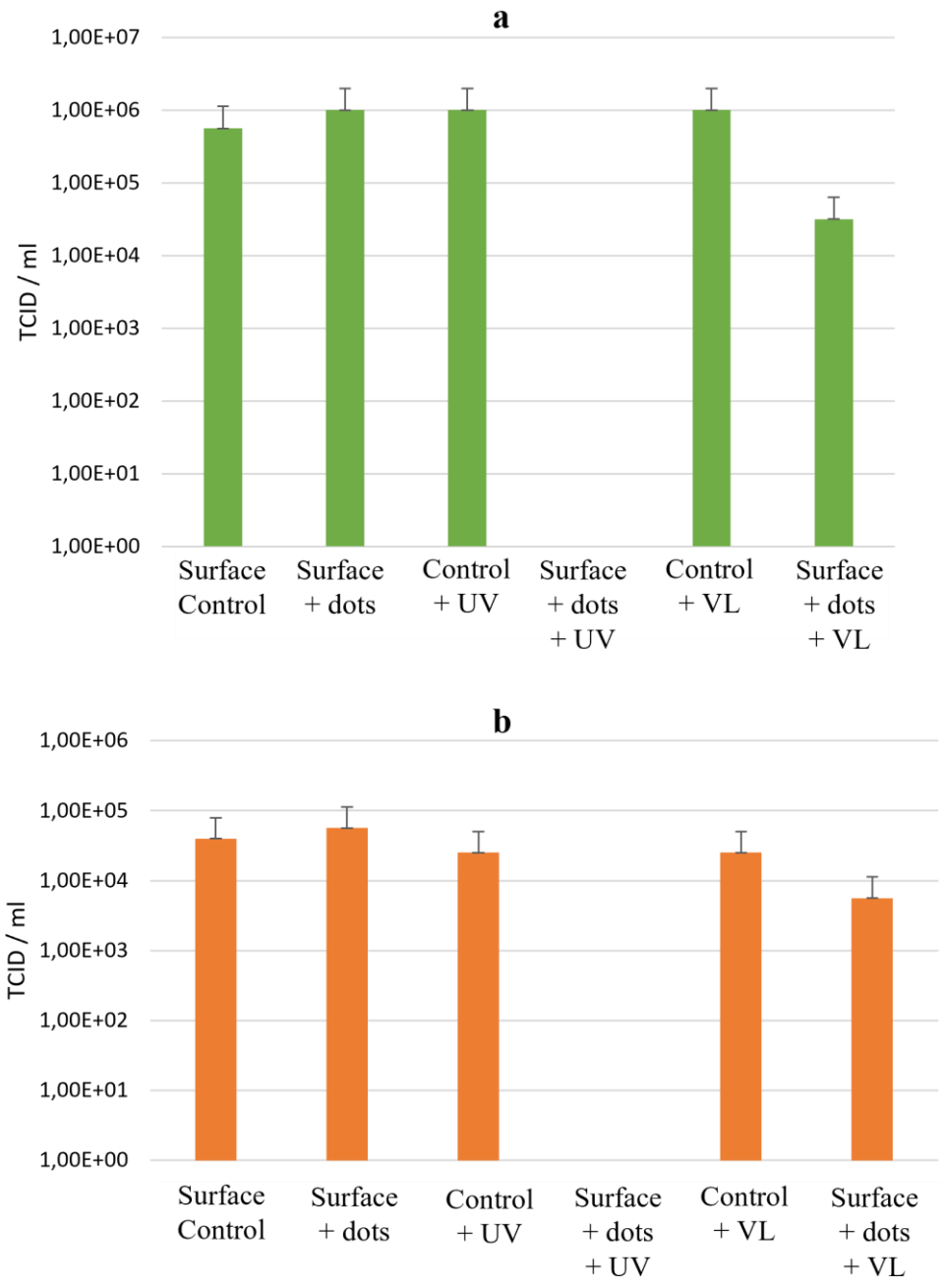

Figure 3.32 Bar chart of viral titer under UV and Visible (VL) light: a) against original strain and b) against delta strain of SARS-CoV-2, of the functionalized surface with CD-Boron.

The dots used for surface functionalization, kept their antiviral properties even after the functionalization. Specifically, the performance was the same for both variants under UV and visible irradiation.

Antibacterial evaluation

The second type of functional surface, on the other hand, was tested against bacterial resistance. CD-Lico were tested against four bacteria: two gram-positive, two gram-negative. As can be seen from the tests performed according to Broth's microdilution method [199], CD-Lico showed interesting bacterial susceptibility to gram-positive bacteria S. aureus and E. faecium (**Figure 3.33**).

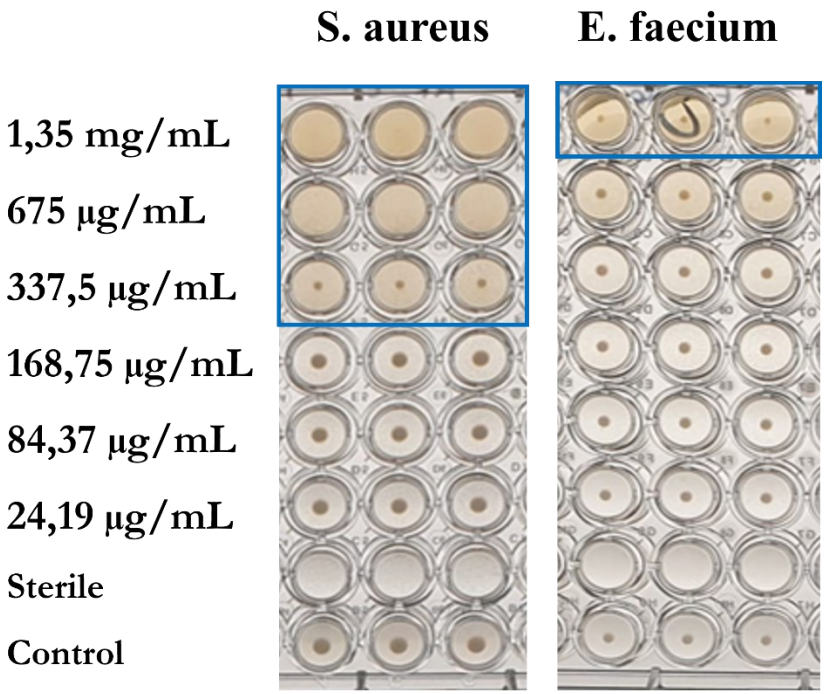

Figure 3.33 Antibacterial test of CD-Lico against gram positive bacteria.

The dots, against gram-negative bacteria P. aeruginosa and A. baumannii, were not effective (**Figure 3.34**). This result probably depends on the different structure of the bacteria. Gram-negative bacteria, contrary to gram-positive bacteria, have three outer membranes, as opposed to two membranes in gram-positive bacteria. These

three membranes prevent more efficiently, the passage of the dots inside the cell, where they would go for biological activity.

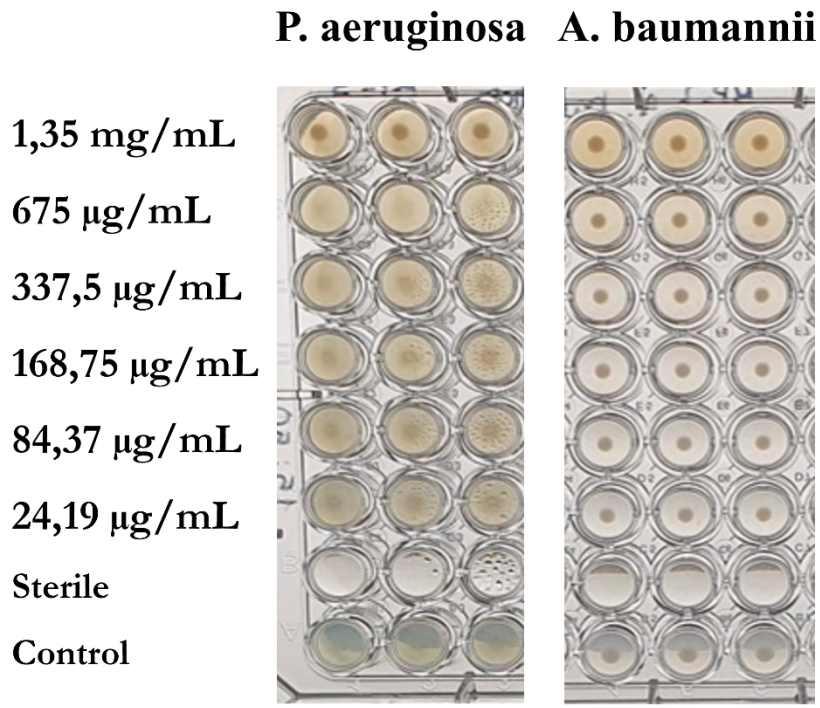

Figure 3.34 Antibacterial test of CD-Lico against gram negative bacteria.

Self-standing surfaces developed using CD-Lico, have proven to be of particular interest in food packaging (**Figure 3.35**). In a proof-of-concept demonstrator, the CD-Lico film was used as a top coating for boxes of fresh food, such as fruit, to provide a better preservation of the product. A sample of strawberries was used to evaluate the effective antimicrobial action of the surfaces. All tests were carried out at room temperature, in the air, with a humidity of about 60%, in dark conditions.

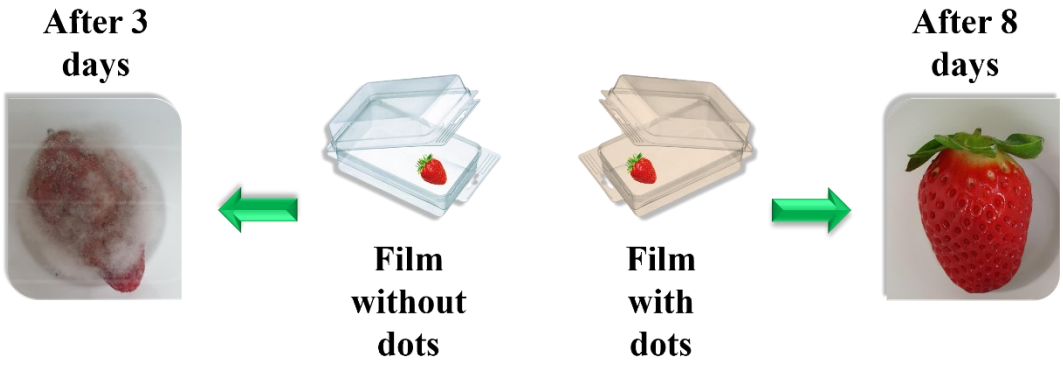

Figure 3.35 Proof of concept of the self-standing surface, functionalized with CD-Lico, in the field of food packaging.

As can be seen from the results obtained, CD-Lico was able to inhibit mold (botrytis cinerea) formation for at least 8 days, compared with 3 days for the strawberry covered with the non-functionalized film. Although preliminary, these results appear of extreme interested in the prospected applications. Further experiments are ongoing to elucidate the mechanism of antibacterial activity even is the surface is not put in direct contact with the food.

Chapter 4: Conclusions

This doctoral project was aimed at developing functional surfaces with antimicrobial properties, exploiting the properties of carbon-dots. To do this, two different systems were designed, one with 1,5-diaminonaphthalene and one with glycyrrhizic acid, that had as a common precursor an amino acid, the glycine. In both carbon-dots, the aim was to exploit the amino and carboxyl groups of glycine in order to form carbonaceous structures based on the amide bonds. Dots synthesized from glycine and 1,5-diaminonaphthalene were comprehensively characterized, evaluating the variation in the molar ratios of the precursors and also assessing the importance of an acid catalyst such as boric acid (CD-Boron) and hydrochloric acid (CD-Chlorine).

Comparison between CD-Boron and CD-Chlorine:

In the comparison of the two carbon-dots, CD-Boron and CD-Chlorine, many differences were observed, both from a structural perspective and from an antiviral activity point of view.

First, several UV-Visible absorption signals were observed, with maxima centered at 330 nm for CD-Boron and 360 nm for CD-Chlorine. These absorptions led to two different signals of fluorescence (property present in both dots) emission, at 405 and 450 nm, respectively.

The structural composition is characterized by different signals observed at TEM, FTIR, NMR and XPS, associated with significantly different structures between the two dots. TEM images showed two different morphologies: for CD-Boron, nanoparticles were observed, with a size around 18 nm, with a dense core (associated with the compacted state of long polydiaminonaphthalene chains that enclose monomeric glycine units within them), well defined and with a rather homogeneous particle size distribution. For CD-Chlorine, on the other hand, particles were observed with a dense core of very small size, about 2 nm, associated with the compaction of small structures formed by short polyglycine chains that reacted with single molecules of 1,5-diaminonaphthalene, with a second polymer-

type structure around it, bigger than the dense one, associated with the presence of long polyglycine chains. From the TEM images, therefore, it can be seen that the use of boric acid leads to the formation of more compact structures, probably due to more efficient polymerization of the precursors, particularly of 1,5-DAN, which itself has aromatic rings and more easily promotes the formation of graphitic-type structures. On the other hand, hydrochloric acid (in CD-Chlorine) promotes more the reaction between the two precursors, also going to form small particles formed by a few units of glycine and one of 1,5-DAN, as well as promoting the polymerization of glycine alone. This result, hypothesized mainly on the results obtained from FTIR, NMR, and XPS measurements, may suggest that hydrochloric acid is more efficient than boric acid in this reaction.

When performing EPR analysis, several considerations can be made.

The EPR measurement has shown the presence of carbon radical centers in both samples, CD-Boron and CD-Chlorine, with a higher concentration in the one synthesized with hydrochloric acid. The analysis conducted on the precursor 1,5-diaminonaphthalene alone has also revealed the presence of carbon radical centers. This indicates that carbon radicals are an intrinsic property of this precursor and, consequently, its derivatives. The CD-Chlorine sample and the 1,5-DAN precursor exhibit the same behavior under visible light irradiation (470 nm), with the carbon radical signals consistently present. In contrast, CD-Boron shows different properties when irradiated with a light with the same wavelength.

In this case, an increase in the concentration of carbon radical centers was observed, which varies with the extended exposure time of the sample. This is attributed to the presence of a weak signal resulting from the absorption of electromagnetic radiation at around 460 nm for this sample. The presence of this maximum at this specific wavelength is due to the graphitic-like structure promoted during the reaction catalyzed by boric acid. This structure makes CD-Boron photosensitive.

In addition to the carbon radical centers, the promotion of reactive oxygen species, specifically singlet oxygen (whose importance has been discussed in chapter 1), has also been evaluated.

To carry out this measurement, a "trapper" molecule was used, which is called 4-oxo-TEMP. When this trapper is in the presence of singlet oxygen, it can capture it and make it detectable by EPR.

The measurement conducted on the 1,5-DAN precursor did not show any promotion of singlet oxygen, neither under visible light irradiation at 470 nm. CD-Chlorine exhibited the same behavior as the precursor alone, not promoting singlet oxygen formation in any case.

For CD-Boron, on the other hand, there was observed a promotion of singlet oxygen, and this promotion increased in concentration with prolonged exposure of the sample to visible light. This result indicates that the 1,5-DAN precursor is not responsible for the photoactivity of this dot and that the nanoparticle structure promoted by boric acid is better than that promoted by hydrochloric acid, even though hydrochloric acid more effectively promotes the reaction between the reagents, regarding the formation of this ROS.

The promotion of ROS is the main mechanism hypothesized for the antimicrobial activity of these nanomaterials.

From the measurements conducted on the original variant of SARS-CoV-2, it is evident that CD-Boron and CD-Chlorine are equally effective when irradiated with ultraviolet light (365 nm). This is probably because they both produce singlet oxygen under irradiation at this specific wavelength. This is possible because both dots have absorption maximum in this region of the spectrum. However, when we shift to the visible spectrum, CD-Chlorine no longer exhibits efficient antiviral activity, as it did in the previous case, but instead appears almost ineffective. In contrast, CD-Boron, although less than the measurement under UV light, is still effective even in the visible range. This is because, as mentioned previously, graphitic structures are present that allow absorption of light at about 460 nm, making it photoactive even under these conditions.

The same results were obtained with another variant of SARS-CoV-2, the delta variant, where CD-Boron showed approximately the same efficacy.

The CD-Lico:

Regarding CD-Lico, composed of glycine, glycyrrhizic acid, and boric acid, even with limited characterizations, we can still make some observations. From the TEM images, a double structure similar to that shown by CD-Chlorine can be observed. However, in this case, the dense cores are of discrete dimensions, and the polymeric halo has a smaller size. Overall, the particles exhibit an almost spherical shape, typical of carbon dots, but with a size on the order of 100 nm. The presence of polymers in this sample is expected, as it is reported in the literature that both, glycine and glycyrrhizic acid, can form long polymeric chains under specific reaction conditions.

However, from the FTIR measurements we can assume that large amounts of unreacted monomers are present here as well. Probably, as in the case of CD-Boron, these compose the dense core observed at TEM.

Although limited structural characterizations, biological analyses returned some interesting results: the CD-Lico dots showed attractive anitbacterial susceptibility against gram-positive bacteria. The ineffectiveness of these dots against gram-negative bacteria is probably due to the difficult penetration of the nanoparticles inside the cell because of the thick membrane they possess.

The surfaces:

Surface engineering was studied using two approaches: one approach involved the deposition of an organosilane-based film on a single-crystalline silicon substrate and then functionalizing this film with the dots through an EDC/NHS coupling reaction; a second approach, on the other hand, involved the use of a polymer matrix where the dots are incorporated internally (functionalization), to obtain a self-standing surface.

In the first approach, CD-Boron were used for functionalization, as it is necessary to effectively disperse the dots in an organic solvent (N,N-dimethylformamide) to create the right reaction environment. In this case, the use of a double layer of organosilanes, was designed to improve the adhesive properties of the film to the substrate, a recurring problem in this type of system. What we got was a film that

could withstand the fingerprint test and rinsing with water and ethanol. However, it presents less resistance from a scratching perspective.
The surface functionalization was confirmed by AFM measurements.
The antiviral activity of the surface so functionalized has been tested against two variants of SARS-CoV-2, the original strain and the delta strain. It was observed that the dots kept their antiviral property even after functionalization, and in both cases, they remained effective under both ultraviolet and visible light irradiation.
Functionalization through a coupling reaction works and is appealing for surfaces that can be pre-modified with sol-gel, including methods such as spray coating.
For the second approach, CD-Lico was used for the functionalization of the self-standing surface. This choice was made due to its better dispersion in water, which is the solvent used for the building of this system. In this case, the surface functionalization was confirmed by evaluating the fluorescence of the film. Both the dots and the surface exhibit the same fluorescence (the film itself is not fluorescent).
The self-standing surface has been used as an active packaging material to increase the shelf life of food. Even though the mechanism is not yet fully defined, the surface functionalized with CD-Lico has shown intriguing potential in combating mold formation on fruits.

Future perspectives:
Although all the results obtained are very interesting and scientifically significant, there is still much work to be done, and there are many questions that need to be clarified. It is necessary to clarify the role of the acid catalyst in the synthesis of this system, particularly to understand the role of boric acid in promoting structures with better photoactive properties compared to those obtained with another acid catalyst, such as hydrochloric acid. It is necessary to gain a better understanding of the structure of these nanoparticles. Despite the comprehensive study of CD-Boron, the actual structure of this system is still hard to identify. Lastly, it is essential to complete all the studies on CD-Lico carbon dots, which have shown promise as a nanomaterial in combating bacteria, and as an "additive" for food packaging to

extend the shelf life of food. It is essential to assess the potential contamination of food in active packaging and the actual toxicity of the dots in case of contact with food.

Bibliography

[1]: LePan, N. Visualizing the History of Pandemics, Infographic: The History of Pandemics, by Death. Toll, 2020

[2]: Palgen, J. L.; Feraoun, Y.; Dzangué-Tchoupou, G.; Joly, C.; Martinon, F.; Le Grand, R.; Beignon, A. S. Optimize Prime/Boost Vaccine Strategies: Trained Immunity as a New Player in the Game. Front. Immunol., 2021, 12:612747.

[3]: Collins, H. M.; Metz, S. W. Progress and Works in Progress: Update on Flavivirus Vaccine Development, Clinical Therapeutics, 2017, 39, 1519-1536.

[4]: Munoz-Bonilla, A.; Fernandez-Garcıa, M. Polymeric materials with antimicrobial activity. Prog. Polym. Sci. 2012, 37, 281–339.

[5]: Fullenkamp, D.E.; et al. Mussel-inspired silver-releasing antibacterial hydrogels. Biomaterials, 2012, 33, 3783–3791.

[6]: Pinna, A.; Figus, C.; Lasio, B.; Piccinini, M.; Malfatti, L.; Innocenzi, P. Release of Ceria Nanoparticles Grafted on Hybrid Organic–Inorganic Films for Biomedical Application. ACS Applied Materials & Interfaces, 2012, 4, 3916-3922.

[7]: Buffet-Bataillon, S.; et al. Emergence of resistance to antibacterial agents: the role of quaternary ammonium compounds – a critical review. Int. J. Antimicrob. Agents, 2012, 39, 381–389.

[8]: Hasan, J.; Crawford, R. J.; Ivanova, E. P. Trends Biotechnol., 2013, 31, 295-304

[9]: Innocenzi, P.; Stagi, L. Carbon-based antiviral nanomaterials: graphene, C-dots, and fullerenes. A perspective. Chem. Sci., 2020, 11, 6606

[10]: Liu, Q.; Guo, B.; Rao, Z.; Zhang, B.; Gong J. R. Strong Two-Photon-Induced Fluorescence from Photostable, Biocompatible Nitrogen-Doped Graphene Quantum Dots for Cellular and Deep-Tissue Imaging. Nano Lett., 2013, 13, 2436–2441.

[11]: S. Zhu, J. Zhang, C. Qiao, S. Tang, Y. Li, W. Yuan, B. Li, L. Tian, F. Liu, R. Hu, H. Gao, H. Wei, H. Zhang, H. Sun and B. Yang, Chem. Commun., 2011, 47, 6858–6860.

[12]: Zhu, S. J.; Zhang, J. H.; Liu, X.; Li, B.; Wang, X. F.; Tang, S. T.; Meng, Q. N.; Li, Y. F.; Shi, C.; Hu R.; Yang, B. RSC Adv., 2012, 2, 2717–2720.

[13]: Duman, A.N.; Colak, S.G.; Alas, M.O.; Er, O.; Tuncel, A.; Ozturk, I.; Yurt, F.; Genc, R.; Ocakoglu, K. Enhanced bacterial uptake of 131I -labeled antimicrobial imidazolium bromide salts using fluorescent carbon nanodots. Mater. Today Commun. 2021, 26.

[14]: Otis, G.; Bhattacharya, S.; Malka, O.; Kolusheva, S.; Bolel, P.; Porgador, A.; Jelinek, R. Selective Labeling and Growth Inhibition of Pseudomonas aeruginosa by Aminoguanidine Carbon Dots. ACS Infect. Dis. 2019, 5, 292–302.

[15]: Das, P.; Maruthapandi, M.; Saravanan, A.; Natan, M.; Jacobi, G.; Banin, E.; Gedanken, A. Carbon Dots for Heavy-Metal Sensing, pH-Sensitive Cargo Delivery, and Antibacterial Applications. ACS Appl. Nano Mater. 2020, 3, 11777–11790.

[16]: Xu, X.; Ray, R.; Gu, Y.; Ploehn, H. J.; Gearheart, L.; Raker, K.; Scrivens, W. A. Electrophoretic Analysis and Purification of Fluorescent Single-Walled Carbon Nanotube Fragments. J. Am. Chem. Soc. 2004, 126 (40), 12736–12737.

[17]: Kang, Z.; Lee, S.T. Nanoscale, 2019, 11, 19214-19224.

[18]: Cayuela, A.; Soriano, M. L.; Carrillo-Carrión, C.; Valcárcel, M. Semiconductor and Carbon-Based Fluorescent Nanodots: The Need for Consistency. Chem. Commun. 2016, 52 (7), 1311–1326.

[19]: Hutton, G. A. M. M.; Martindale, B. C. M. M.; Reisner, E. Carbon Dots as Photosensitisers for Solar-Driven Catalysis. Chem. Soc. Rev. 2017, 46 (20), 6111–6123.

[20]: de Medeiros, T. V.; Manioudakis, J.; Noun, F.; Macairan, J.-R.; Victoria, F.; Naccache, R. Microwave-Assisted Synthesis of Carbon Dots and Their Applications. J. Mater. Chem. C 2019, 7, 7175–7195.

[21]: Xia, C.; Zhu, S.; Feng, T.; Yang, M.; Yang, B. Evolution and Synthesis of Carbon Dots : From Carbon Dots to Carbonized Polymer Dots. Adv. Sci. 2019, 1901316.

[22]: Li, S.; Li, L.; Tu, H.; Zhang, H.; Silvester, D. S.; Banks, C. E.; Zou, G.; Hou H.; Ji, X.; The development of carbon dots: From the perspective of materials chemistry, Materials Today, 2021, 51, 188-207.

[23]: Xia, C.; Zhu, S.; Feng, T.; Yang, M.; Yang, B.; Evolution and Synthesis of Carbon Dots: From Carbon Dots to Carbonized Polymer Dots, Adv. Sci. 2019, 6, 1901316.
[24]: Zheng, X.T.; Ananthanarayanan, A.; Luo, K. Q.; Chen, P. Glowing Graphene Quantum Dots and Carbon Dots: Properties, Syntheses, and Biological Applications, Small, 2015, 11(14), 1620–1636.
[25]: Yan, F.; Sun, Z.; Zhang, H.; Sun, X.; Jiang, Y.; Bai, Z. The fluorescence mechanism of carbon dots, and methods for tuning their emission color: a review. Microchimica Acta, 2019, 186(8), 583.
[26]: Wang B.; Lu, S. The light of carbon dots: From mechanism to applications, Matter, 2022, 5, 110–149.
[27]: Chen B. B.; Liu M. L.; Li C. M.; Huang C. Z. Fluorescent carbon dots functionalization, Advances in Colloid and Interface Science, 2019, 270, 165–190.
[28]: Yan, F.; Jiang, Y.; Sun, X. et al. Surface modification and chemical functionalization of carbon dots: a review, Microchim Acta, 2018, 185, 424.
[29]: Li, L.; Dong, T. Photoluminescence Tuning in Carbon Dots: Surface Passivation or/and Functionalization, Heteroatom Doping, Journal of Materials Chemistry C, 2018, 10, 1039.
[30]: Havrdova M.; Hola K.; Skopalik J.; Tomankova K.; Petr M.; Cepe K.; Polakova K.; Tucek J.; Bourlinos A. B.; Zboril R. Toxicity of carbon dots – Effect of surface functionalization on the cell viability, reactive oxygen species generation and cell cycle, Carbon, 2016, 99, 238-248.
[31]: Liu, J. H.; Yang, S. T.; Chen, X. X.; Wang, H. Fluorescent Carbon Dots and Nanodiamonds for Biological Imaging: Preparation, Application, Pharmacokinetics and Toxicity, Current Drug Metabolism, 2012, 13(8), 1046–1056.
[32]: Emam A.N.; Loutfy S. A.;Mostafa A. A.; Awad H.; Mohamed M. B. Cyto-toxicity, biocompatibility and cellular response of carbon dots–plasmonic based nanohybrids for bioimaging, RSC Adv., 2017, 7, 23502.
[33]: Xia C.; ZhuS.; Feng T.; Yang M.; Yang B. Evolution and Synthesis of Carbon Dots: From Carbon Dots to Carbonized Polymer Dots, Adv. Sci. 2019, 6, 1901316.

[34]: Cui, L.; Ren, X.; Sun, M.; Liu, H.; Xia, L. Carbon Dots: Synthesis, Properties and Applications, Nanomaterials, 2021, 11, 3419.
[35]: El-Shabasy, R.M.; Farouk Elsadek, M.; Mohamed Ahmed, B.; Fawzy Farahat, M.; Mosleh, K.N.; Taher, M.M. Recent Developments in Carbon Quantum Dots: Properties, Fabrication Techniques, and Bio-Applications, Processes, 2021, 9, 388.
[36]: Nguyen, V.; Zhao, N.; Yan, L.; Zhong, P.; Le, P.H. Double-pulse femtosecond laser ablation for synthesis of ultrasmall carbon nanodots. Mater. Res. Express 2020, 7, 015606.
[37]: Gonçalves, H.; Duarte, A.J.; da Silva, J.C.E. Optical fiber sensor for Hg(II) based on carbon dots. Biosens. Bioelectron. 2010, 26, 1302–1306.
[38]: Małolepszy, A.; Blonski, S.; Chrzanowska-Gi˙zy´ nska, J.; Wojasi ´ nski, M.; Plocinski, T.; Stobinski, L.; Szymanski, Z. Fluorescent carbon and graphene oxide nanoparticles synthesized by the laser ablation in liquid. Appl. Phys. A 2018, 124, 282.
[39]: Kaczmarek, A.; Hoffman, J.; Morgiel, J.; Mo´scicki, T.; Stobi ´ nski, L.; Szyma´ nski, Z.; Małolepszy, A. Luminescent Carbon Dots Synthesized by the Laser Ablation of Graphite in Polyethylenimine and Ethylenediamine. Materials 2021, 14, 729.
[40]: Su, Y.; Xie, M.; Lu, X.;Wei, H.; Geng, H.; Yang, Z.; Zhang, Y. Facile synthesis and photoelectric properties of carbon dots with upconversion fluorescence using arc-synthesized carbon by-products. RSC Adv. 2013, 4, 4839–4842.
[41]: Dey, S.; Govindaraj, A.; Biswas, K.; Rao, C.N.R. Luminescence properties of Boron and nitrogen doped graphene quantum dots prepared from arc-discharge-generated doped graphene samples. Chem. Phys. Lett. 2014, 595–596, 203–208.
[42]: Crista, D.M.A.; Esteves da Silva, J.C.G.; Pinto da Silva, L. Evaluation of Different Bottom-up Routes for the Fabrication of Carbon Dots. Nanomaterials 2020, 10, 1316.
[43]: Gong, N.; Wang, H.; Li, S.; Deng, Y.; Chen, X.; Ye, L.; Gu, W. Microwave-Assisted Polyol Synthesis of Gadolinium-Doped Green Luminescent Carbon Dots as a Bimodal Nanoprobe. Langmuir 2014, 30, 10933–10939.

[44]: Li, H.; Shao, F.-Q.; Zou, S.-Y.; Yang, Q.-J.; Huang, H.; Feng, J.-J.;Wang, A.-J. Microwave-assisted synthesis of N,P-doped carbon dots for fluorescent cell imaging. Microchim. Acta 2015, 183, 821–826.
[45]: Tabaraki, R.; Sadeghinejad, N. Microwave assisted synthesis of doped carbon dots and their application as green and simple turn off–on fluorescent sensor for mercury (II) and iodide in environmental samples. Ecotoxicol. Environ. Saf. 2018, 153, 101–106.
[46]: Romero, M.P.; Alves, F.; Stringasci, M.D.; Buzzá, H.H.; Ciol, H.; Inada, N.M.; Bagnato, V.S. One-Pot Microwave-Assisted Synthesis of Carbon Dots and in vivo and in vitro Antimicrobial Photodynamic Applications. Front. Microbiol. 2021, 12, 662149.
[47]: Wang, J.; Wei, J.; Su, S.; Qiu, J. Novel fluorescence resonance energy transfer optical sensors for vitamin B12 detection using thermally reduced carbon dots. New J. Chem. 2015, 39, 501–507.
[48]: Zheng, M.; Ruan, S.; Liu, S.; Sun, T.; Qu, D.; Zhao, H.; Xie, Z.; Gao, H.; Jing, X.; Sun, Z. Self-Targeting Fluorescent Carbon Dots for Diagnosis of Brain Cancer Cells. ACS Nano 2015, 9, 11455–11461.
[49]: Feng, T.; Ai, X.; An, G.; Yang, P.; Zhao, Y. Charge-Convertible Carbon Dots for Imaging-Guided Drug Delivery with Enhanced in Vivo Cancer Therapeutic Efficiency. ACS Nano 2016, 10, 4410–4420.
[50]: Dong, Y.; Pang, H.; Bin Yang, H.; Guo, C.; Shao, J.; Chi, Y.; Li, C.M.; Yu, T. Carbon-Based Dots Co-doped with Nitrogen and Sulfur for High Quantum Yield and Excitation-Independent Emission. Angew. Chem. Int. Ed. 2013, 52, 7800–7804.
[51]: Qian, Z.; Shan, X.; Chai, L.; Ma, J.; Chen, J.; Feng, H. Si-Doped Carbon Quantum Dots: A Facile and General Preparation Strategy, Bioimaging Application, and Multifunctional Sensor. ACS Appl. Mater. Interfaces 2014, 6, 6797–6805.
[52]: Shan, X.; Chai, L.; Ma, J.; Qian, Z.; Chen, J.; Feng, H. B-doped carbon quantum dots as a sensitive fluorescence probe for hydrogen peroxide and glucose detection. Analyst 2014, 139, 2322–2325.

[53]: Mitra, S.; Chandra, S.; Kundu, T.; Banerjee, R.; Pramanik, P.; Goswami, A. Rapid Microwave Synthesis of Fluorescent Hydrophobic Carbon Dots. RSC Adv. 2012, 2 (32), 12129.
[54]: Yan, L.; Yang, Y.; Ma, C. Q.; Liu, X.; Wang, H.; Xu, B. Synthesis of Carbon Quantum Dots by Chemical Vapor Deposition Approach for Use in Polymer Solar Cell as the Electrode Buffer Layer. Carbon 2016, 109, 598–607.
[55]: Yang, H.; Liu, Y.; Guo, Z.; Lei, B.; Zhuang, J.; Zhang, X.; Liu, Z.; Hu, C. Hydrophobic Carbon Dots with Blue Dispersed Emission and Red Aggregation-Induced Emission. Nat. Commun. 2019, 10 (1), 1789.
[56]: Prikhozhdenko, E. S.; Bratashov, D. N.; Mitrofanova, A. N.; Sapelkin, A. V.; Yashchenok, A. M.; Sukhorukov, G. B.; Goryacheva, I. Y. Solvothermal Synthesis of Hydrophobic Carbon Dots in Reversed Micelles. J. Nanoparticle Res. 2018, 20, 234–254.
[57]: Yan, F.; Jiang, Y.; Sun, X.; Bai, Z.; Zhang, Y.; Zhou, X. Surface Modification and Chemical Functionalization of Carbon Dots: A Review. Microchimica Acta. Microchimica Acta 2018.
[58]: Nurunnabi, M.; Khatun, Z.; Huh, K. M.; Park, S. Y.; Lee, D. Y.; Cho, K. J.; Lee, Y. K. In Vivo Biodistribution and Toxicology of Carboxylated Graphene Quantum Dots. ACS Nano 2013, 7 (8), 6858–6867.
[59]: Ding, C.; Zhu, A.; Tian, Y. Functional Surface Engineering of C-Dots for Fluorescent Biosensing and in Vivo Bioimaging. Acc. Chem. Res. 2014, 47 (1), 20–30.
[60]: Luo, P. G.; Yang, F.; Yang, S.-T.; Sonkar, S. K.; Yang, L.; Broglie, J. J.; Liu, Y.; Sun, Y.-P. Carbon-Based Quantum Dots for Fluorescence Imaging of Cells and Tissues. RSC Adv. 2014, 4 (21), 10791.
[61]: Du, J.; Xu, N.; Fan, J.; Sun, W.; Peng, X. Carbon Dots for In Vivo Bioimaging and Theranostics. Small 2019, 15, 1805087.
[62]: Wang, K.; Gao, Z.; Gao, G.; Wo, Y.; Wang, Y.; Shen, G.; Cui, D. Systematic Safety Evaluation on Photoluminescent Carbon Dots. Nanoscale Res. Lett. 2013, 8, 1–9.

[63]: Arcudi, F.; Đorđević, L.; Prato, M.; Arcudi, F.; Dordevic, L. Rationally Designed Carbon NanoDots En Route to Pure White-Light Emission. Angew. Chem. Int. Ed. 2017, 56 (15), 4170–4173.
[64]: Miao, X.; Qu, D.; Yang, D.; Nie, B.; Zhao, Y.; Fan, H.; Sun, Z. Synthesis of Carbon Dots with Multiple Color Emission by Controlled Graphitization and Surface Functionalization. Adv. Mater. 2018, 30 (1), 1704740.
[65]: Zhang, F.; Liu, F.; Wang, C.; Xin, X.; Liu, J.; Guo, S.; Zhang, J. Effect of Lateral Size of Graphene Quantum Dots on Their Properties and Application. ACS Appl. Mater. Interfaces 2016, 8 (3), 2104–2110.
[66]: Molaei, M. J. A Review on Nanostructured Carbon Quantum Dots and Their Applications in Biotechnology, Sensors, and Chemiluminescence. Talanta 2019, 196, 456–478.
[67]: Tepliakov, N. V.; Kundelev, E. V.; Khavlyuk, P. D.; Xiong, Y.; Leonov, M. Y.; Zhu, W.; Baranov, A. V.; Fedorov, A. V.; Rogach, A. L.; Rukhlenko, I. D. Sp2–Sp3-Hybridized Atomic Domains Determine Optical Features of Carbon Dots. ACS Nano 2019, acsnano.9b05444.
[68]: Qiao, Z.A.;Wang, Y.; Gao, Y.; Li, H.; Dai, T.; Liu, Y.; Huo, Q. Commercially activated carbon as the source for producing multicolor photoluminescent carbon dots by chemical oxidation. Chem. Commun. 2010, 46, 8812–8814.
[69]: Bourlinos, A.B.; Zboˇril, R.; Petr, J.; Bakandritsos, A.; Krysmann, M.; Giannelis, E.P. Luminescent Surface Quaternized Carbon Dots. Chem. Mater. 2012, 24, 6–8. [55]: Pan, L.; Sun, S.; Zhang, A.; Jiang, K.; Zhang, L.; Dong, C.; [70] Huang, Q.; Wu, A.; Lin, H. Truly Fluorescent Excitation-Dependent Carbon Dots and Their Applications in Multicolor Cellular Imaging and Multidimensional Sensing. Adv. Mater. 2015, 27, 7782–7787.
[71]: Wang, C.; Xu, Z.; Zhang, C. Polyethyleneimine-Functionalized Fluorescent Carbon Dots: Water Stability, pH Sensing, and Cellular Imaging. ChemNanoMat 2015, 1, 122–127.
[72]: Pan, D.; Zhang, J.; Li, Z.;Wu, C.; Yan, X.;Wu, M. Observation of pH, solvent-, spin-, and excitation-dependent blue photoluminescence from carbon nanoparticles. Chem. Commun. 2010, 46, 3681–3683.

[73]: Kozák, O.; Datta, K.K.; Greplová, M.; Ranc, V.; Kašlík, J.; Zboˇril, R. Surfactant-Derived Amphiphilic Carbon Dots with Tunable Photoluminescence. J. Phys. Chem. C 2013, 117, 24991–24996.
[74]: Wang, X.; Wang, S.T.; Lu, F.; Meziani, M.J.; Tian, L.; Sun, K.W.; Bloodgood, M.A.; Sun, Y.P. Bandgap-like strong fluorescence in functionalized carbon nanoparticles. Angew. Chem. Int. Ed. 2010, 122, 5438–5442.
[75]: Zhu, S.; Meng, Q.; Wang, L.; Zhang, J.; Song, Y.; Jin, H.; Zhang, K.; Sun, H.; Wang, H.; Yang, B. Highly Photoluminescent Carbon dots for multicolor patterning, sensors and bioimaging. Angew. Chem. Int. Ed. 2013, 125, 4045–4049.
[76]: Hou, J.; Wang, W.; Zhou, T.; Wang, B.; Li, H.; Ding, L. Synthesis and Formation Mechanistic Investigation of Nitrogen- Doped Carbon-Dots with High Quantum Yield and Yellowish-Green Fluorescence. Nanoscale 2016, 8, 11185–11193.
[77]: Pan, L.; Sun, S.; Zhang, A.; Jiang, K.; Zhang, L.; Dong, C.; Huang, Q.; Wu, A.; Lin, H.Truly Fluorescent Excitation-Dependent Carbon Dots and Their Applications in Multicolor Cellular Imagingand Multidimensional Sensing. Adv. Mater. 2015, 27, 7782–7787.
[78]: Park, Y.; Yoo, J.; Lim, B.; Kwon, W.; Rhee, S.-W. Improving the Functionality of Carbon Nanodots: Doping and Surface Functionalization. J. Mater. Chem. A 2016, 4, 11582–11603.
[79]: Liu, M. L.; Chen, B. Bin; Li, C. M.; Huang, C. Z. Carbon Dots: Synthesis, Formation Mechanism, Fluorescence Origin and Sensing Applications. Green Chem. 2019, 21 (3), 449–471.
[80]: Wang, X.; Feng, Y.; Dong, P.; Huang, J. A Mini Review on Carbon Quantum Dots: Preparation, Properties, and Electrocatalytic Application. Front. Chem. 2019, 7 (October), 1–9.
[81]: Molaei, M. J. A Review on Nanostructured Carbon Quantum Dots and Their Applications in Biotechnology, Sensors, and Chemiluminescence. Talanta 2019, 196, 456–478.
[82]: Strauss, V.; Margraf, J. T.; Dolle, C.; Butz, B.; Nacken, T. J.; Walter, J.; Bauer, W.; Peukert, W.; Spiecker, E.; Clark, T.; et al. Carbon Nanodots: Toward a

Comprehensive Understanding of Their Photoluminescence. J. Am. Chem. Soc. 2014, 136 (49), 17308–17316.
[83]: Li, L.; Dong, T. Photoluminescence Tuning in Carbon Dots: Surface Passivation or/and Functionalization, Heteroatom Doping. J. Mater. Chem. C 2018, 6 (30), 7944–7970.
[84]: Yao, B.; Huang, H.; Liu, Y.; Kang, Z. Carbon Dots: A Small Conundrum. Trends Chem. 2019, 1 (2), 235–246.
[85]: Hu, C.; Li, M.; Qiu, J.; Sun, Y. P. Design and Fabrication of Carbon Dots for Energy Conversion and Storage. Chem. Soc. Rev. 2019, 48 (8), 2315–2337.
[86]: Jaleel, J. A.; Pramod, K. Artful and Multifaceted Applications of Carbon Dot in Biomedicine. J. Control. Release 2018, 269 (November 2017), 302–321.
[87]: Nguyen, V.; Si, J.; Yan, L.; Hou, X. Electronehole recombination dynamics in carbon nanodots. Carbon, 2015, 659-663.
[88]: Li, Y.; Liu, C.; Sun, H.; Chen, M.; Hou, D.; Zheng, Y.; Xie, H.; Zhou, B.; Lin, X. Formation and Band Gap Tuning Mechanism of Multicolor Emissive Carbon Dots from m-Hydroxybenzaldehyde. Adv. Sci., 2023, 10, 2300543.
[89]: Ding, H.; Yu, S. B.; Wei, J. S.; Xiong, H. M. Full-Color Light-Emitting Carbon Dots with a Surface-State-Controlled Luminescence Mechanism. ACS Nano, 2015.
[90]: Liu, T.; Yu, K.; Gao, L.; Chen, H.; Wang, N.; Hao, L.; Li, T.; He, H.; Guo, Z. A Graphene Quantum Dot Decorated SrRuO3 Mesoporous Film as an Efficient Counter Electrode for High-Performance Dye-Sensitized Solar Cells. J. Mater. Chem. A 2017, 5 (34), 17848–17855.
[91]: Huang, X.; Zhang, F.; Zhu, L.; Choi, K. Y.; Guo, N.; Guo, J.; Tackett, K.; Anilkumar, P.; Liu, G.; Quan, Q.; et al. Effect of Injection Routes on the Biodistribution, Clearance, and Tumor Uptake of Carbon Dots. ACS Nano 2013, 7 (7), 5684–5693.
[92]: Parvin, N.; Mandal, T. K. Synthesis of a Highly Fluorescence Nitrogen-Doped Carbon Quantum Dots Bioimaging Probe and Its in Vivo Clearance and Printing Applications. RSC Adv. 2016, 6 (22), 18134–18140.

[93]: Zheng, M.; Liu, S.; Li, J.; Qu, D.; Zhao, H.; Guan, X.; Hu, X.; Xie, Z.; Jing, X.; Sun, Z. Integrating Oxaliplatin with Highly Luminescent Carbon Dots: An Unprecedented Theranostic Agent for Personalized Medicine. Adv. Mater. 2014, 26 (21), 3554–3560.
[94]: Li, J.; Yang, S.; Deng, Y.; Chai, P.; Yang, Y.; He, X.; Xie, X.; Kang, Z.; Ding, G.; Zhou, H.; et al. Emancipating Target-Functionalized Carbon Dots from Autophagy Vesicles for a Novel Visualized Tumor Therapy. Adv. Funct. Mater. 2018, 28 (30), 1–9.
[95]: Lai, C.W.; Hsiao, Y. H.; Peng, Y. K.; Chou, P. T.; et al. Facile synthesis of highly emissive carbon dots from pyrolysis of glycerol; gram scale production of carbon dots/mSiO2 for cell imaging and drug release. J. Mater. Chem., 2012, 22, 14403–14409
[96]: Mishra, V.; Patil, A.; Thakur, S.; Kesharwani, P. Carbon Dots: Emerging Theranostic Nanoarchitectures. Drug Discovery Today. Elsevier Ltd 2018, pp 1219–1232.
[97]: Liu, J.; Liu, Y.; Liu, N.; Han, Y.; Zhang, X.; Huang, H.; Lifshitz, Y.; Lee, S. T.; Zhong, J.; Kang, Z. Metal-Free Efficient Photocatalyst for Stable Visible Water Splitting via a Two-Electron Pathway. Science 2015, 347 (6225), 970–974.
[98]: Zhang, P.; Wang, T.; Chang, X.; Zhang, L.; Gong, J. Synergistic Cocatalytic Effect of Carbon Nanodots and Co3O4 Nanoclusters for the Photoelectrochemical Water Oxidation on Hematite. Angew. Chem. Int. Ed. 2016, 55 (19), 5851–5855.
[99]: Zhang, X.; Wang, F.; Huang, H.; Li, H.; Han, X.; Liu, Y.; Kang, Z. Carbon Quantum Dot Sensitized TiO_2 Nanotube Arrays for Photoelectrochemical Hydrogen Generation under Visible Light. Nanoscale 2013, 5 (6), 2274–2278.
[100]: Cao, L.; Sahu, S.; Anilkumar, P.; Bunker, C. E.; Xu, J.; Fernando, K. A. S.; Wang, P.; Guliants, E. A.; Tackett, K. N.; Sun, Y. P. Carbon Nanoparticles as Visible-Light Photocatalysts for Efficient CO 2 Conversion and Beyond. J. Am. Chem. Soc. 2011, 133 (13), 4754–4757.
[101]: Qing, M.; Meng, Y.; Wang, Y.; Li, X.; Zhou, C.; Liang, Y.; Zhang, Z.; Liu, Q.; Guo, Y.; Xiao, D. Building Nanoparticle-Stacking MoO2-CDs via in-Situ

Carbon Dots Reduction as High-Performance Anode Material for Lithium Ion and Sodium Ion Batteries. Electrochim. Acta 2019, 319, 740–752.
[102]: Feng, H.; Xie, P.; Xue, S.; Li, L.; Hou, X.; Liu, Z.; Wu, D.; Wang, L.; Chu, P. K. Synthesis of Three-Dimensional Porous Reduced Graphene Oxide Hydrogel/Carbon Dots for High-Performance Supercapacitor. J. Electroanal. Chem. 2018, 808 (December 2017), 321–328.
[103]: Li, X.; Rui, M.; Song, J.; Shen, Z.; Zeng, H. Carbon and Graphene Quantum Dots for Optoelectronic and Energy Devices: A Review. Adv. Funct. Mater. 2015, 25 (31), 4929–4947.
[104]: Zhou, D.; Li, D.; Jing, P.; Zhai, Y.; Shen, D.; Qu, S.; Rogach, A. L. Conquering Aggregation-Induced Solid-State Luminescence Quenching of Carbon Dots through a Carbon Dots-Triggered Silica Gelation Process. Chem. Mater. 2017, 29 (4), 1779–1787.
[105]: Zhang, X. X.; Wang, F.; Huang, H.; Li, H.; Han, X.; Liu, Y.; Kang, Z.; Zhang, Y.; Wang, Y. Y. Y.; Kalytchuk, S.; et al. Color-Switchable Electroluminescence of Carbon Dot Light-Emitting Diodes. ACS Nano 2013, 7 (12), 11234–11241.
[106]: Guo, X.; Wang, C.-F. F.; Yu, Z.-Y. Y.; Chen, L.; Chen, S.; Chen*, S. Facile Access to Versatile Fluorescent Carbon Dots toward Light-Emitting Diodes. Chem. Commun. 2012, 48 (21), 2692–2694
[107]: Chen, Y.; Zheng, M.; Xiao, Y.; Dong, H.; Zhang, H.; Zhuang, J.; Hu, H.; Lei, B.; Liu, Y. A Self-Quenching-Resistant Carbon-Dot Powder with Tunable Solid-State Fluorescence and Construction of Dual-Fluorescence Morphologies for White Light-Emission. Adv. Mater. 2016, 28 (2), 312–318.
[108]: Yeh, T. F.; Teng, C. Y.; Chen, S. J.; Teng, H. Nitrogen-Doped Graphene Oxide Quantum Dots as Photocatalysts for Overall Water-Splitting under Visible Light Illumination. Adv. Mater. 2014, 26 (20), 3297–3303.
[109]: Li, Y.; Hu, Y.; Zhao, Y.; Shi, G.; Deng, L.; Hou, Y.; Qu, L.; Zhou, J.; Booker, C.; Li, R.; et al. An Electrochemical Avenue to Green-Luminescent Graphene Quantum Dots as Potential Electron-Acceptors for Photovoltaics. Adv. Mater. 2011, 23 (6), 776–780.

[110]: Chao, D.; Zhu, C.; Xia, X.; Liu, J.; Zhang, X.; Wang, J.; Liang, P.; Lin, J.; Zhang, H.; Shen, Z. X.; et al. Graphene Quantum Dots Coated VO 2 Arrays for Highly Durable Electrodes for Li and Na Ion Batteries. Nano Lett. 2015, 15 (1), 565–573.

[111]: Kotta, S.; Aldawsari, H. M.; Badr-Eldin, S. M.; et al. Exploring thepotential of carbon dots to combat COVID-19. Front MolBiosci. 2020, 7:616575.

[112]: Zhao, C.; Wu, L.; Wang, X.; et al. Quaternary ammonium carbonquantum dots as an antimicrobial agent against Gram-positive bacteria for the treatment of MRSA-infectedpneumonia in mice. Carbon, 2020, 163, 70-84.

[113]: Kuo, W. S.; Chang, C. Y.; Chen, H. H.; et al. Two-photon photo-excited photodynamic therapy and contrast agent with antimicrobial graphene quantum dots. ACS Appl Mater Interfaces. 2016, 8, 30467-30474.

[114]: Huang, S.; Gu, J.; Ye, J.; et al. Benzoxazine monomer derived carbon-dots as a broad-spectrum agent to block viral infectivity. J Colloid Interface Sci. 2019, 542, 198-206.

[115]: Abu Rabe, D. I.; Al Awak, M. M.; Yang, F.; et al. The dominant role of surface functionalization in carbon dots' photo-activated antibacterial activity. Int J Nanomedicine. 2019, 14, 2655-2665.

[116]: Pandiyan, S.; Arumugam, L.; Srirengan, S. P.; et al. Biocompatible carbon quantum dots derived from sugarcane industrial wastes for effective nonlinear optical behavior and anti-microbial activity applications. ACS Omega, 2020, 5, 30363-30372.

[117]: Dong, X.; Edmondson, R.; Yang, F.; et al. Carbon dots for effective photodynamic inactivation of virus. RSC Adv., 2020, 10, 33944-33954.

[118]: Barras, A.; Pagneux, Q.; Sane, F.; et al. High efficiency of functional carbon nanodots as entry inhibitors of herpes simplex virus type1. ACS Appl Mater Interfaces., 2016, 8, 9004-9013.

[119]: Tong, T.; Hu, H.; Zhou, J.; et al. Glycyrrhizic-acid-based carbondots with high antiviral activity by multisite inhibition mechanisms. Small., 2020, 16, e1906206.

[120]: Ting, D.; Dong, N.; Fang, L.; et al. Multisite inhibitors for enteric coronavirus: antiviral cationic carbon dots based on curcumin. ACS Appl Nano Mater., 2018 1, 5451-5459.
[121]: Knoblauch, R.; Harvey, A.; Ra, E.; et al. Antimicrobial carbon nanodots: photodynamic inactivation and dark antimicrobial effects on bacteria by brominated carbon nanodots. Nanoscale., 2021, 13, 85-99.
[122]: Ma, Y.; Zhang, M.; Wang, H.; et al. N-doped carbon dots derived from leaves with low toxicity via damaging cytomembrane for broad-spectrum antibacterial activity. Mater Today Commun., 2020, 24, 101222.
[123]: Wang, H.; Song, Z.; Gu, J.; Li, S.; Wu, Y.; Han, H.; Nitrogen-doped carbon quantum dots for preventing biofilm formation and eradicating drug-resistant bacteria infection. ACS Biomater Sci Eng., 2019, 5, 4739-4749.
[124]: Jijie, R.; Barras, A.; Bouckaert, J.; Dumitrascu, N.; Szunerits, S.; Boukherroub, R.; Enhanced antibacterial activity of carbon dots functionalized with ampicillin combined with visible light triggered photodynamic effects. Colloids Surf B Biointerfaces., 2018, 170, 347-354.
[125]: Sun, B.; Wu, F.; Zhang, Q.; et al. Insight into the effect of particle size distribution differences on the antibacterial activity of carbon dots. J Colloid Interface Sci., 2021, 584, 505-519.
[126]: Li, P.; Sun, L.; Xue, S.; et al. Recent advances of carbon dots as new antimicrobial agents. SmartMat., 2022, 3, 226-248.
[127]: Wilson, W. W.; Wade, M. M.; Holman, S. C.; Champlin, F. R. Status of methods for assessing bacterial cell surface charge properties based on zeta potential measurements. J Microbiol Methods., 2001, 43, 153-164.
[128]: Bing, W.; Sun, H.; Yan, Z.; Ren, J.; Qu, X. Programmed bacteria death induced by carbon dots with different surface charge. Small., 2016, 12, 4713-4718.
[129]: Verma, A.; Arshad, F.; Ahmad, K.; et al. Role of surface charge in enhancing antibacterial activity of fluorescent carbon dots. Nanotechnology., 2020, 31, 095101.

[130]: Gagic, M.; Kociova, S.; Smerkova, K.; et al. One-pot synthesis of natural amine-modified biocompatible carbon quantum dots with antibacterial activity. J Colloid Interface Sci., 2020, 580, 30-48.
[131]: Abbaszadegan, A.; Ghahramani, Y.; Gholami, A.; et al. The effect of charge at the surface of silver nanoparticles on antimicrobial activity against Gram-positive and Gram-negative bacteria: a preliminary study. J Nanomater., 2015, 1-8.
[132]: Priyadarshini, E.; Rawat, K.; Prasad, T.; Bohidar, H. B. Antifungal efficacy of Au@ carbon dots nanoconjugates against opportunistic fungal pathogen, Candida albicans, Colloids and Surfaces B: Biointerfaces, 2018, 163, 355-361.
[133]: Ezati, P.; Rhim, J. W.; Molaei, R.; Priyadarshi, R.; Roy, S.; Min, S.; Kim, Y. H.; Lee, S. G.; Han, S. Preparation and characterization of B, S, and N-doped glucose carbon dots: Antibacterial, antifungal, and antioxidant activity, Sustainable Materials and Technologies, 2022, 32, e00397.
[134]: Liu, Y.; Li, W.; Wu, K.; Lei, B.; Chen, J.; Zhang, X.; Lei, H.; Duan, X.; Huang, R. Antifungal molecular details of MNQ-derived novel carbon dots against Penicillium digitatum, Food Chemistry, 2023, 413, 135687.
[135]: Ezati, P.; Rhim, J. W.; Molaei, R.; Rezaei, Z. Carbon quantum dots-based antifungal coating film for active packaging application of avocado, Food Packaging and Shelf Life, 2022, 33, 100878.
[136]: Cao, Y.; Dong, H.; Yang, Z.; Zhong, X.; Chen, Y.; Dai, W.; Zhang, X. Aptamer conjugated graphene quantum dots/porphyrin derivative theranostic agent for intracellular cancer-related microRNA detection and fluorescence-guided photothermal/photodynamic synergetic therapy, ACS Appl. Mater. Interfaces, 2017, 9, 159–166.
[137]: Yang, K.; Wang, C.; Liu, C. et al. Bioluminescence-initiated photodynamic therapy bridged on high-luminescent carbon dots-conjugated protoporphyrin IX. J Mater Sci, 2019, 54, 3383–3391.
[138]: Wang, J.; Zhang, Z.; Zha, S.; Zhu, Y.; Wu, P.; Ehrenberg, B.; Chen, J. Y. Carbon nanodots featuring efficient FRET for two-photon photodynamic cancer therapy with a low fs laser power density, Biomaterials, 2014, 35, 9372-9381.

[139]: Sun, Y.; Zhang, M.; Bhandari, B.; Yang, C. Recent Development of Carbon Quantum Dots: Biological Toxicity, Antibacterial Properties and Application in Foods, Food Reviews International, 2022, 38, 1513-1532.
[140]: Fernando, K. A.; Sahu, S.; Liu, Y.; Lewis, W. K.; Guliants EA, Jafariyan A, et al. Carbon quantum dots and applications in photocatalytic energy conversion. ACS Appl Mater Interfaces, 2015, 7, 8363–76.
[141]: Das, G. S.; Tripathi, K. M.; Kumar, G.; Paul, S.; Mehara, S.; Bhowmik, S.; et al. Nitrogen-doped fluorescent graphene nanosheets as visible-light-driven photocatalysts for dye degradation and selective sensing of ascorbic acid. New J Chem., 2019, 43, 14575–83.
[142]: Huang, Y.; Liang, Y.; Rao, Y.; Zhu, D.; Cao, J. J.; Shen, Z.; et al. Environment-friendly carbon quantum dots/ZnFe2O4 photocatalysts: characterization biocompatibility and mechanisms for NO removal. Environ Sci Technol, 2017, 51, 2924–33.
[143]: Selvakumar, T.; Rajaram, M.; Natarajan, A.; Harikrishnan, L.; Alwar, K.; Rajaram, A. Highly efficient sulfur and nitrogen codoped graphene quantum dots as a metal-free green photocatalyst for photocatalysis and fluorescent ink applications. ACS Omega, 2022, 15, 790–8.
[144]: Kamat, P. V. Manipulation of charge transfer across semiconductor interface. A criterion that cannot be ignored in photocatalyst design. J Phys Chem Lett, 2012, 3, 663–72.
[145]: Zou, H.; Dong, C.; Li, S.; Im, C.; Jin, M.; Yao, S.; et al. Effect of surface trap states on photocatalytic activity of semiconductor quantum dots. J Phys Chem C, 2018, 122, 9312–9.
[146]: Mukherjee, I.; Cilamkoti, V.; Dutta, R. K. Sunlight-driven photocatalytic degradation of ciprofloxacin by carbon dots embedded in ZnO nanostructures. ACS Appl Nano Mater, 2021, 4, 7686–97.
[147]: Xu, W.; Jia, J.; Wang, T.; Li, C.; He, B.; Zong, J.; et al. Continuous tuning of Au-Cu2O Janus nanostructures for efficient charge separation. Angew Chem Int Ed Engl, 2020, 59, 22246–51.

[148]: Zhang, J.; Lu, X.; Tang, D.; Wu, S.; Hou, X.; Liu, J.; et al. Phosphorescent carbon dots for highly efficient oxygen photosensitization and as photo-oxidative nanozymes. ACS Appl Mater Interfaces, 2018, 10, 40808–14.

[149]: Xu, Y.; Wang, C.; Ran, G.; Chen, D.; Pang, Q.; Song, Q. Phosphate-assisted transformation of methylene blue to red-emissive carbon dots with enhanced singlet oxygen generation for photodynamic therapy. ACS Appl Nano Mater, 2021, 4, 4820–8.

[150]: Barman, M. K.; Jana, B.; Bhattacharyya, S.; Patra, A. Photophysical properties of doped carbon dots (N P and B) and their influence on electron/hole transfer in carbon dots-nickel (II) phthalocyanine conjugates. J Phys Chem C, 2014, 118, 20034–41.

[151]: Zhang, J.; Lu, X.; Tang, D.; Wu, S.; Hou, X.; Liu, J.; Wu, P. Phosphorescent Carbon Dots for Highly Efficient Oxygen Photosensitization and as Photo-oxidative Nanozymes, ACS Applied Materials & Interfaces, 2018, 10, 40808-40814.

[152]: Christensen I. L.; Sun, Y. P.; Juzenas, P. Carbon Dots as Antioxidants and Prooxidants, Journal of Biomedical Nanotechnology, 2011, 7, 667-676.

[153]: Ge, J.; Lan, M.; Zhou, B. et al. A graphene quantum dot photodynamic therapy agent with high singlet oxygen generation. Nat Commun, 2014 5, 4596.

[154]: Cao, Y.; Dong, H.; Yang, Z.; Zhong, X.; Chen, Y.; Dai, W.; Zhang, X. Aptamer conjugated graphene quantum dots/porphyrin derivative theranostic agent for intracellular cancer-related microRNA detection and fluorescence-guided photothermal/photodynamic synergetic therapy, ACS Appl. Mater. Interfaces, 2017, 9, 159–166

[155]: Edge, R.; Truscott, T. G.; The Reactive Oxygen Species Singlet Oxygen, Hydroxy Radicals, and the Superoxide Radical Anion—Examples of Their Roles in Biology and Medicine. Oxygen, 2021, *1*, 77-95

[156]: Zeng, L.; Zhao, H.; Zhu, Y.; Chen, S.; Zhang, Y.; Wei, D.; Sun, J.; Fan, H. One-pot synthesis of multifunctional Bi2S3 nanoparticles and the construction of core-shell Bi2S3@Ce6-CeO2 nanocomposites for NIR-triggered phototherapy, J. Mater. Chem. B, 2020, 8, 4093–4105.

[157]: Rigo, S.; Cai, C.; Gunkel-Grabole, G.; Maurizi, L.; Zhang, X.; Xu, J.; Palivan, C. G. Nanoscience-Based Strategies to Engineer Antimicrobial Surfaces Adv. Sci., 2018, 5, 1700892.
[158]: Z.-M. Xiu, Q.-B. Zhang, H.L. Puppala, V.L. Colvin, P.J.J. Alvarez, Negligible particle-specific antibacterial activity of silver nanoparticles, Nano Lett. 12 (8) (2012) 4271–4275.
[159]: Zhang, L.; Jiang, Y.; Ding, Y.; Povey, M.; York, D. Investigation into the antibacterial behaviour of suspensions of ZnO nanoparticles (ZnO nanofluids), J. Nanopart. Res., 2007, 9, 479–489.
[160]: Zhao, Y.; Tian, Y.; Cui, Y.; Liu, W.; Ma, W.; Jiang, X. Small molecule-capped gold nanoparticles as potent antibacterial agents that target gram-negative bacteria, J. Am. Chem. Soc., 2010, 132, 12349–12356.
[161]: Chernousova, S.; Epple, M. Silver as antibacterial agent: ion, nanoparticle, and metal, Angew. Chem. Int. Ed., 2013, 52, 1636–1653.
[162]: Dizaj, S. M.; Lotfipour, F.; Barzegar-Jalali, M.; Zarrintan, M. H.; Adibkia, K. Antimicrobial activity of the metals and metal oxide nanoparticles, Mater. Sci. Eng., C 44 (2014) 278–284.
[163]: Mubarak Ali, D.; Thajuddin, N.; Jeganathan, K.; Gunasekaran, M. Plant extract mediated synthesis of silver and gold nanoparticles and its antibacterial activity against clinically isolated pathogens, Colloids Surf. B, 2011, 85, 360–365.
[164]: Marambio-Jones, C.; Hoek, E. M. V. A review of the antibacterial effects of silver nanomaterials and potential implications for human health and the environment, J. Nanopart. Res., 2010, 12, 1531–1551.
[165]: Sun, Z.; Ostrikov, K. K. Future antiviral surfaces: Lessons from COVID-19 pandemic, Sustainable Materials and Technologies, 2020, 25, e00203.
[166]: Hasan, J.; Crawford, R. J.; Ivanova, E. P. Antibacterial surfaces: the quest for a new generation of biomaterials, Trends in Biotechnology, 2013, 31, 295-304.
[167]: Dong, X.; Liang, W.; Meziani, M. J.; Sun, Y. P.; Yang, L. Carbon Dots as Potent Antimicrobial Agents. Theranostics. 2020,10, 671-686.
[168]: Riahi, Z.; Rhim, J. W.; Bagheri, R.; Pircheraghi G.; Lotfali, E. Carboxymethyl cellulose-based functional film integrated with chitosan-based

carbon quantum dots for active food packaging applications, Prog. Org. Coating, 2022, 166, 1–14.
[169]: Zhao, L.; Zhang, M.; Mujumdar A. S.; Adhikari, B. Preparation of a Novel Carbon Dot/Polyvinyl Alcohol Composite Film and Its Application in Food Preservation, ACS Appl. Mater. Interfaces, 2022, 37528–37539.
[170]: Xu, N.; Gao, S.; Xu, C.; Fang, Y.; Xu L.; Zhang, W. Carbon quantum dots derived from waste acorn cups and its application as an ultraviolet absorbent for polyvinyl alcohol film, Appl. Surf. Sci., 2021, 556, 149774.
[171]: Das, P.; Ganguly, S.; Margel S.; Gedanken, A. Immobilization of Heteroatom-Doped Carbon Dots onto Nonpolar Plastics for Antifogging, Antioxidant, and Food Monitoring Applications, 2021, 37, 58.
[172]: Fan, K.; Zhang, M.; Fan D.; Jiang, F. Effect of carbon dots with chitosan coating on microorganisms and storage quality of modified atmosphere packaged fresh cut cucumber, J. Sci. Food Agric., 2019, 99, 6032–6041.
[173]: Li, H.; Huang, J.; Song, Y. X.; Zhang, M. L.; Wang, H. B.; Lu, F.; et al. Degradable Carbon Dots with Broad-Spectrum Antibacterial Activity. Acs Appl Mater Inter., 2018, 10, 26936-46.
[174]: Xiang, Y.; Mao, C.; Liu, X.; Cui, Z.; Jing, D.; Yang, X.; et al. Rapid and Superior Bacteria Killing of Carbon Quantum Dots/ZnO Decorated Injectable Folic Acid-Conjugated PDA Hydrogel through Dual-Light Triggered ROS and Membrane Permeability. Small., 2019, 15, e1900322.
[175]: Kousheh, S. A.; Moradi, M.; Tajik, H.; Molaei, R. Preparation of antimicrobial/ultraviolet protective bacterial nanocellulose film with carbon dots synthesized from lactic acid bacteria, International Journal of Biological Macromolecules, 2020, 155, 216-225.
[176]: Jackowska, K.; Bukowska, J.; Jamkowski, M. Synthesis, electroactivity and molecular structure of poly(l,5diaminonaphthalene). Journal of Electroanalytical Chemistry, 1995, 388, 101-108.
[177]: Cossu, F. L.; Poddighe, M.; Stagi, L.; Anedda, R.; Innocenzi, P. The Birth of Fluorescence from Thermally Polymerized Glycine, Macromol. Chem. Phys., 2022, 2200052.

[178]: Lee Jia Ming and Adeline Chia Yoke Yin. Therapeutic Effects of Glycyrrhizic Acid. Natural Product Communications, 2013, 8.
[179]: Stormer, F. C.; Reistad, R.; Alexander J. Glycyrrhizic acid in liquorice--evaluation of health hazard. Fd. Chem. Toxic., 1993, 31, 303-312.
[180]: Bart Ploeger, B.; Mensinga, T.; Sips, A.; Seinen, W.; Meulenbelt, J.; DeJongh, J. The pharmacokinetics of glycyrrhizic acid evaluated by physiologically based pharmacokinetic modeling. Drug Metabolism Reviews, 2001, 33, 125–147.
[181]: Privitera, G.; Agodi, A.; Bertinato, L.; D'Ancona, F. P.; Durando, P.; Monaco, R.; Mongardi, M.; Moro, M. L.; Nicastro, O.; Pan, A.; Pantosti, A.; Petrosillo, N.; Settimo, G. Indicazioni per la sanificazione degli ambienti interni per prevenire la trasmissione di SARS-COV 2. Rapporto ISS COVID-19 n. 20/2020.
[182]: Miao, X.; Qu, D.; Yang, D. X.; et al Synthesis of carbon dots with multiple color emission by controlled graphitization and surface functionalization. Adv Mater., 2018, 30, 1704740.
[183]: Jackowska, K.; Bukowska, J.; Jamkowski, M. Synthesis, electroactivity and molecular structure of poly(l,5diaminonaphthalene). Journal of Electroanalytical Chemistry, 1995, 388, 101-108.
[184]: Cossu, F. L.; Poddighe, M.; Stagi, L.; Anedda, R.; Innocenzi, P. The Birth of Fluorescence from Thermally Polymerized Glycine, Macromol. Chem. Phys., 2022, 2200052.
[185]: Yuan, F.; Wang, Z.; Li, X.; Li, Y.; Tan, Z.; Fan, L.; Yang, S. Bright Multicolor Bandgap Fluorescent Carbon Quantum Dots for Electroluminescent Light-Emitting Diodes. Adv. Mater., 2017, 29, 1604436.
[186]: Joseph, J.; Anappara, A. A. White light emission of carbon dots by creating different emissive traps. J. Lumin., 2016, 178, 128–133.
[187]: Derkacheva, O.; Sukhov, D. Investigation of Lignins by FTIR Spectroscopy. Macromol. Symp., 2008, 265, 61–68.
[188]: Abdel Azzem, M.; Yousef, U. S.; Limosin, D.; Pierre, G. Electra-oxidative oligomerization of 1,5-diaminonaphthalene in acetonitrile medium. Journal of Electroanalyfical Chemistry, 1996, 417, 163-173.

[189]: Wishart, D. S.; Knox, C.; Guo, A. C.; Eisner, R.; Young, N.; Gautam, B.; Hau, D. D.; Psychogios, N.; Dong, E.; Bouatra, S.; Mandal, R.; Sinelnikov, I.; Xia, J.; Jia, L.; Cruz, J. A.; Lim, E.; Sobsey, C. A.; Shrivastava, S.; Huang, P.; Liu, P.; Fang, L.; Peng, J.; Fradette, R.; Cheng, D.; Tzur, D.; Clements, M.; Lewis, A.; De Souza, A.; Zuniga, A.; Dawe, M.; et al., HMDB: a knowledgebase for the human metabolome. Nucleic Acids Res., 2009, 37, 603.

[190]: Saiful Badri, M. A.; Salleh, M. M.; Md Noor, N. F.; Rahman, M. Y. A.; Umar, A. A. Green synthesis of few-layered graphene from aqueous processed graphite exfoliation for graphene thin film preparation. Materials Chemistry and Physics, 2017.

[191]: Zhang, Y.; Gao, D.; Li, S.; Wei, W.; Lin, J.; Jiang, Y. 1,5-Diaminonaphthalene functionalized carbon nanodots as a novel matrix for the analysis of small molecules by matrix-assisted laser desorption/ionization mass spectrometry. Anal. Methods, 2019, 11, 1131-1136.

[192]: Socrates G. Infrared and Raman Characteristic Group Frequencies. John Wiley & Sons, LTD, 2001.

[193]: Schaich, K. M.; Karel, M. Free Radical Reactions of Peroxidizing Lipids with Amino Acids and Proteins: An ESR Study. Lipids, 1976, 11, 392–400.

[194]: Lipovsky, A.; Tzitrinovich, Z.; Friedmann, H.; Applerot, G.; Aharon Gedanken, A.; Lubart, R. EPR Study of Visible Light-Induced ROS Generation by Nanoparticles of ZnO. J. Phys. Chem. C 2009, 113, 15997–16001.

[195]: Zang, L. Y.; Zhang, Z.; Misra, H. P. EPR studies of trapped singlet oxygen (lo2) generated during photoirradiation of hypocrellin a. Photochemistry und Photobiology, 1990, 52, 677483.

[196]: Pratiwi, R. A.; Nandiyanto, A. B. D. How to Read and Interpret UV-VIS Spectrophotometric Results in Determining the Structure of Chemical Compounds. Indonesian Journal of Educational Research and Technology, 2022, 2, 1-20.

[197]: Bernela, M.; Ahuja, M.; Thakur, R. Enhancement of anti-inflammatory activity of glycyrrhizic acid by encapsulation in chitosan-katira gum nanoparticles. European Journal of Pharmaceutics and Biopharmaceutics, 2016, 105, 141-147.

[198]: Fischer, M. J. E. Amine Coupling Through EDC/NHS: A Practical Approach. Surface Plasmon Resonance, 2010, 627.
[199]: Carson, C. F.; Hammer, K. A.; Riley, T. V. Broth micro-dilution method for determining the susceptibility of Escherichia coli and Staphylococcus aureus to the essential oil of Melaleuca alternifolia (tea tree oil). Microbios., 1995, 82,181-5.